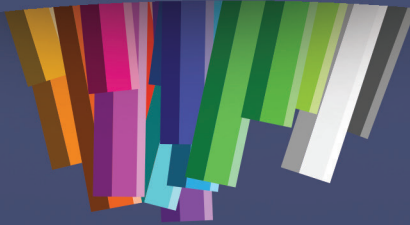




RESEARCH & REVIEWS IN ENGINEERING

MAY 2021

VOLUME 2



EDITORS

ASSOC. PROF. DR. BELMA HASDEMİR
DR. MAHMUT TURHAN
DR. CEREN KARAMAN

AUTHORS

TEODOR ILİEV
ELENA IVANOVA
IVAYLO STOYANOV
GRİGOR MİHAYLOV
BANU NERGİS
BURAK ÖZ
SERHAT KÜÇÜKDERMENCI
MUKADDER İGĐİ ŞEN
BETÜL SARAÇ
TEOMAN AYHAN
AHMET B. DEMİRPOLAT
ERCAN AYDOĞMUŞ
ÖZDOĞAN KARAÇALI

gece
kitaplığı

İmtiyaz Sahibi / Publisher • Yaşar Hız
Genel Yayın Yönetmeni / Editor in Chief • Eda Altunel
Kapak & İç Tasarım / Cover & Interior Design • Gece Kitaplığı
Editörler / Editors • Assoc. Prof. Dr. Belma Hasdemir
Dr. Mahmut Turhan
Dr. Ceren Karaman
Birinci Basım / First Edition • © May 2021
ISBN • 978-625-7411-77-6

© copyright

Bu kitabın yayın hakkı Gece Kitaplığı'na aittir.

Kaynak gösterilmeden alıntı yapılamaz, izin
almadan hiçbir yolla çoğaltılamaz.

The right to publish this book belongs to Gece Kitaplığı.

Citation can not be shown without the source, reproduced in any way
without permission.

Gece Kitaplığı / Gece Publishing

Türkiye Adres / Turkey Address: Kızılay Mah. Fevzi Çakmak 1. Sokak

Ümit Apt. No: 22/A Çankaya / Ankara / TR

Telefon / Phone: +90 312 384 80 40

web: www.gecekitapligi.com

e-mail: gecekitapligi@gmail.com



Baskı & Cilt / Printing & Volume

Sertifika / Certificate No: 47083

Research & Reviews in Engineering

May 2021

Volume 2

EDITORS

Assoc. Prof. Dr. Belma HASDEMİR

Dr. Mahmut TURHAN

Dr. Ceren KARAMAN

CONTENTS

CHAPTER 9

EVOLUTION OF 5G NETWORKS TOWARDS THE FUTURE 6G MOBILE NETWORKS: CONCEPTS, SERVICES AND KEY TRENDS

Teodor Iliev, Elena IVANOVA , Ivaylo STOYANOV,

Grigor MIHAYLOV 1

CHAPTER 10

DIVERSE APPROACHES TO RING SPINNING FOR HIGH QUALITY YARN PRODUCTION AND INCREASED PRODUCTIVITY

Banu NERGİS 23

CHAPTER 11

TENDER EVALUATION MODELS IN PUBLIC CONSTRUCTION WORKS AND CONSULTANCY SERVICES

Burak ÖZ 43

CHAPTER 12

OVERVIEW OF LINEAR HALBACH ARRAYS AND EFFECT OF PARAMETRIC CHANGES

Serhat KÜÇÜKDERMENÇİ 65

CHAPTER 13

HEALTH RISKS ENCOUNTERED OF SPACECRAFTS AND SPACE PEOPLE AND PROTECTION METHODS

Mukadder İĞDİ ŞEN 81

CHAPTER 14

THERMODYNAMIC ANALYSIS OF THE REFRIGERATION TEST EVAPORATOR UNIT WITH ADVANCED EXERGY ANALYSIS

Betül SARAÇ, Teoman AYHAN 97

CHAPTER 15

THE HYBRID-NANOFLUIDS REINFORCED WITH IRON(III) OXIDE AND COPPER(II) OXIDE

Ahmet B. DEMIRPOLAT, Ercan AYDOĞMUŞ 125

CHAPTER 16

INNOVATIVE EXPLORATION ON MODULAR BELT CONVEYOR TRANSPORTATION MECHANISIM BY DEFORMATION, VON-MISES STRESS MECHANICAL AND CFD ANALYSIS IN MATERIAL HANDLING

Özdoğan KARAÇALI 137

Chapter 9

EVOLUTION OF 5G NETWORKS TOWARDS THE FUTURE 6G MOBILE NETWORKS: CONCEPTS, SERVICES AND KEY TRENDS

Teodor ILIEV¹

Elena IVANOVA²

Ivaylo STOYANOV³

Grigor MIHAYLOV⁴

¹ University of Ruse, Department of Telecommunications, Ruse, Bulgaria

Corresponding author: tiliev@uni-ruse.bg

² University of Ruse, Department of Telecommunications, Ruse, Bulgaria

³ University of Ruse, Department of Electric Power Engineering, Ruse, Bulgaria

⁴ University of Telecommunications and Post, Department of Telecommunications, Sofia, Bulgaria

1. Introduction

Today we are at the stage of Industry 4.0 and the third wave digital transformation based on information and telecommunication technologies (ICT) and artificial intelligence. Since the 2000s, over 100 countries of the world (the majority of industrial developed and many developing) have decided to build their economies based on Industry 4.0 (Internet of Things - IoT, big data, blockchain, etc.) (Tsigkanos, 2019; Giordani, 2020; Grande, 2020). National plans for the development of ICT networks were approved for digitalization projects in many countries.

Ivanova (2021) states that wireless communications are one of the few sectors that kept a fast-growing tendency with creative features for a number of decades.

As a telecommunications basis for networks, IoT in the era of Industry 4.0, will use also already in maturity 4G mobile networks, and new booming 5G networks. Phase 2 standardization of 5G networks (Release 16) was finally completed in June 2020. The standardization of 5G communications has been completed, and the system is being deployed worldwide (Sadinov, 2020). On Figure 1 is shown the 5G commercial network coverage map worldwide (5G coverage, 2020).

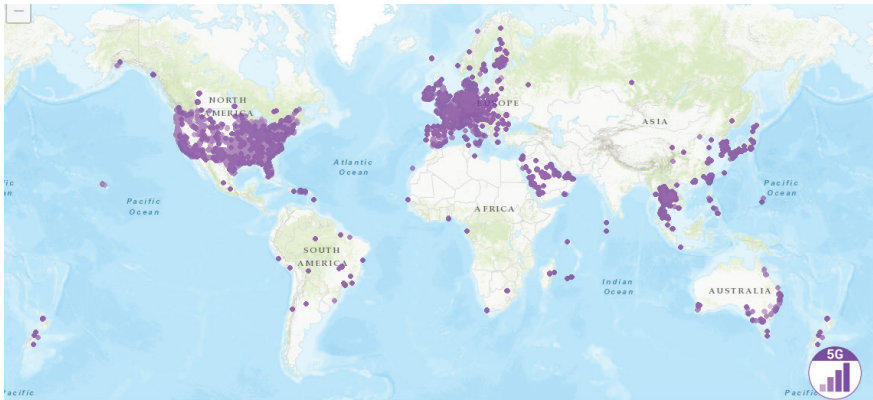


Figure 1. 5G coverage map worldwide (5G coverage map)

The new 5G network standards are being developed to accomplish the preferred performance goals and to co-exist with 4G network. The authors in Asadi (2018) explained that there is very limited spectrum available below 6 GHz, so mmWave frequencies that can incorporate wide-bandwidth transmissions are being investigated for next generation communication systems.

With the development of IoT, 5G includes communications between people and things (device to device, vehicle to vehicle, etc.). 5G networks have an extensive variety of services comprising enhanced mobile broadband

(eMBB), ultra-reliable and low-latency communications (uRLLC), and massive machine-type communications (mMTC). Nevertheless, wireless data traffic and the numbers of connected things are expected to leap to a hundredfold of equipment in a given m^3 . Thus, the service capability of 5G is improved to provide services to both people and things. 5G can achieve a peak data rate of 10 Gbps as explained in Iliev (2017) and perform well in eMBB scenario with bandwidth 400 MHz and more advanced channel coding and high-order modulation like Low-Density Parity Coding (LDPC) and 256QAM.

Furthermore in Baldemair (2016) and Sim (2020) was explained some applications such as sending HD multimedia, holographic videos need a spectrum bandwidth that is currently unavailable in the mmWave spectrum.

Such situation offerings demanding challenges on an area or a spatial spectral efficiency and the needed frequency spectrum bands for connectivity as explained in Viswanathan (2020). Therefore, a wider radio frequency bandwidth is needed and can only be found at the sub-terahertz THz and THz bands (Tikhvinskiy, 2020).

Additionally, the recent progress of various mobile applications, especially those supported by Artificial Intelligence (AI), is spurring intense discussions on the future evolution of wireless networks (Balabanova, 2019; Sheth, 2020). These challenges have motivated not only the scientists, but the industry to start conceptualizing the sixth generation (6G) of the wireless communication network. The aim of 6G is to provide communication services for the future application of 2030 and supporting the sustainability and competitiveness of wireless communication networks. The authors in Shafin (2020) and Zhou (2020) proposed that the 6G mobile networks are expected to offer a huge coverage that allows users to communicate with one another, at any time and any place, with a high data rate due to the unconventional technologies, that will be adopted by 6G networks, such as and tremendously large bandwidth (THz) and AI, including the functional and environmental aspects along with the services of the networks.

2. 5G mobile networks

The new 5G cellular standards are being developed to achieve the desired performance goals and to co-exist with 4G technologies. There is very limited spectrum available below 6 GHz so mmWave frequencies that can incorporate wide-bandwidth transmissions are being investigated for next generation cellular systems.

5G provides the ability to upgrade through cognitive radio technology, which includes various important features, such as the ability of devices to identify their geographical location, as well as time, temperature, and

more signals in its work environment. In addition, it timely distinguishes changes in its environment and responds accordingly to ensure continuous quality of service (QoS).

2.1. Characteristics of 5G

5G is a truly cohesive system supporting a wide range of mobile voice and multi-gigabit Internet applications for D2D and V2X communications, as well as proprietary machine type communications (MTC) and public safety applications. MIMO will be incorporated into Base Stations (BS) to further increase data speed and capacity at the macro-cellular level. The system's performance in terms of coverage, capacity, and energy efficiency (Ee) will be further enhanced in "dead" and hot spots through relay stations, deployment of small cells, or landing on WiFi; mmWave connections will be used to redirect relay and/or small BS cells. As explained in Iliev (2017) D2D communications will be supported by macro-BS, providing the control plane. The smart grid is another interesting application for 5G that allows the power grid to work more reliably and efficiently. Cloud computing can potentially be applied to radio access network (RAN) and mobile users, which can form a virtual set of resources that can be managed by the network. Bringing cloud apps to the end user reduces communication latency to support real-time applications.

The standardization of 5G technologies and solutions should be completed by 2021, so 5G currently means only fragmented solutions, which in the future will become part of the overall IMT2020 solution. Such solutions have already been implemented in various countries, but they are still local and test in nature and don't provide all the planned functionality of IMT2020 networks (Ivanova, 2021).

5G networks significantly extend the limited functionality of previous generations of mobile networks. The main functional characteristics of 5G networks can be summarized to:

- **Enhanced Mobile Broadband (eMBB)** - This use case category is the natural extension of the classic mobile broadband connectivity scenario under current mobile telecommunication standards. It addresses human-centric connectivity, including access to multimedia content, services, and data. This is done by providing the high data rates that are required to support future multimedia services and the increasing traffic volume generated by these services.

- **Ultra-Low Latency Reliable Communication (ULLRC)** - stringent requirements on both latency and reliability are the distinctive features of this use case category, which targets mainly machine-type communications (MTC). Envisaged applications include wireless control

of industrial manufacturing and production processes, remote medical surgery, driverless and/or remotely driven vehicles, and distribution automation in smart grids.

- **Massive IoT/IIoT, mMTC (massive Machine Type Communication)** - the growth of the Internet of Things (IoT) is causing a proliferation of wirelessly connected devices carrying MTC traffic. Indeed, the number of such devices is expected to exceed soon the number of devices carrying human-generated traffic. The focus of the mMTC is on providing connectivity to a massive number of devices, which are assumed to transmit sporadically a low amount of traffic, which is not delayed critical. The mMTC devices are expected to have a very long battery lifetime to allow for remote deployments. Key requirements for such services include very low device cost and very low device energy consumption, allowing for very long device battery life of up to at least several years. A distinctive feature of this use case is that the MTC devices will be extremely heterogeneous in terms of capabilities, cost, energy consumption, and transmission power.

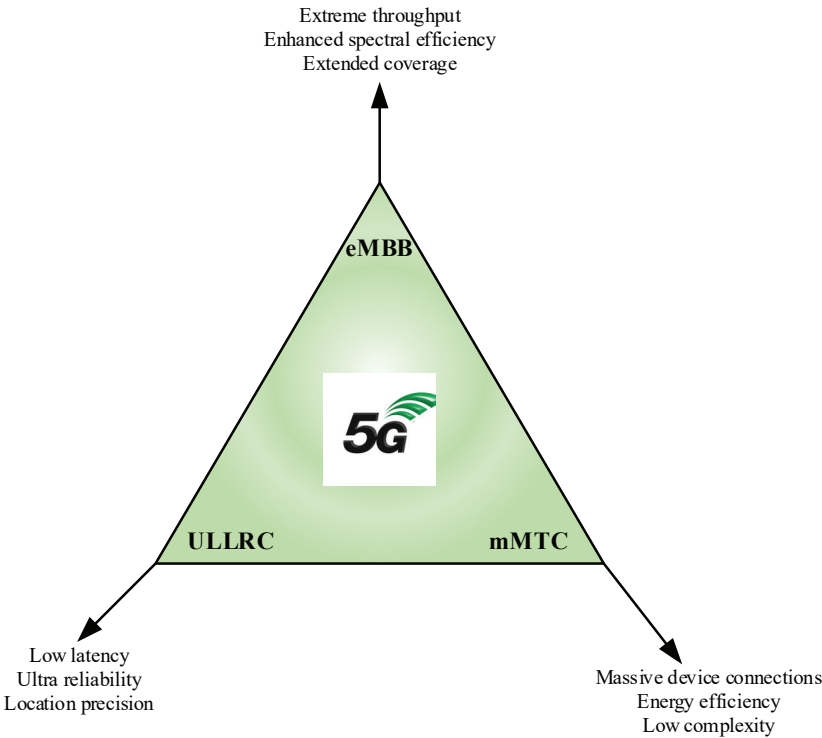


Figure 2. 5G uses cases

2.2. Millimeter wave communications

The primary motivation for using millimeter waves is the promise of an abundant spectrum above 30 GHz. While mmW spectrum spans the range from 30 GHz–300 GHz, it is widely believed that the reach of mass market semiconductor technology extends up to around 100 GHz and will inevitably surpass that limit with time (ETSI GS mWT 0020). Microwave bands from 3 GHz–30 GHz are just as relevant to meeting extreme requirements for 5G. Millimeter wave bands in current use are predominantly employed for radar, earth exploration, point-to-point services, and satellite communications, etc. Some of these bands are assigned in co-primary fashion to mobile services; there are of course no terrestrial mobile services in operation above 6 GHz. The 60 GHz ISM band does provide as much as 7 GHz of spectrum for unlicensed use in most parts of the world; the band has been used by IEEE 802.11 in the recent “ad” amendment to create a physical and Medium Access Control (MAC) layer capable of peak rates up to 7 Gbps (Baldemair, 2016).

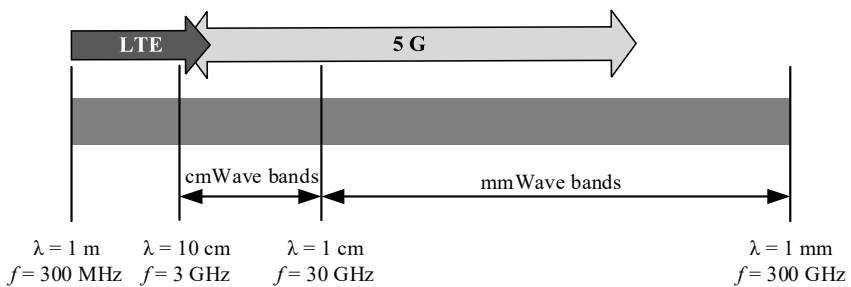


Figure 3. Spectrum band occupied by mmWaves

Millimeter wave bands pose unique challenges for radio communication. Large-scale losses over line-of-sight paths generally follow free space loss values, and attenuation relative to isotropic radiators increases proportionally to the square of operating frequency. Millimeter wave path losses are affected by a variety of other additional factors, all of which are generally frequency dependent: (a) atmospheric losses due to gases, notably water vapor and oxygen, (b) rain attenuation, (c) foliage loss, (d) diffraction loss. Rappaport et. al (2019) proposed that below 100 GHz, two atmospheric absorption peaks occur at 24 GHz and 60 GHz, due to water and oxygen.

Spectrum above 30 GHz is useful for near line-of-sight environments; these are typically interior or exterior spaces that are connected in a way that allows propagation of electromagnetic fields. Coverage in such environments is provided by dense deployment of infrastructure nodes within and around hot spots that tend to concentrate traffic.

Millimeter wave bands above 60 GHz are well suited for short range point-to-point links for backhaul. These bands will typically support higher bandwidth communication than access links, and can support high-reliability performance requirements for the data plane as well as provide excess bandwidth for link management and radio system monitoring. Such bands will also find use for short range applications that need very wide bandwidth capability, such as video transmission, virtual office or augmented and virtual reality applications (Baldemair, 2016).

2.3. Device-to-Device Communication

Device-to-device communications in cellular spectrum supported by a cellular infrastructure has the potential of increasing spectrum and energy efficiency as well as allowing new peer-to-peer services by taking advantage of the so called proximity and reuse gains. In fact, D2D communications in the cellular spectrum are currently studied by the 3GPP to facilitate proximity aware internetworking services (Tsigkanos, 2019), national security and public safety applications (Guevara, 2020), and machine type communications (Baldemair, 2016).

Obviously, D2D communications utilizing cellular spectrum poses new challenges, because relative to cellular communication scenarios, the system needs to cope with new interference situations. For example, in an orthogonal frequency division multiplexing (OFDM) system in which user equipment's (UE) are allowed to use D2D (LTE direct mode) communication, D2D communication links may reuse some of the OFDM time-frequency physical resource blocks (RB). Due to the reuse, intracell orthogonality is lost and intracell interference can become severe due to the random positions of the D2D transmitters and receivers as well as of the cellular UEs communicating with their respective serving base stations (Iliev, 2017).

2.4. Smart Mobility Management for D2D Communications

Iliev (2017) assumed that the D2D resource usage and coordination are under the network's control. This is due to the fact that in-band D2D operation, as an underlay for cellular communications, requires the network's control on D2D radio resources in order to provide optimized resource utilization, minimized interference among D2D links, and from D2D links to cellular link, as well as more robust mobility.

Enabling very low latency data communications between end-users is one of the distinctive advantages expected from Device-to-Device communications. However, when several base stations (BSs), which are connected to each other via a non-ideal backhaul, are involved in the D2D radio resource control, the quality of service requirement in terms of

latency may not be satisfied due to large backhaul delay. Furthermore, the additional control overhead is expected due to the exchange of necessary information between controlling nodes as depicted in Figure 4. Therefore, Iliev (2017) proposed two smart mobility management solutions that can be used to minimize the negative impacts (e.g., larger latency and additional signalling overhead) of multi-site radio resource control on D2D communications by controlling the D2D control handover and cell selection during the mobility of D2D UEs (DUEs):

- D2D-aware handover solution,
- D2D-triggered handover solution.

Here, it should be noted that D2D control handover and regular cellular handover could be executed separately, such as in dual connectivity.

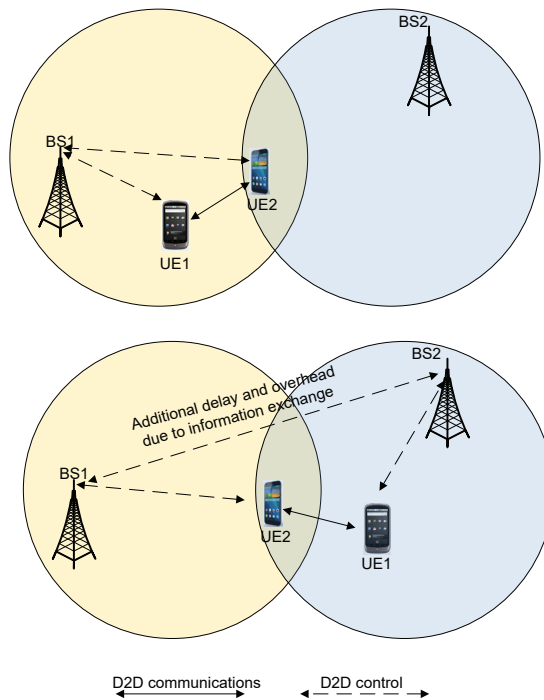


Figure 4. D2D control and communications before and after regular cellular handover execution

D2D-aware handover solution is introduced to minimize the End-to-End (E2E) latency in D2D communications and reduce the network signalling overhead in case of DUE mobility.

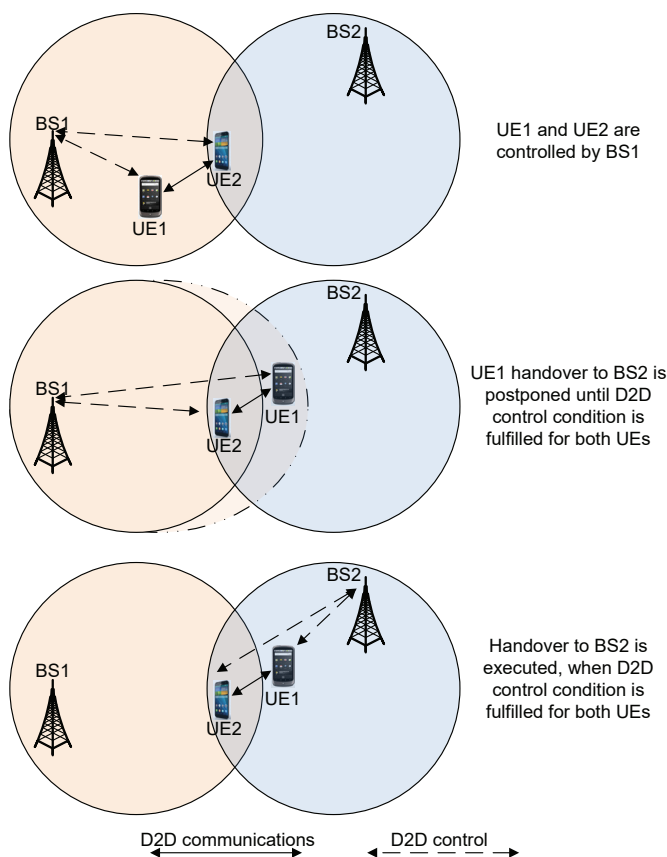


Figure 5. D2D control and communications during the DUE mobility between different sites

With D2D-triggered handover solution, Iliev (2017) proposed within a minimum number of cells or BSs to reduce the network signalling overhead caused by the inter-BS information exchange, such as related to D2D radio resource usage. The solution targets the scenarios where D2D groups are dynamically formed by more than two DUEs (Figure 5). The solution can be applied when DUEs taking part in a D2D group are varying in time, for instance, due to mobility.

3. Requirements and Key Trends of the Future 6G Networks

One of the first research projects for 6G was launched by the University of Oulu, Finland for full future adaptation of 6G network by the end of 2030 (6G White Paper, 2020). In addition to this university, many research institutes have started to explore numerous issues and tasks in 6G networks, like Seoul National University, Korea, Korea Advanced Institute of Science and Technology, Southeast University, China, NTT Docomo, Japan, etc. At the same time, three industrial groups were created by the European

Telecommunications Standards Institute (ETSI) to develop specifications for new-generation mobile networks: millimeter Wave Transmission (ETSI GS mWT 002), Network Function Virtualization (NFV) (ETSI GS NFV-INF 001), and Next Generation Protocols (NGP) (ETSI GS NGP 001).

6G offers some fascinating services beyond broadband applications explained in Strinati (2019) and Piran (2019), such as extended reality (XR), virtual reality (VR), mixed reality (MR), augmented reality (AR), super Hi-vision video streaming (8K), holographic communications, eHealth, unmanned aerial vehicles (UAV), connected autonomous vehicles, etc., currently not available by the 4G and 5G communication networks.

Table 1. 6G Key performance indicators compared to 5G

Parameter	Systems	
	5G	6G
Services	- eMBB; - URLLC; - mMTC.	- MBRLLC; - mURLLC; - HCS; - MPS.
UEs	- Smartphones; - Sensors; - UAV.	- Sensors and DLT devices; - XR and BCI; - Smart implants.
Bandwidth (max)	1 GHz	100 GHz
Spectral efficiency considering energy efficiency	100 bits/s/Hz/m ² /J	1000 bits/s/Hz/m ³ /J
E2E latency	~1 ms	<1 ms
Radio latency	0,5 ms	0.1 ms
Reliability	99.9999%	99.99999%
Mobility	350 km/h	>1000 km/h
Positioning precision	10 – 100 cm in 2D	1 cm in 3D
Peak data rate	10 (20) Gbps	>1Tbps
Connection density	10 ⁶ devices/km ²	10 ⁶ devices/km ² 100 devices/m ³

Notes:

MBRLLC – Mobile Broadband Reliable Low Latency Communication;

mURLLC – massive URLLC;

HCS – Human-Centric Services;

MPS – Multi-Purpose Services;

DLT – Distributed Ledger Technology;

CRAS - Connected Robotics and Autonomous Systems.

Based on the great capabilities of 5G wireless communications networks, the mobile industry should be relocated from the traditional approaches to

some new ones like Iliev (2017), including operation in shared spectrum bands, inter-operator spectrum sharing, indoor small cell networks, a large number of local network operators, etc. Tikhvinskiy (2020), Alsharif (2020), Chowdhury (2020) scientists and researchers have set out research methods on the formulation, characterization, design, and identification of significant technologies motivating the initiation toward a beyond 5G networks or 6G communication system. Therefore, the requirements of 6G compared to 5G are more limited as shown in Table 1.

In the next paragraphs, we discuss some of the most significant requirements and tendencies of the future generation of mobile communication networks.

The future 6G communication systems are expected to be featured by the following associated services (Tsigkanos, 2019; Tikhvinskiy, 2020; Khan, 2020):

- Ubiquitous mobile ultra-broadband (uMUB);
- Mobile broadband reliable low latency communication (MBRLLC);
- Ultra-high speed with low latency communications (uHSLLC);
- Massive machine-type communication (mMTC);
- Ultra-high data density (uHDD);
- Human-centric services (HCS);
- Multi-purpose services (MPS).

The future 6G networks are expected to increase the level, currently set by 5G networks with the donation of improved services from the perspectives of network data availability, mobile data rate, and seamless ubiquitous connection. Additionally, 6G communications will utilize a rare communication method to gain acceptance to numerous mobile data groups and send them via traditional enhanced radio networks. Such a process will allow the innovative wireless transmission of feelings with participation and virtual presence (Alsharif, 2020), including holographic calls (Strinati, 2019) and a tactile Internet (Saad, 2020) [24, 27]. Figure 6 present the major key features of future 6G networks.

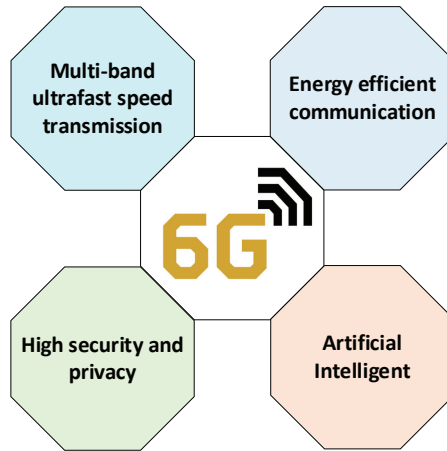


Figure 6. 6G key features

The outstanding concepts are the THz wireless communications system, AI, and programmable intelligent surfaces. It is expected, that the future 6G system will have 1000 times higher simultaneous connectivity in comparison with 5G network. New features are expected to have latency nearby to zero, such as end-to-end delay of less than 1 ms. It is supposed that by the end of 2030, there will be 50 billion connected devices to Internet of Everything (IoE), which means an enormous number of connections per km². In the future mMTC, as also known massive IoE (mIoE), machines will play the roles that were done by a human in the previous network generations. The ultra-high speed with low latency communications (uHSLLC) in 6G will provide fast connectivity, high reliability of more than 99.99999%, and a peak data rate of approximately 1 Tbps. The user equipment or devices in 6G network will need much more energy, in comparison with the 4G/5G wireless networks – they are invented to operate in higher frequency radio bands. Thus, Alsharif (2020) proposed that the energy consumption and energy efficiency are some of the challenges that need to be taken into the consideration. The future 6G communications will employ satellite communication technologies to provide global coverage. 6G will integrate telecommunication satellites, earth imaging satellites, and navigation satellites to provide localization services, broadcast and Internet connectivity (Rappaport, 2019), as well as weather information to cellular users.

The 6G networks will employ satellite communications (GPS, Galileo, Glonass, BeiDou, QZSS) to provide global coverage and super precision positioning (Filjar, 2021). This will help in the progress of connected robots and fully autonomous connected vehicles. The 6G network will offer complete unmanned mobility, safe and self-driving cars, a smart infotainment system, and enhanced traffic management.

4. 6G Technologies: Concepts and Services

Based on the growth of mobile networks (primarily 4G and 5G), 6G networks are mainly based on the architecture and deriving the benefits achieved in 5G (Sim, 2020; Viswanathan, 2020; Guevara, 2020). Some of the technologies, implemented in 5G, will be improved in 6G and several new technologies and applications will be added. Therefore, the 6G communication network will be operated by many technologies. Some of the expected essential technologies for 6G networks are discussed in the following sections (shown on Figure 7).

4.1. Artificial Intelligence (AI)

Artificial Intelligence (AI) (Balabanova, 2019) and Machine learning (ML) (Asadi, 2018), along with deep learning, are widely considered technologies that can be one of the key parts of the future 6G network. It can be said, that without a doubt, AI has attracted a lot of attention in the field of networking as image classification, computer vision, social networks, and security. AI and ML technologies can be implemented in the 6G communication networks in different layers: data links and network infrastructure, SDN, NFV, and cloud/edge/fog computing (Lataief, 2019). The intelligent radio transmission in the future 6G network can be realized completely through AI with assistance from ML algorithms. We really expect to go from AI and ML as a basis for air interface design, self-optimizing transmitters, and receivers and cognitive spectrum use.

4.2. Mobile Edge Computing

Due to the distributed massive cloud applications, mobile edge computing (MEC) becomes a significant part of 6G technologies, which helps the calculations to be performed as close to the IoT devices as possible (Tsiganos, 2019; Grande, 2020). Implementation of AI-based MEC in (Hussain, 2020) will reduce the data volume sent to the central servers, which will ultimately lead to lower latency, as a result improving the performance of real-time services and applications. Shafin (2020) proposed that the AI techniques implemented in MEC (complex networks) could achieve better results rather than using the traditional algorithms. MEC can play a significant role to provide high Quality of Experience (QoE) in smart dynamic services and applications for edge scenarios.

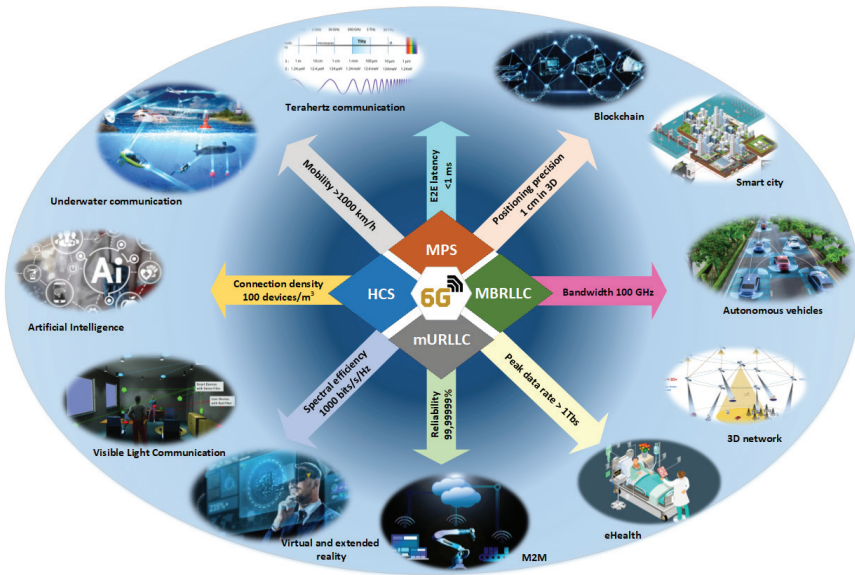


Figure 7. 6G architecture scenarios

4.3. Blockchain

The blockchain is a comparatively newer technology and offers a variety of applications, as explained Alsharif (2020). In the 6G systems, some numerous services and applications can be supported – smart healthcare, network decentralization, spectrum sharing, smart transportation, distributed ledger technologies (DLT). Khan (2020) proposed that the use of blockchain in 6G networks would considerably improve the security of authentication and could simplify the network management and enhance the network performance. On another hand, blockchain technologies combine a distributed network architecture, compromise mechanism, and innovative cryptography to highlight the promising features that are not available in the existing structures (Chowdhury; 2020, Wang, 2020).

One of the primary goals of 6G systems are scalability and reliability of the networks. Implementing the blockchain will be possible to achieve key design aspects, such as fault tolerance, security, low latency, and decentralization.

4.4. Terahertz Technology (THz)

The first specification of 5G NR, developed by 3GPP using mmWave and sub-6 GHz bands supporting high data transfer. 6G aims to enable even higher data rates and new applications. The radio frequency band (RF) is filled by existing wireless communications and cannot be used for future technologies (Rappaport, 2019). These factors stimulated the development of 6G networks through the use of terahertz (THz) waves in addition to

mmWave bands. THz waves operate between 0.1 THz and 10 THz, with the equivalent wavelengths 0.03 mm÷3 mm range. The ITU-R specified the 0.275÷3 THz band as the main band for terahertz communications in cellular networks. The THz communication compared to mmWaves will improve the 6G capabilities by supporting wireless communication, high data rates in the order of hundreds of Gbps, super Hi-vision video streaming, augmented reality, and precise positioning (Rappaport, 2019; Wang, 2020).

The THz band offers several advantages, but on the other hand, propagation loss, molecular absorption, high penetration loss are just some of the issues that must be resolved to enable the use of terahertz communication in 6G networks. All these lead to engineering challenges for antenna systems and effective transceivers with innovative adaptive array technologies.

4.5. Visible Light Communications

Visible light communication (VLC) has been proposed to complement RF communications by adapting a cheap light-emitting diode (LED). These devices can indeed switch between different light intensities very quickly to modulate a signal and to transmit it to a proper receiver (Strinati, 2019). In comparison with RF which has high latency and interference, the VLC offers higher bandwidths and resistance to electromagnetic interference. The progress of LED technology and multiplexing techniques are among the main prerequisites for the application of VLC in 6G network (Alsharif, 2020). On the other, hand the wavelength division multiplexing and the use of white light based on different wavelengths will increase the transmission rates to 100+ Gbps for VLC access points. Communication systems based on visible light communication can offer very high data rates, low latencies, and secure communications.

4.6. 3D networks

The current 5G and previous generations networks also have been designed to provide connectivity for devices collocated on the ground in bi-dimensional space (2D network). However, as explained in (Giordani, 2020) the 6G heterogeneous networks will integrate the ground and space networks to provide communications for UE in the three-dimensional (3D) network and to incorporate satellites, terrestrial networks, UAVs, and undersea communications. Thus, the 6G communication systems genuinely accomplished the global coverage and stringent seamless access, even for river, sea, plane, and mountain areas (Piran, 2019; Hussian, 2020). The altitude above Earth's surface of low earth orbit satellites is between 700 to 1500 km, for that reason, it is difficult to achieve the ultra-low delays of the signals. Long-distance imposes higher power requirements for IoT equipment to communicate with the satellite.

Regardless of these opportunities, some challenges need to be addressed before UAVs can be effectively used in wireless networks, such as modelling space to ground communication channels, improving the topology and trajectory, energy efficiency, and resource management.

4.7. eHealth

The eHealth isn't a new technology, like an example, the medical specialists used for more than two decades the Wireless Brain-Computer Interaction (BCI). The future 6G networks in combination with AI will change the healthcare sector, so the doctors and nurses can provide and guarantee better patient care. Healthcare will be significantly changed, with 24/7 monitoring of the human vitals and environmental readings (e.g. humidity, air pollution, temperature) through a number of both wearable IoT devices and implants. Remote surgery will also be possible through 6G communications. The real-time data of the patient will be used as the raw data, which are then transmitted to edge servers or through the Internet for analysis (Sheth, 2020; Letaief, 2019; Thuemmler, 2018).

4.8. Autonomous Systems and Intelligent Transport System

The Internet of Things, Smart Cities, and Intelligent Transportation Systems are three of the main concepts that will be encouraged with the appearance of 5G and the future 6G technologies.

The future 6G networks can support the deployment of autonomous vehicles and unmanned aerial vehicles (UAV). In the intelligent transport system (ITS) the vehicle shares its sensor data and current position with other vehicles and the roadway. On the other hand, the vehicles can receive data from the roadway and/or infrastructure, which can reduce the likelihood of incidents and improve mobility. With the usage of AI and such type of communications as explained by (Sharif, 2020; Guevara, 2020; Guo, 2019), ITS can succeed in safe intersection crossing, safe lane changing, optimal traffic signal control, smart parking allocation, and emergency warning notification. The UAV can simplify the eMBB, mMTC, and URLLC services in the 6G networks, so, therefore, could help in various fields including smart video surveillance, aerial photography, smart farming, and disaster management.

4.9. Smart Cities

The concept of a smart city was proposed in the late 1990 and was aimed primarily at the development of technologies and infrastructure of the city. Some scientists defined that the smart city is distinguished by the use of such components of smart urban systems as smart video surveillance system and video analytics; intelligent street lightning system; intelligent transportation system; public Wi-Fi networks; IoT; augmented and virtual

reality; unmanned and autonomous vehicles, etc. (Tsigkanos, 2019; Grande, 2020; Guevara, 2020; Wang, 2020). Powerful use of intelligent systems can be achieved with the combination of artificial intelligence techniques with edge technologies and devices.

5. Conclusion

We analysed and discussed the opportunities, main technical challenges, and services that will characterize the future 6G networks. On another hand, we derived the key performance indicators of 6G network and compared them to the present 5G communication standard. There is a tradition of inventing a new mobile generation standard approximately every decade, for this reason, the appearance of the 6G at the end of 2030 is quite possible. Future research in the field of 6G wireless networks will be further developed, upgraded, and complement the recent technologies used in the 5G networks. In this regard, will be introduced the use of Terahertz technology in addition to mmWaves, visible light communications, edge computing, and others. Improving the performance of 6G networks will be achieved through the use and development of AI/ML technologies. Finally, we recognized the following key technologies most possible to be defined for the future 6G network: (i) AI and ML technologies implemented in network infrastructure, SDN, NFV, and cloud/edge/fog computing; (ii) wider radio frequency bandwidth terahertz (THz) waves in addition to mmWave; (iii) blockchain technologies can be supported – smart healthcare, network decentralization; (iv) three-dimensional (3D) network incorporated satellites, terrestrial networks, UAVs and undersea communications; (v) autonomous vehicles and UAVs can simplify the eMBB, mMTC and URLLC services in the 6G networks. These technologies are not yet available to users, but they all give researchers an incentive to work in different areas, such as: the study of spatial multiplexing algorithms for antennas systems of 6G radio access network; investigation of the radio frequency bands 92-174.8 GHz range for the development of 6G generation mobile communication networks; research into the need and scenarios for the use of AI to improve the efficiency of the 6G radio interface.

REFERENCES

- 5G coverage map worldwide, Retrieved from <https://www.nperf.com/bg/map/5g>
- 6G White Paper on Connectivity for Remote Areas, 6G Research Visions, No. 5, June 2020, Retrieved from <http://jultika.oulu.fi/files/isbn9789526226750.pdf>
- Alsharif, M., Kelechi, A., Albreem, M., Chaudhry, S., Zia, M. S. & Kim, S., (2020). Sixth Generation (6G) Wireless Networks: Vision, Research Activities, Challenges and Potential Solutions. *Symmetry* 12, 4, 676, <https://doi.org/10.3390/sym12040676>
- Asadi, A., Müller, S., Sim, G. H., Klein, A., & M. Hollick, M., (2018). FML: Fast Machine Learning for 5G mmWave Vehicular Communications. *IEEE INFOCOM 2018 - IEEE Conference on Computer Communications*, Honolulu, HI, pp. 1961-1969, doi: 10.1109/INFOCOM.2018.8485876.
- Balabanova, I., Kostadinova, S., Markova, V., & Georgiev, G., (2019). Analysis and Categorization of Traffic Streams by Artificial Intelligence. *2019 International Conference on Biomedical Innovations and Applications (BIA)*, Varna, Bulgaria, pp. 1-5, doi: 10.1109/BIA48344.2019.8967475.
- Baldemair, R., Balachandran, K., Sundström, L. & Hui, D., (2016). Millimeter wave communications. in Osseiran, A., Monserrat, J. F., & Marsch (Eds) P. *5G Mobile and Wireless Communications Technology*. Cambridge University Press 2016.
- Chowdhury, M. Z., Shahjalal, M., Ahmed, S., & Jang, Y. M., (2020). 6G Wireless Communication Systems: Applications, Requirements, Technologies, Challenges, and Research Directions. *IEEE Open Journal of the Communications Society*, 1, pp. 957-975, doi: 10.1109/OJCOMS.2020.3010270.
- Digital transformation of Bulgaria for the period 2020-2030, Retrieved from: https://www.mtitc.government.bg/sites/default/files/digital_transformation_of_bulgaria_for_the_period_2020-2030_f.pdf
- ETSI GS NFV-INF 001, Network Functions Virtualisation (NFV), Infrastructure Overview, Retrieved from https://www.etsi.org/deliver/etsi_gs/NFV-INF/001_099/001/01.01.01_60/gs_NFV-INF001v010101p.pdf
- ETSI GS NGP 001, Next Generation Protocols (NGP), Scenarios Definitions, Retrieved from https://www.etsi.org/deliver/etsi_gs/NGP/001_099/001/01.01.01_60/gs_NGP001v010101p.pdf
- Filjar, R., Damas, M. & Iliev, T., (2021). Resilient satellite navigation empowers modern science, economy, and society”, *IOP Conference Series: Materials Science and Engineering*, 1032, 012001, <https://doi.org/10.1088/1757-899X/1032/1/012001>
- Giordani, M., Polese, M., Mezzavilla, M., Rangan, S. & Zorzi M., (2020). Toward 6G Networks: Use Cases and Technologies. *IEEE Communications Magazine*, 58(3), pp. 55-61, doi: 10.1109/MCOM.001.1900411.

- Grande, E., & Beltrán M., (2020) Edge-centric delegation of authorization for constrained devices in the Internet of Things. *Computer Communications*. 160, pp. 464-474, <https://doi.org/10.1016/j.comcom.2020.06.029>.
- GS mWT 002, millimetre Wave Transmission (mWT), Applications and use cases of millimetre wave transmission, Retrieved from https://www.etsi.org/deliver/etsi_gs/mWT/001_099/002/01.01.01_60/gsmwt002v010101p.pdf
- Guevara, L. & Cheein, F. (2020). The Role of 5G Technologies: Challenges in Smart Cities and Intelligent Transportation Systems. *Sustainability*, 12(16), 6469. <https://doi.org/10.3390/su12166469>
- Guo, Y., Wang, Z., Li, M., & Liu Q., (2019). Machine Learning Based mmWave Channel Tracking in Vehicular Scenario. *IEEE International Conference on Communications Workshops (ICC Workshops)*, Shanghai, China, pp. 1-6, doi: 10.1109/ICCW.2019.8757185.
- Hussain, B., Du, Q., Imran, A. & Imran, M. A., (2020). Artificial Intelligence-Powered Mobile Edge Computing-Based Anomaly Detection in Cellular Networks. *IEEE Transactions on Industrial Informatics*, 16(8), pp. 4986-4996, doi: 10.1109/TII.2019.2953201.
- Iliev, T. B., Mihaylov, G. Y., Ivanova, E. P. & Stoyanov, I. S., (2017). Power control schemes for device-to-device communications in 5G mobile network. *40th International Convention on Information and Communication Technology, Electronics and Microelectronics (MIPRO)*, pp. 416-419, doi: 10.23919/MIPRO.2017.7973460.
- Iliev, T. B., Nikolaev, N. T., Mihaylov, G. Y., Ivanova, E. P., Stoyanov, I. S. & Radev, D. I., (2018). A Critical View of the NFV Dataplane Implementations for 5G Networks. *26th Telecommunications Forum (TELFOR)*, Belgrade, pp. 1-4, doi: 10.1109/TELFOR.2018.8611980.
- Ivanova, E., Iliev, T., Stoyanov, I., & Mihaylov, G., (2021) Evolution of mobile networks and seamless transition to 5G. *IOP Conference Series: Materials Science and Engineering*, 1032, 012008, <https://doi.org/10.1088/1757-899X/1032/1/012008>
- Khan, L. U., Yaqoob, I., Imran, M., Han, Z., & Hong, C. S., (2020). 6G Wireless Systems: A Vision, Architectural Elements, and Future Directions. *IEEE Access*, 8, pp. 147029-147044, doi: 10.1109/ACCESS.2020.3015289.
- Letaief, K. B., Chen, W., Shi, Y., Zhang, J. & Zhang, Y. A., (2019). The Roadmap to 6G: AI Empowered Wireless Networks. *IEEE Communications Magazine*, 57(8), pp. 84-90, doi: 10.1109/MCOM.2019.1900271.
- Piran, M. J., & Suh, D. Y., (2019) Learning-Driven Wireless Communications, towards 6G. *International Conference on Computing, Electronics & Communications Engineering (iCCECE)*, London, United Kingdom, pp. 219-224, doi: 10.1109/iCCECE46942.2019.8941882.

- Rappaport, T. S. et al., (2019). Wireless Communications and Applications Above 100 GHz: Opportunities and Challenges for 6G and Beyond, *IEEE Access*, 7, pp. 78729-78757, doi: 10.1109/ACCESS.2019.2921522.
- Rappaport, T., Xing, Y., Kanhere, O., Ju, S., Madanayake, A., Mandal, S., Alkhateeb, A., Trichopoulos, G., (2019). Wireless communications and applications above 100 GHz: Opportunities and challenges for 6g and beyond. *IEEE Access*. 7. pp. 78729-78757, doi: 10.1109/ACCESS.2019.2921522.
- Saad, A., Al-Ma'aitah, M. & Alwadain, A., (2020). 6G technology based advanced virtual multi-purpose embedding algorithm to solve far-reaching network effects. *Computer Communications*, 160, pp. 749-758, <https://doi.org/10.1016/j.comcom.2020.07.025>.
- Sadinov, S., Kogias, P., Angelov, K., Malamatoudis, M., & Aleksandrov, A., (2020). The Impact of Channel Correlation on the System Performance and Quality of Service in 5G Networks. *7th International Conference on Energy Efficiency and Agricultural Engineering (EE&AE)*, Ruse, pp. 1-4, doi: 10.1109/EEAE49144.2020.9278982.
- Shafin, R., Liu, L., Chandrasekhar, V., Chen, H., Reed, J., & Zhang, J. C., (2020). Artificial Intelligence-Enabled Cellular Networks: A Critical Path to Beyond-5G and 6G. *IEEE Wireless Communications*, 27(2), pp. 212-217, doi: 10.1109/MWC.001.1900323.
- Sheth, K., Patel, K., Shah, H., Tanwar, S., Gupta, R., & Kumar, N., (2020). A taxonomy of AI techniques for 6G communication networks. *Computer Communications*, 161, pp. 279-303, <https://doi.org/10.1016/j.comcom.2020.07.035>.
- Sim, M. S., Lim, Y., Park, S. H., Dai, L., & Chae, C., (2020). Deep Learning-Based mmWave Beam Selection for 5G NR/6G With Sub-6 GHz Channel Information: Algorithms and Prototype Validation. *IEEE Access*, 8, pp. 51634-51646, doi: 10.1109/ACCESS.2020.2980285.
- Strinati E., et al. (2019) 6G: The Next Frontier: From Holographic Messaging to Artificial Intelligence Using Subterahertz and Visible Light Communication. *IEEE Vehicular Technology Magazine*, 14(3), pp. 42-50, doi: 10.1109/MVT.2019.2921162.
- Thuemmler, C., Paulin, A., Jell, T., Lim, A. (2018). Information Technology – Next Generation: The Impact of 5G on the Evolution of Health and Care Services. In: Latifi S. (eds) *Information Technology - New Generations. Advances in Intelligent Systems and Computing*, 558. Springer, Cham. https://doi.org/10.1007/978-3-319-54978-1_100
- Tikhvinskiy, V., Devyatkin, E., Bochechka, G., & Borodin, A., (2020). 6G at the start. *The Electrosvyaz Magazine*, 1, pp. 54 – 59 (in russian)

- Tsigkanos, C., Nastic, S., & Dustdar, S. (2019). Towards resilient Internet of Things: Vision, challenges, and research roadmap. *IEEE 39th International Conference on Distributed Computing Systems, ICDCS*, Dallas, TX, USA. pp. 1754–1764, doi: 10.1109/ICDCS.2019.00174.
- Viswanathan, H., & Mogensen, P. E., (2020) Communications in the 6G Era. *IEEE Access*, 8, pp. 57063-57074, doi: 10.1109/ACCESS.2020.2981745.
- Wang, M., Zhu, T., Zhang, T., Zhang, J., Yu, S. & Zhou, W., (2020). Security and privacy in 6G networks: New areas and new challenges. *Digital Communications and Networks*, 6(3), pp. 281-291, <https://doi.org/10.1016/j.dcan.2020.07.003>.
- Zhou, Y., Liu, L., Wang, L., Hui, N., Cui, X., Wu, J., Peng, Y., Qi, Y., & Xing, C., (2020). Service-aware 6G: An intelligent and open network based on the convergence of communication, computing and caching. *Digital Communications and Networks*, 6(3), pp. 253-260, <https://doi.org/10.1016/j.dcan.2020.05.003>.

Chapter 10

DIVERSE APPROACHES TO RING SPINNING FOR HIGH QUALITY YARN PRODUCTION AND INCREASED PRODUCTIVITY

Banu NERGIS¹

¹ Professor Dr., Technical University of Istanbul, Textile Engineering Department, ORCID ID:
0000-0001-6010-6497

“A staple-spun yarn is a linear assembly of many fibres in the cross-section and along the length, held together usually by the insertion of twist to form a continuous strand, small in diameter but of any specified length.” (McIntyre, 1995). Spun yarns are produced using one of the major spinning processes presented in Table 1.

Table 1. Classification of major short staple spinning systems (Matsuo, 2008)

Short Staple Spinning	
Real Twisting Method	Ring Spinning
	Rotor Spinning
Open-End Twisting Method	Friction Spinning
	Air Jet-Vortex Spinning

The most relevant spinning systems are ring spinning, rotor spinning and air-jet/vortex spinning with a market share of 65%, 30% and 2-5%, respectively. Ring-spinning accounts for about two third of long and short staple yarns produced globally (Anonymous, 2019).

The success of ring spinning can be attributed to the superior quality, remarkable strength, and evenness of ring yarns over those produced by other systems. Ring spinning also offers high versatility in terms of yarn count and fiber type (Zahidul, 2019). On the other hand, the problems associated with ring spinning are high power consumption, high yarn tension and, low production speed mainly resulting from the friction between the ring and the traveller (Lawrence, 2010).

The generated heat due to friction elevates the traveller temperature which, at extreme conditions, results in the breakage of the yarn or even the traveller. Traveller speed is limited in order to avoid such failure. The heat problem can be overcome either by reducing its generation or dissipating the generated heat out of the traveller rapidly. For doing so, such approaches as the use of rings and/or travellers with different shapes, sizes, modified surfaces or use of rotating rings were proposed in various research and development studies. Some researcher even tried to cool the ring by refrigeration (Begum, 2011).

On the other hand, hairiness, which occurs unavoidably during spinning, is one of the important yarn properties that affects the processing and quality of the yarns. During the past decades, a great deal of attention was paid to improve ring spun yarns' quality, and to achieve higher production rates. Compact (aerodynamic or mechanic), Jetring (Air-Plus Ring Tandem), Compact-Jet, Siro, Siro-Jet, Compact Siro, Solo, Siro-Solo, Pro-Spin, Nu-Torque, Offset, Mismatch, Sirofil, Contact, Agent Aided Spinning Systems

and Pre-Twister Process are among the hybrid and spinning triangle modified technologies based on ring spinning, that primarily reduced yarn hairiness, increased abrasion resistance and improved strength (Nergis, 2017; Khan, Begum and Sheikh, 2020).

There is still an ongoing and indispensable effort for improving the quality parameters of ring spun yarns and increasing the production speed. In order to serve the improvements aimed, different modification approaches to ring spinning machines were developed and those proposed, mostly within the final decade, were gathered in this work. It should however, be noted that not all the presented techniques have been launched as commercial machines but the modifications explained would help researchers develop or improve novel approaches.

1. APPROACHES TO DECREASE THE HAIRINESS OF RING SPUN YARNS

1.1 Decreasing Hairiness by Contact Surface Installation

A contact surface installation into the yarn formation zone after the spinning triangle was one of the approaches adopted to reduce yarn hairiness (Fig.1) Presence of the contact surface introduced a re-wrapping effect on the protruding fiber ends and reduced the yarn hairiness. However, despite the improvement achieved for yarn hairiness, unevenness and strength properties of the yarns deteriorated when a contact surface was used (Xia, Xu, Zhang, Qiu and Feng, 2012).

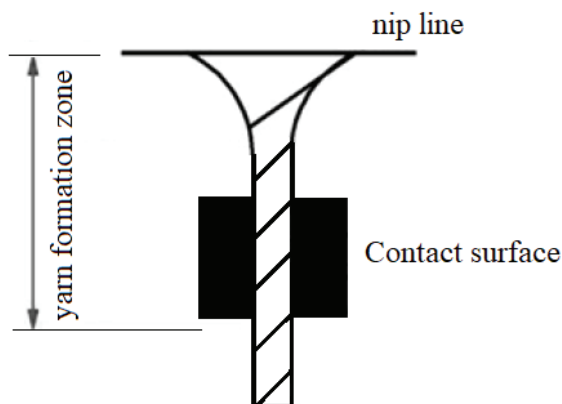


Figure 1. Stationary contact surface installed after the spinning triangle (Xia, Xu, Zhang, Qiu and Feng, 2012)

Aiming to improve the spun yarn properties further, the stationary contact surface was replaced by a rotary grooved cylinder. The decreased frictional force and reduced twist blockage provided by the rotary surface prohibited improper drawing of the drafted strand in the spinning triangle.

So, the yarns produced had better tenacity values. Although similar unevenness values were achieved, hairiness reduction ratio of the yarns spun with the rotary grooved cylinder was significantly lower than that of the corresponding yarn spun with the static grooved one (Yu et.al, 2018).

In another modified method introduced to overcome the deterioration in yarn evenness and insufficient hairiness reduction obtained with the static contact surface, the yarn was passed between a contacting static rod and a self-adjustable disc. The static rod and disc assembly was placed into the yarn formation zone in such a way that the rod was below and the disc was above the yarn. The length of the static rod adopted shortened the contacting length of the strand in comparison to the contact length of the static surface. Self-adjustable disc was able to perform both vertical and rotational motions. The experimental results proved that the yarns produced using a combination of a static rod and adjustable disc surfaces had considerably decreased hairiness values. Despite its good contribution to existing alternative pneumatic compacting systems, the limitation of the proposed arrangement was its more or less twist blocking function (Liu et.al, 2018).

The contacting static rod and self-adjustable disc approach was further improved by varying the manner which the drafted strand contacted the rod and disc surfaces while its passage between them (Xu et al., 2020). Accordingly, the strand either followed a straight, convexing-up or concaving-down route. In case of convexing-up passage form, the strand surrounded the surface of the static rod while partly contacting the self-adjustable disc. On the other hand, in the concaving-down route the strand surrounded the surface of the self-adjustable disc while partly touching the static rod. The results of the tests conducted showed that yarn hairiness was significantly reduced for all contacting modes when compared with the hairiness of conventional yarn and the yarn tenacity was slightly enhanced only for the strands that followed the convexing-up and concaving-down routes.

In another approach, a rotary wheel with a threaded surface with three pitch lengths of 0,3, 0,5 and 0,7 mm was designed and attached 10 mm below the front roller nip line. According to the experimental results, yarn hairiness and tenacity significantly improved when rotary-threaded wheel was used and hairiness reduction ratio gradually decreased as the threaded pitches widened (Xu, et.al, 2021).

1.2 Decreasing Hairiness by Modifying the Yarn Path

In an attempt to produce less hairy ring spun yarns, various approaches have been reported for maintaining horizontal offset of the spinning triangle by deflecting the path of the yarn from the drafting arrangement to the bobbin. There is an asymmetric fibre distribution in the spinning triangle and the direction of the offset seems to play an important role

in determining the hairiness of the yarns. Although there are opposing opinions whether right or left offset of the yarn path is the most effective one for reducing hairiness, this simple geometric modification of the spinning triangle offered successful results.

For achieving a left diagonal path, Rajwin, Prakash, and Vimal (2018) used the mismatching approach and diverted the yarn towards left by guiding the yarn to the adjacent spindle on the left side (Fig. 2). Right diagonal path of the yarn was achieved by guiding the yarn to the adjacent right side spindle. Yarn hairiness, evenness, tenacity, elongation and breaking force of the conventional and compact ring yarns spun by the left diagonal path were better than those properties of the yarns that followed straight and right paths during their production. 30-39% reduction were observed in the hairiness of the yarns produced with left diagonal path.

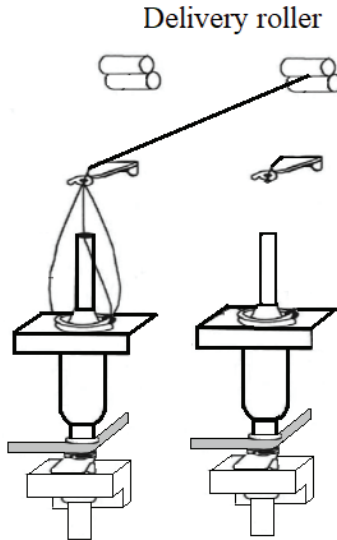


Figure 2. Left diagonal path arrangement (Rajwin, Prakash and Vimal, 2018)

Despite the fact that it provided high hairiness reduction, the mismatching approach also had the potential to cause problems such as excessive offset or empty spindle. So, a pair of offset device that can change the horizontal offset of the spinning triangle was adopted on a spinning machine, between the front roller and the yarn guide. In the arrangement, two round guides, inserted in two slots, could be moved freely to change the horizontal offset (Fig. 3). It was reported that the “Z” twisted spun yarn hairiness reduced by applying appropriate right horizontal offset of spinning triangle, where “S” twisted yarn hairiness reduced by selecting appropriate left offset (Liu and Su, 2016).

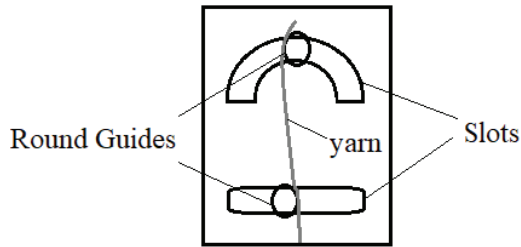


Figure 3. Round guides in horizontal slots

Various offset distances were also achieved by shifting a traverse guide, placed between the delivery roller and the pig tail, on horizontal axis (Fig. 4). The yarn leaving the front roller nip was threaded through the traverse guide and the diagonal path provided by offsetting the guide affected the hairiness of the yarns but quite different effects were observed for left and right diagonal paths. 3-9 mm long hairs of the yarns, which followed right diagonal path during production, reduced a great amount. For the right offset arrangement, 12 mm proved to be the optimum value as the offset distance (Wu, Xie, Su, Liu and Huang, 2011).

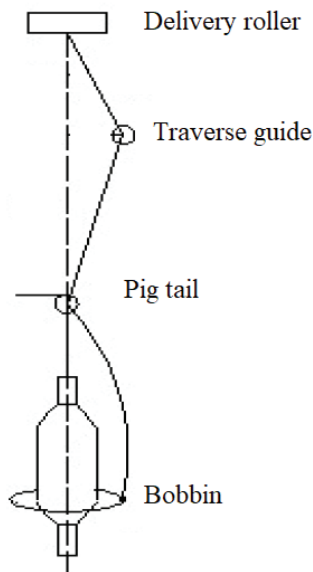


Figure 4. Offsetting by traverse guide (Wu, Xie, Su, Liu and Huang, 2011)

35° angle offset in the spinning triangle was obtained by moving the position of the twisting unit relative to the nipping point of the drafting arrangement exit roller by Singh, Gordan and Wang (2018). According to the results they obtained using this arrangement, right offset proved to be effective in reducing hairiness for a Z-twist yarn while left offset deteriorated hairiness results.

1.3 Decreasing Hairiness by Pre-Twisting (Low Torque Spinning)

Advantages such as reduced twist liveliness, less hairiness and higher strength at lower twists, soft handle and lower fabric spirality after washing and tumble-drying processes are offered by yarns producing low torque ring spinning approach. For producing such yarns, ring spinning system is modified by incorporating a false twister/pre-twister into the yarn path between the front roller and yarn guide. The patented technique proposed by Tao, Xu and Wong (2004) can be considered as the base for the following approaches in which ring spinning system is modified by employing a false twister/pre-twister in the yarn formation zone.

By using an additional twisting element after the drafting arrangement, the yarn path is divided into two zones after the spinning triangle (Fig.5) (Yang, Tao, Xu and Lam, 2007).

Zone I, from the yarn formation point to the false twister, is the high-twist zone, due to the amount of false twist given in Z direction by the false twister.

Zone II, on the other hand, is the low twist zone, from the false twister to ring, traveler and spindle. In this zone, the same amount of false twist in reverse direction is immediately introduced as the yarn passes the false twister. At the same time, true twist propagates from the traveler and interacts with false twist, forming the final single yarn.

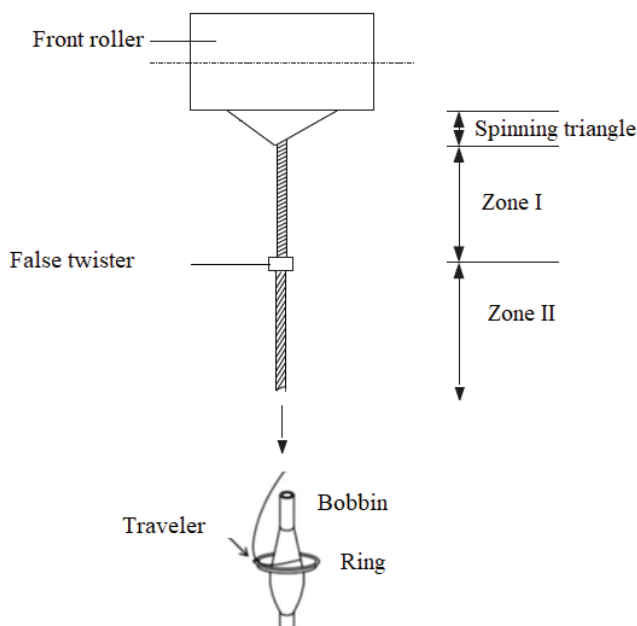


Figure 5. Twist zones after the spinning triangle (Yang, Tao, Xu and Lam, 2007)

In Table 2, various approaches used for producing the so-called low torque yarn by employing different false/pre-twisters on the ring spinning machine are presented.

Table 2. Different approaches for producing yarns using a pre-twister

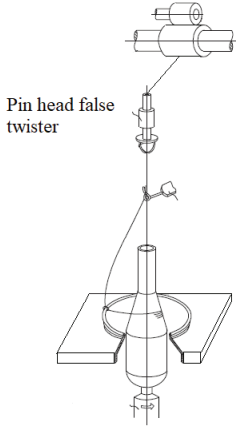
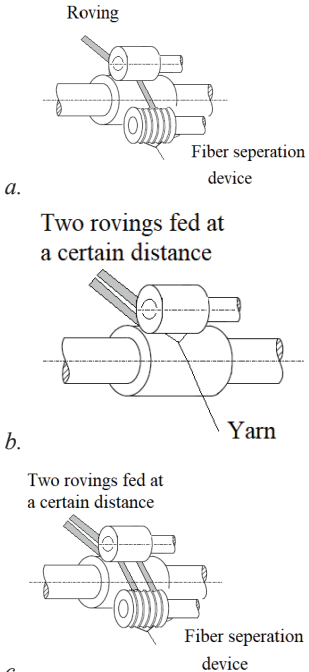
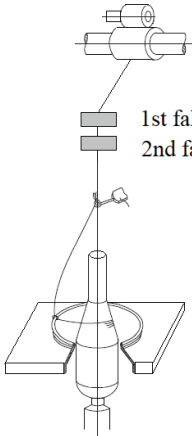
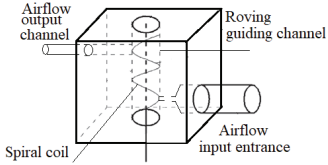
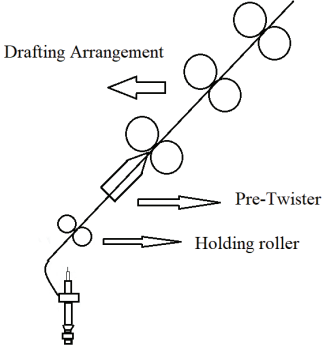
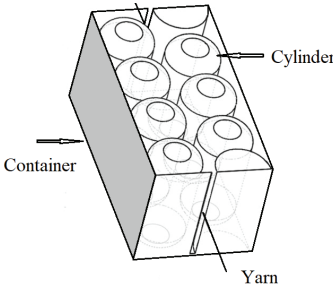
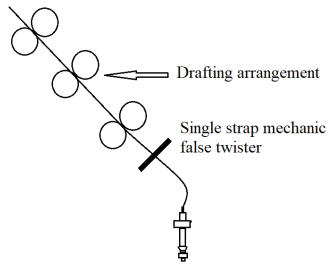
	Type of pre-twister used	Figure	Results obtained
(Yang, Tao, Xu and Lam, 2007)	The conventional ring spinning system was equipped with a pin false twister that was driven by a couple rotor.	 <p>Pin head false twister</p> <p>Figure 6</p>	Modified low twist yarn had relatively high strength and low residual torque. The use of low residual yarn has the potential to solve the spirality problem of the single jersey fabrics.
(Xu and Tao, 2008).	The pin false twister with three fiber feeding approaches were employed: a. A fiber separation device, which splitted the drafted strand into many sub-assemblies of fibers, was used. b. Two strands of rovings parallel to each other at a certain distance were fed. c. Combination of 1&2.	 <p>Roving</p> <p>Fiber separation device</p> <p>a. Two rovings fed at a certain distance</p> <p>b. Two rovings fed at a certain distance</p> <p>c. Two rovings fed at a certain distance</p> <p>Fiber separation device</p> <p>Yarn</p> <p>Figure 7</p>	Each fiber feeding approach offered its own advantages and, in general, the modified yarns had low twist with sufficient strength for good spinning and knitting performance.

Table continued.

<p>(Ying et.al, 2015).</p>	<p>Two false twisters rotating in reverse directions were incorporated in the new modified spinning system.</p>	 <p>Figure 8</p>	<p>22,5% and 28,7% twist reductions were achieved for single and plied yarns, respectively. Even with the reduced twist, the modified yarns had better tenacity, hairiness, wet snarling and IPI values that the conventionally produced ones.</p>
<p>(Liu and Xuzhong, 2017).</p>	<p>An air nozzle having a vortex guiding channel was designed in which the twist can be produced by the high-pressure air vortex. The nozzle was placed after the front rollers.</p>	 <p>Figure 9</p>	<p>The results showed that different benefits were achieved for Z and S twisted yarns when the airflow direction was switched from clockwise to anticlockwise.</p>
<p>(Wang, Xue and Cheng, 2018).</p>	<p>A pre-twister, which was located very close to the front roller nip, and a holding roller were added to the system. Compressed air supplied from four nozzles of the pre-twister maintained the false twist effect.</p>	 <p>Figure 10</p>	<p>Although the yarn was weaker than the corresponding conventional ring-spun one, potentially higher productivity was reached.</p>

<p>(Shao, Cheng, Yu, Xu and Wu, 2019).</p>	<p>A dynamic twist-resistant device was placed to the exit of the drafting arrangement. The device consisted of a cylinder and an oscillating container. The twisting torque at the twist point was reduced due to The dynamic normal force acting on the yarn and, the friction between the yarn and the cylinders.</p>	 <p><i>Figure 11</i></p>	<p>Yarns produced by the modified system had better performance in terms of strength and hairiness compared with the conventional ones. The effect of the modified ring-spinning system on evenness was not significant.</p>
<p><i>Table continued.</i></p>			
<p>(Liua, Sua and Song, 2020)</p>	<p>A motor driven single strap that served as a simple mechanical false-twisting device was introduced. The yarn that bypassed the upper or the lower part of the strap produced a false twisting effect.</p>	 <p><i>Figure 12</i></p>	<p>By using the mechanical false-twisting attachment ring, compact and siro yarns were produced. Hairiness and strength of all yarns produced using the attachment improved when compared with those properties of their conventionally produced counterparts.</p>

Other than the arrangements presented in Table 2, Yin, Tao and Xu (2019) used a single friction-belt, polyurethane or polyester, for achieving the false twist effect. Studying the impact of the material type, surface roughness, hardness and diameter of the friction belt on yarn properties revealed that shortening the interactive path of the false-twisting unit resulted in a significant reduction of yarn imperfections, especially neps. The yarns, produced by the modified process, that gave the optimum

results apparently outweighed the conventional yarns in hairiness with a 11,1% twist reduction.

Gulsevincler, Usal and Yilmaz (2020) suggested the use of an air humidification system which was connected to the pneumatic distributor that supplied air to the nozzle placed into the yarn formation zone. According to the obtained results, supply of humid air to the nozzle displayed a slight positive effect on yarn hairiness, irregularity, elongation and tenacity.

Liu and Su (2013) employed an airflow false twisting device on a sirospinning system and by doing so, modified the geometry of primary and final spinning triangle (Fig.13). When the spun yarns produced by the modified system were analyzed, it was shown that increased airflow pressures distributed the tensile and compressive stresses more uniformly within the yarn, and thus the yarn torque decreased correspondingly.

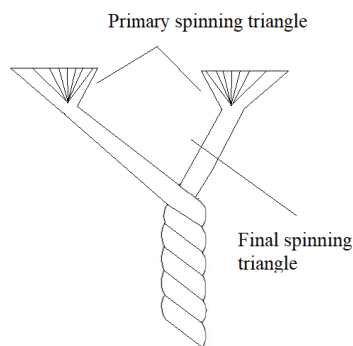


Figure 13. Spinning triangles of Sirospun system (Yin, Tao and Xu, 2019)

As another approach based on low torque ring spinning, a two-step spinning (twisting-and-untwisting) process was proposed by Xu, Ta, and Wong (2014). Accordingly, two separate steps namely, one for producing a highly twisted yarn on ring spinning machine and another one for untwisting the spun yarn on a twisting machine, were carried out. In the first step, a ring yarn at a higher twist (nT , T is a nominal twist) was produced where in the next step, opposite twist of $(n-1)T$ was inserted on a twisting machine. The results obtained for yarns produced by the two-step spinning process showed that they had slightly higher tenacity, lower wet snarling tendency and much less hairiness than the conventional yarns. However, on the other hand, yarn properties of the yarns were inferior to those of yarns produced by a low torque spinning method.

1.4 Decreasing Hairiness by Other Novel Approaches

Embeddable and locatable spinning (ELS) was another novel spinning method proposed for producing super-fine worsted yarns, improving the yarn quality and increasing fiber utilization (Xu et.al., 2011).

The system was designed in such a way that each staple strands could be reinforced by the filaments, and staple fibers could be well embedded into the body of the resultant yarn. The three approaches for producing the ELS yarn structure was as follows:

1. The filaments were fed between the two staple strands at a certain distance away from the corresponding strand.
2. The staple strands and the corresponding filaments were overlapped.
3. The filaments were located at the outer position and the two staple fiber strands were fed between them.

Results of the study, in which water-soluble polyvinyl alcohol filaments were used, showed that the third approach was the best alternative for eliminating yarn hairs.

In another approach, liquid water was employed as the humidification medium for reducing yarn hairiness during ring spinning. The so-called agent-aided system (AAS) developed was located into the yarn formation zone between the front roller nip and the yarn guide (Fig. 14). The system was composed of two components namely, one container full of pure water and one self-rotating cylinder connected with a speed motor above the container. The cylinder has direct contact with the drafted strand in the yarn formation zone and the lower part of it was submerged in water. The whole surface of the cylinder was covered with water due to the high-speed rotation of the cylinder and the viscous shear effect of liquids. Upon contact of the cylinder to the strand and through the relatively small surface tension of liquid water, the surface of the fibers became wet. The results revealed that use of the AAS system effectively improved yarn properties and ring yarns with obviously reduced hairiness could be spun (Li, Guo, Sun and Gao, 2019).

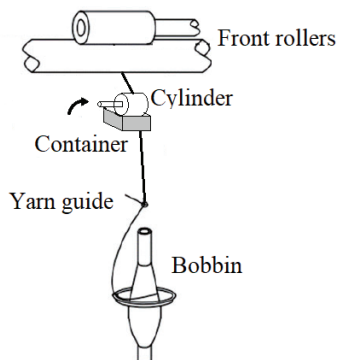


Figure 14. Container and self-rotating cylinder of agent-aided system (Li, Guo, Sun and Gao, 2019)

In an attempt to further improve the ring spun yarn properties by using the agent-aided system, sodium carboxymethyl cellulose (CMC-Na), which easily dissolves in pure water under room temperature, was used as an adhesive. Effect of the the ratio of the linear surface velocity of the self-rotating cylinder to the yarn output speed and the CMC-Na concentration was observed. It has been found that a slightly faster linear surface velocity of the cylinder compared with the yarn speed resulted in a reduction in the yarns hairiness while the higher agent concentration contributed to a higher breaking strength and lower breaking elongation. Sodium carboxymethyl cellulose concentration of 0.7% also significantly reduced yarn hairiness (Li, Guo, Sun and Gao W, 2020).

Another approach called “soft drafting system” SDS was proposed in which the drafting system of the ring spinning machine was modified. A flexible lattice apron and two magnetically fixed curved plates replaced the aprons and formed a curve-shaped channel shown to control the movement of fibers. Results of the tests conducted showed that the soft drafting system improved yarn evenness and reduced the number of frequently occurring yarn faults (Cui, Song, Cheng, Deng W and Ji, 2021).

2. APPROACHES TO INCREASE THE PRODUCTION SPEED OF RING SPINNING

In an attempt to reduce the friction between the ring and the traveller and hence, the heat generated, Begum (2011) proposed three set-ups in which the ring and the traveller were vibrated at various frequency, amplitude and velocities. In the proposed arrangements, vibration was generated either by using an unbalanced rotating mass, by to and fro movement of a small shaft or by using transverse motion of a small shaft in the radial direction of the ring. The latter arrangement that produced the forced vibration with transverse direction motion generated the most effective vibration and provided a reduction of yarn tension as well as co-efficient of friction of up to 25%. Friction generated temperature, on the other hand, reduced by 16%. The reduction in the friction between the ring and the traveller and, the heat generated allowed about 5-10% increase in the speed of the traveller. The vibration applied had no adverse effects on the total quality of the yarns produced.

In order to overcome the limitations in the production rate imposed by the different forces involved in the ring/traveller system, the concept of Magnetic spinning was proposed by Abdel-hady, Mogahzy, AbuElenin and Abdel-Kader (2006). The introduced system was based on magnetic suspension, where a lightweight rotor suspended magnetically and span freely inside a fixed stator. By this approach, the ring/traveler system was replaced by a floating ring with an eyelet on its inner surface. The floating ring revolved by

the action of yarn passing through the eyelet and the ring was kept suspended in space by the active magnetic levitation system (Fig.15).

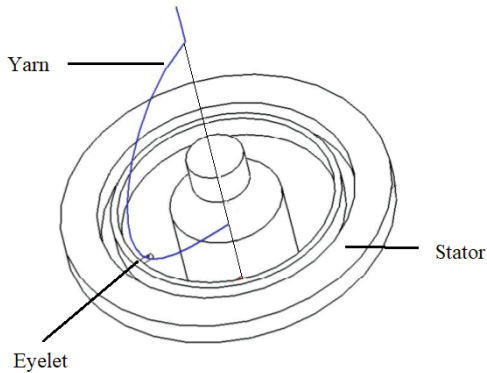


Figure 15. Magnetically suspended ring in magnetic spinning - (Abdel-hady, Mogahzy, AbuElenin and Abdel-Kader, 2006).

A superconductor loses all its electrical resistance to a great extent when cooled below a certain temperature. In principle, superconductors allow electrical current to flow without losing energy. Quantum levitation is, on the other hand, is a process where the properties of quantum physics is used to levitate an object, especially, a superconductor over a magnetic source (Jones, 2019a; 2019b). According to the principles of superconducting levitation, the permanent magnet ring of the developed system levitates and rotates above the superconductor ring freely upon cooling the superconductor below its transition temperature (Jones, 2019a; 2019b).

In order to overcome the complexity and high maintenance requirement of the magnetically suspended ring, a magnetic bearing system based on superconducting technology, which consisted of a circular superconductor and permanent magnet ring, was proposed (Hossain et.al., 2014; 2015; 2018).

The two designs of superconducting magnetic bearing (SMB) installed on the conventional ring-spinning machine were as follows (Fig. 16):

1. A magnetic ring rotated coaxially over a superconductor ring and the permanent magnet ring levitated above superconductor coaxially.
2. A magnetic ring rotated coplanarly inside the superconductor ring and the permanent magnet levitated inside the superconductor coplanarly.

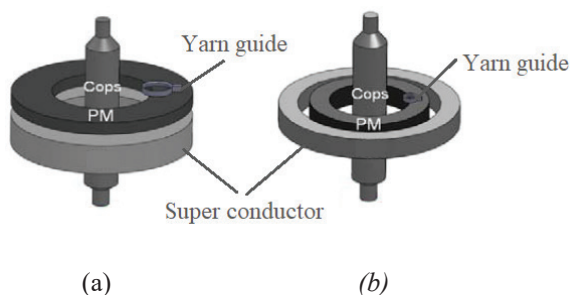


Figure 16. Superconducting magnetic bearing positioning concepts (a) coaxially placed, (b) coplanerly placed (Hossain et.al., 2014; 2015; 2018).

Coaxial placement had the advantage concerning dimension of cops in twisting zone in comparison to that of coplaner placement. The yarns spun by using coaxial configuration was less hairy, more even and had reduced irregularity. The dynamic yarn behavior of the system presented great potential to double the productivity in comparison to existing spinning machines especially for thermoplastic materials.

3. CONCLUSIONS

The ongoing attempts for raising the performance of the ring spinning technology and enhancing the yarn properties result in the development of various diversified approaches proposed by researchers. The proposed technologies, which mainly aim at modifying the yarn formation zone and traveller/ring assembly, seem to be promising in improving the performance of ring yarns.

REFERENCES

- Abdel-hady F., Mogahzy Y.E., AbuElenin S. and Abdel-Kader R. (2006). Innovative Approach To High-Speed Spinning Using A Magnetically-Elevated Spinning Ring. *AUTEX Research Journal*, 6, 3, 113-121.
- Anonymous. (2019). *Global Spinning Machinery Market Growth-2019-2024* <https://www.fiormarkets.com/report/global-spinning-machinery-market-growth-2019-2024-381790.html>
- Begum H.A. (2011). Effect of Vibration on The Twisting Rate of Ring Spinning For The Production of Yarn. (Ph.D Thesis). Mechanical Engineering, Bangladesh University of Engineering and Technology.
- Cui Y., Song H., Cheng L., Deng W. and Ji Y. (2021). Experimental study of a modified drafting system based on the ring spinning frame. *Textile Research Journal First Published January 12*, <https://doi.org/10.1177/0040517520984977>
- Feng J., Xu B., Tao X., and Wong C. (2014). Performance of Cotton Single Yarns and Knitted Fabrics Produced by a 2-Step Spinning Method. *Fibers and Polymers*, 15, 4, 882-890.
- Gulsevindir E., Usal M.R. and Yilmaz D. 2020. The Effect of Humidified Air on Yarn Properties in a Jet-Ring Spinning System. *Tekstilec*, 63, 4, 294–304.
- Hossain M., Abdkader A., Cherif C., Sparing M., Berger D., Fuchs G. and Schultz L. (2014). Innovative twisting mechanism based on superconducting technology in a ring-spinning system. *Textile Research Journal*, 84, 8, 871–880
- Hossain M., Sparing M., Berger D., Abdkader A., Berger D., Fuchs G., , Cherif C., Schultz L. (2015). Prototype ring spinning tester with superconducting magnetic bearing system for high productivity. *ITMA 2015 release*-www.itma.com.
- Hossain M., Abdkader A., Cherif C., Berger A., Sparing M., Hühne R., Schultz L., Nielsch K. (2018). Potential of High Performance Ring Spinning Based on Superconducting Magnetic Bearing. *World Academy of Science, Engineering and Technology International Journal of Industrial and Manufacturing Engineering*, 12, 5, 512-516.
- Jones A.Z. (2019a, January 11). *How Quantum Levitation Works*. <https://www.thoughtco.com/quantum-levitation-and-how-does-it-work-2699356>.
- Jones A.Z. (2019b, May 30). *Superconductor Definition, Types, and Uses*. <https://www.thoughtco.com/superconductor-2699012>.
- Khan K.R.K., Begum H.A. and Sheikh R. (2020). An Overview on the Spinning Triangle Based Modifications of Ring Frame to Reduce the Staple Yarn Hairiness. *Journal of Textile Science and Technology*, 6, 19-39.
- Klein W. (1995). *The technology of short-staple spinning : manual of textile technology*. The Textile Institute.

- Lawrence C.A. (Editor). (2010). *Advances in Yarn Spinning Technology*. A volume in Woodhead Publishing Series in Textiles.-
- Li P., Guo M., Sun F. and Gao W. (2019). Reducing yarn hairiness in ring spinning by an agent-aided system, *Textile Research Journal*, 89 (21–22), 4438–4451.
- Li P., Guo M., Sun F. and Gao W. (2020). An adhesive-aided ring spinning for improving cotton yarn quality with the aid of sodium carboxymethyl cellulose solution. *Journal of Engineered Fibers and Fabrics*, 15, 1–13
- Liu X. and Su X. (2013). Research on Sirospun yarn torque using airflow false twisting device. *Journal of The Textile Institute*, 104:5, 473-480, DOI: 10.1080/00405000.2012.743648.
- Liu X. and Su X. (2016). Yarn Hairiness on Ring Spinning with Modified Yarn Path. *Indian Journal of Fiber and Textile Research*, 41, 221-225
- Liu X and Xuzhong S. (2017). Research on flow field in a modified ring spinning system with the air nozzle. *The Journal of The Textile Institute*, 108:4, 489-499, DOI: 10.1080/00405000.2016.1171480.
- Liu K., Xia Z., Xu W., Hao Y., Xu B Q., Jin W. and Ni J. (2018). Improving spun yarn properties by contacting the spinning strand with the static rod and self-adjustable disk surfaces. *Textile Research Journal*, Vol. 88(7), 800–811.
- Liua X., Sua X. and Song J. (2020) Research on yarn qualities modified by mechanical false-twisting device. *The Journal of The Textile Institute*,. 111, 4, 529–539.
- McIntyre, J.E. (1995). *Textile Terms and Definitions*, The Textile Institute, Manchester, UK.
- Matsuo T. (2008). Innovations in Textile Machine and Instrument. *Indian Journal of Fiber & Textile Research*, 33, 288-202.
- Nergis B.U. (2017). An Overview of Hybrid Ring Spinning Methods. *Curr Trends Fashion Technol Textile Eng. 1*(5), 555572.
- Rajwin, A. J., Prakash C., and Vimal J. T. (2018). Effect of diagonal path on the physical properties of compact and conventional ring yarn. *Indian Journal of Fibre & Textile Research*, 43, 495-498.
- Shao R., Cheng L., Yu Y., Xu J. and Wu J. (2019). Research on the mechanism of the modified ring-spinning system using a dynamic twist-resistant device and its yarn quality. *Textile Research Journal*, 89(15), 3169–3177.
- Singh C. Gordon S. and Wang X. (2018). The mechanism of hairiness reduction in offset ring spinning with a diagonal yarn path. *Textile Research Journal*, 89, 8, 1546–1556.
- Tao, X.M., Xu, B.G. and Wong, S.K., (2004). Method and Apparatus for Manufacturing a Singles Ring Yarn, US Patent: 02/06/2004, US 7096655

- Xia Z., Xu W., Zhang M., Qiu W., and Feng F. (2012). Reducing Ring Spun Yarn Hairiness via Spinning with a Contact Surface. *Fibers and Polymers*, 13, 5, 670-674.
- Xu B.G. and Tao X.M. (2008). Techniques for Torque Modification of Singles Ring Spun Yarns. *Textile Research Journal*, 78(10), 869–879 DOI: 10.1177/0040517507087684.
- Xu D., Fan H., Jiang H. , Yang S., Ni J, Zhang X., ... (2020). Comparative Analysis on the Properties of Yarns Formed by Different Contact-shaped Strands Passing through Static Rod and Self-adjustable Disk Surfaces. *Journal of Natural Fibers*, DOI: 10.1080/15440478.2020.1821277
- Xu W., Xia Z., Wang Z., Chen J., Cui W., Ye W., Ding C. and Wang X. (2011). Embeddable and Locatable Spinning. *Textile Research Journal*, 81(3), 223–229.
- Xu D., Fan H., Li J., YangW. , Liu K. and Xu W. (2021). Comparative Analysis of the Properties of Yarn Spun by Rotary Threaded Surfaces with Different Pitches. *Journal of Natural Fibers*, DOI: 10.1080/15440478.2020.1870630.
- Wang K., Xue W. and Cheng L. (2018). A Numerical and Experimental Study on a Pre-Twisted Ring Spinning System. *Polymers*, 10, 671; doi:10.3390/polym10060671
- Wu T., Xie C., Su X., Liu X. and Huang B. (2011). A Modified Ring Spinning System with Various Diagonal Yarn Path Offsets, *Procedia Engineering*, 18, 1 – 6
- Yang K., Tao X.M., Xu B.G. and Lam J. (2007). Structure and Properties of Low Twist Short-staple Singles Ring Spun Yarns. *Textile Research Journal*, 77(9), 675–685 DOI: 10.1177/0040517507080545.
- Yin R., Tao X.M. and Xu B. (2020). Yarn and fabric properties in a modified ring spinning system considering the effect of the friction surface of the false-twister. *Textile Research Journal*, 90 (5–6), 572–580.
- Ying G., Jie F., Rong Y., Xungai W., Sluijs M. and Xiaoming T. (2015). Investigation and evaluation on fine Upland cotton blend yarns made by the modified ring spinning system. *Textile Research Journal*, 85(13,) 1355–1366.
- Yu H., Liu K., Jun C., Fu C., Xia Z. and Xu W. (2018). Comparative study of ring yarn properties spun with static and rotary grooved contact surfaces. *Textile Research Journal*, 88(16) 1812–1823.
- Zahidul I. (2019). Comparing Quality Parameters of Yarn Produced by Ring, Rotor, and Compact Spinning System. *European Scientific Journal January edition*, 15, 3, 1857- 7431.

Chapter 11

TENDER EVALUATION MODELS IN PUBLIC CONSTRUCTION WORKS AND CONSULTANCY SERVICES

Burak ÖZ¹

¹ Asst Prof. Dr. Burak Öz, Zonguldak Bulent Ecevit University, Faculty of Engineering,
Department of Civil Engineering, 0000-0003-0686-1410

1. INTRODUCTION

Public authorities and institutions are subject to the Public Procurement Law No. 4734 in tenders to be made using public funds, however, works such as flat received by land owner for which public funds are not used, or demolition works in return for scrap are not covered in this Law (Public Procurement Law,2002).

Public procurements consist of construction works, goods and services. Three different procedures are used for these procurements. The open tender is a procedure by which all tenderers who meet the specified qualification criteria can submit their tenders. In the restricted tender, only prequalification tenderers to be invited by the contracting authority can submit their tenders. The negotiated Procedure can only be used in special cases specified by Public Procurement Law (Public Procurement Law, 2002).

The Public Procurement Law covers different models for the evaluation of the qualifications and tenders. The qualification criteria to be required from candidates or tenderers vary depending on the volume of the work, the tender procedure and the type of procurement. The economically most advantageous tender is determined only on the basis of price offers or by considering the non-price factors (qualitative or quantitative) together with the price offers. At the same time, in the both methods, a price advantage of up to 15% can be applied in favor of the domestic tenderers. The contracting authority calculates the limit value to determine abnormally low prices. The contracting authority has three options based on the estimated cost of the procurement; the tender is awarded to the most economically advantageous tender regardless of the limit value or the tenders below the limit value are rejected without asking for written explanation, or the tenderers whose written explanations are found insufficient are rejected (Public Procurement Law,2002, Public Procurement General Communiqué, 2019).

Although the qualification and evaluation processes of tenders are similar according to the procurement procedures, it also includes differences. The most significant difference is seen in the consultancy service procurements. In this study, tender evaluation models in public construction works and consultancy services in compliance with Turkish Public Procurement Law No. 4734 and relevant regulations will be examined (Public Procurement Law, 2002).

2. TENDER EVALUATION PROCEDURES

There are three procedures: The first is known as the open procedure in which all tenderers meeting the specified qualification criteria can submit their tenders. The second is known as the restricted procedure where only prequalified and invited tenderers can submit their tenders. The

third is known as negotiated procedure in which the contracting authority negotiates with the tenderers about the technical details, implementation methods and, in some cases, the price (Public Procurement Law, 2002).

2.1 Open Procedure

All tenderers who meet the specified qualification criteria can submit their tenders. Tenders will be evaluated after all tenders are submitted. This procedure can be subdivided into the following steps (Public Procurement Law, 2002, Public Procurement General Communiqué, 2019):

- Publishing tender notice.
- Receiving qualification documents and price offers together.
- Evaluating qualification criteria.
- Rejecting not qualified tenderers.
- Evaluating the tenders and deciding the most economically advantageous tender.
- Awarding a contract.

2.2 Restricted Procedure

Only prequalified tenderers invited by the contracting authority can submit their tenders. This procedure can be subdivided into the following steps (Public Procurement Law, 2002, Public Procurement General Communiqué, 2019):

- Publishing for prequalification notice.
- Receiving potential tenderers' prequalification documents.
- Evaluating prequalification criteria.
- Rejecting not prequalified tenderers.
- Inviting all prequalified potential tenderers or having a short list of the potential tenderers.
- Inviting a certain number of the potential tenderers among prequalified tenderers in the short list.
- Receiving tenders.
- Evaluating the tenders and deciding the most economically advantageous tender.
- Awarding a contract.

2.3 Negotiated Procedure

This procedure can only be used in special cases specified by Public Procurement Law. This procedure can be subdivided into the following

steps (Public Procurement Law,2002, Public Procurement General Communique, 2019):

First Option:

- Publishing tender notice (not mandatory).
- Inviting at least 3 tenderers.
- Receiving qualification documents and price offers together.
- Evaluating qualification criteria.
- Rejecting not qualified tenderers.
- Evaluating initial tender prices.
- Invitation for final tender prices.
- Evaluating the tenders and deciding the most economically advantageous tender.
- Awarding a contract.

Second Option:

- Publishing tender notice.
- Receiving qualification documents.
- Evaluating qualification criteria.
- Rejecting not qualified tenderers.
- Receiving tenders, such as technical details and implementation methods regarding to the contract.
- Negotiation to find the best methods and solutions.
- Receiving initial tender prices based on the clarified specifications.
- Evaluating initial tender prices.
- Invitation for final tender prices.
- Evaluating the tenders and deciding the most economically advantageous tender.
- Awarding a contract.

3. MODELS IN PUBLIC CONSTRUCTION WORKS

There are two models. The first model is used for the open procedure and the negotiated procedure in special cases. The second model is used for the restricted procedure, which consists of two stages. Tenderers are determined to be invited to tender in the first stage and tenders are evaluated in the second stage (Public Procurement Law,2002, Public Procurement General Communique, 2019):

3.1 First Model

The first step of this model is to determine decision criteria based on the volume of construction work and to evaluate qualification criteria that must be satisfied in Table 1 and Table 2. If tenderers fail to meet the minimum requirements, they will be rejected from the tendering process. The second step is to evaluate the tenders and to decide the most economically advantageous tender. If more than one tender is equal, the tender is finalized by looking at the work experiences (Construction Works Tender Implementation Regulation, 2019, Type Administrative Specification for Construction Works in Open Tenders 2019)

Table 1. Documents for the economic and financial capability

Criteria	Volume			Condition
	$EC < ThV/10$	$ThV/10 \leq EC < ThV/2$	$EC \geq ThV/2$	
Bank statement.	NR	O	O	$\geq TP * 0.10$ $\geq EC(0.05-0.15)^1$
Current ratio.	NR	O	R	≥ 0.75
Equity capital ratio.	NR	O	R	≥ 0.15
The ratio of short-term bank debt to shareholder equity.	NR	O	R	< 0.50
Tenderer's overall turnover showing its business volume.	NR	O	R	$\geq TP * 0.25$
Tenderer's turnover concerning construction works.	NR	O	R	$\geq TP * 0.15$
¹ The contracting authority decides on the ratio between the indicated ranges; EC: Estimated cost; ThV: Threshold value; TP: Tender price; NR: Not required; O: Optional; R: Required.				

Table 2. Documents for the professional and technical ability

Criteria	Volume		Condition	
	$EC < ThV * 2$	$EC \geq ThV * 2$	$EC < ThV * 2$	$EC \geq ThV * 2$
Operating as a registered member of the related chamber.	R	R	Mandatory	
Legally authorised to submit tenders.	R	R	Mandatory	
Experiences in works contracts and in services contracts linked to construction works (completed or ongoing).	R	R	$\geq TP * (0.50-1.00)^1$	$\geq TP * (0.50-0.80)^1$
			$\geq EC * (0.50-1.00)^2$	$\geq EC * (0.50-0.80)^2$
Organizational structure and adequate number of staff.	O	O	The contracting authority specifies the number, title and qualification.	

Machinery, devices and other equipment required to perform the contract.	<i>O</i>	<i>O</i>	The contracting authority specifies the number, type and capacity.
Quality management system certification.	<i>NR</i>	<i>O</i>	Available/Unavailable
Environmental management system certification.	<i>NR</i>	<i>O</i>	Available/Unavailable
^{1,2} The contracting authority decides on the ratio between the indicated ranges; <i>EC</i> : Estimated cost; <i>ThV</i> : Threshold value; <i>TP</i> : Tender price; <i>NR</i> : Not required; <i>O</i> : Optional; <i>R</i> : Required.			

3.2 Second Model

Firstly, the qualification criteria are determined based on the volume of construction works, then weights of the economic and financial capability and the professional and technical ability are selected between 40 and 100, 100 points in total. Requirements and conditions of the evaluation criteria are shown in Table 3 and Table 4. The determined criteria of each candidate are measured based on the economic and financial capability scores (Eq. 1.1 through 1.6), and the professional and technical ability scores (Eq. 1.7 and 1.8). Calculated scores of each candidate are unified and then multiplied with relative weights (Eq. 1.9 or 1.10 and Eq. 1.11). After the results of the multiplication for each candidate are aggregated into one overall score (Eq. 1.12), the potential tenderers will be ranked according to their scores. Thus, tenderers who have the maximum financial capability and technical qualification to perform a specific project will be elected and only a certain number of qualified candidates will be invited to submit their tenders. If the number of candidates to be invited to tender is less than five, the tender is canceled (Type Prequalification Specification for Construction Works in Restricted Tenders, 2019).

Table 3. Documents for the economic and financial capability of potential tenderers

Criteria		Requirement	Condition
<i>BS</i>	Bank statements	<i>O</i>	$\geq EC^*(0.05-0.15)^1$
<i>CR</i>	Current ratio	<i>R</i>	≥ 0.75
<i>ECR</i>	Equity capital ratio	<i>R</i>	≥ 0.15
<i>DR</i>	The ratio of short-term bank debt to shareholder equity	<i>R</i>	< 0.50
<i>OT</i>	Overall turnover showing business volume	<i>R</i>	$\geq EC^*(0.25-0.35)^1$
<i>TCW</i>	Turnover concerning construction works	<i>R</i>	$\geq EC^*(0.15-0.25)^1$
¹ The contracting authority decides on the ratio between the indicated ranges; <i>O</i> : Optional; <i>R</i> : Required.			

Table 4. Documents for the professional and technical ability of potential tenderers

Criteria		Volume		Condition	
		$EC < ThV * 2$	$EC \geq ThV * 2$	$EC < ThV * 2$	$EC \geq ThV * 2$
<i>MC</i>	Operating as a registered member of the related chamber.	<i>R</i>		Mandatory	
<i>LA</i>	Legally authorised to submit tenders.	<i>R</i>		Mandatory	
<i>E</i>	Experiences in works contracts and in services contracts linked to construction works (completed or ongoing) within the last fifteen years.	<i>R</i>		$EC * (0.50 - 1.00)^1$	$EC * (0.50 - 0.80)^1$
<i>EEE</i>	Total of three experiences in works contracts and in services contracts linked to construction works (completed or ongoing) within the last fifteen years.	<i>O</i>		$3 * EC * (0.50 - 1.00)^1$	$3 * EC * (0.50 - 0.80)^1$
<i>OS</i>	Organizational structure and adequate number of staff.	<i>O</i>		The contracting authority specifies the number, title and qualification.	
<i>MDE</i>	Machinery, devices and other equipment required to perform the contract.	<i>O</i>		The contracting authority specifies the number, type and capacity.	
<i>QMC</i>	Quality management system certification.	<i>NR</i>	<i>O</i>	Available/Unavailable	
<i>EMC</i>	Environmental management system certification.	<i>NR</i>	<i>O</i>	Available/Unavailable	

¹ The contracting authority decides on the ratio between the indicated ranges;
EC: Estimated cost; *ThV*: Threshold value; *NR*: Not required; *O*: Optional; *R*: Required.

3.2.1 Scoring The Economic And Financial Capability (S_{EFC}):

$$S_{BS} = \begin{cases} 0 & BS < EC * BSR \\ \frac{0.10}{EC * BSR} * (BS - EC * BSR) + 0.10 & EC * BSR \leq BS \leq 2 * EC * BSR \\ 0.20 & BS > 2 * EC * BSR \end{cases} \quad (1)$$

Where S_{BS} is the bank statement score, BS is bank statements, EC is the estimated cost and BSR is the bank statement ratio (Type Prequalification Specification for Construction Works in Restricted Tenders, 2019).

$$S_{CR} = \begin{cases} 0 & CR < 0.75 \\ \frac{0.10}{0.75} * (CR - 0.75) + 0.10 & 0.75 \leq CR \leq 1.50 \\ 0.20 & CR > 1.50 \end{cases} \quad (2)$$

Where S_{CR} is the current ratio score and CR is the current ratio (Type Prequalification Specification for Construction Works in Restricted Tenders, 2019).

$$S_{ECR} = \begin{cases} 0 & ECR < 0.15 \\ \frac{0.10}{0.15} * (ECR - 0.15) + 0.10 & 0.15 \leq ECR \leq 0.30 \\ 0.20 & ECR > 0.30 \end{cases} \quad (3)$$

Where S_{ECR} is the equity capital ratio score and ECR is the equity capital ratio (Type Prequalification Specification for Construction Works in Restricted Tenders, 2019).

$$S_{DR} = \begin{cases} 0 & DR > 0.50 \\ \frac{0.10}{0.25} * (0.50 - DR) + 0.10 & 0.25 \leq DR \leq 0.50 \\ 0.20 & DR < 0.25 \end{cases} \quad (4)$$

Where S_{DR} is the ratio of short-term bank debt to shareholder equity and DR is the ratio of short-term bank debt to shareholder equity (Type Prequalification Specification for Construction Works in Restricted Tenders, 2019).

$$S_{OT} = \begin{cases} 0 & OT < EC * OTR \\ \frac{0.10}{EC * OTR} * (OT - EC * OTR) + 0.10 & EC * OTR \leq OT \leq 2 * EC * OTR \\ 0.20 & OTR > 2 * EC * OTR \end{cases} \quad (5)$$

Where S_{OT} is the score of overall turnover showing business volume, OT is the overall turnover showing business volume, EC is the estimated cost and OTR is the overall turnover ratio (Type Prequalification Specification for Construction Works in Restricted Tenders, 2019).

$$S_{TCW} = \begin{cases} 0 & TCW < EC * TCR \\ \frac{0.10}{EC * TCR} * (TCW - EC * TCR) + 0.10 & EC * TCR \leq TCW \leq 2 * EC * TCR \\ 0.20 & TCW > 2 * EC * TCR \end{cases} \quad (6)$$

Where S_{TCW} is the score of turnover concerning construction works, TCW is turnover concerning construction works, EC is the estimated cost and TCR is the turnover ratio (Type Prequalification Specification for Construction Works in Restricted Tenders, 2019).

3.2.2 Scoring The Professional And Technical Ability (S_{PTA}):

$$S_E = \begin{cases} 0 & E < EC * ER \\ \frac{0.25}{EC * ER} * (E - EC * ER) + 0.25 & EC * ER \leq E \leq 2 * EC * ER \\ 0.50 & E > 2 * EC * ER \end{cases} \quad (7)$$

Where S_E is the experience (completed or ongoing) score, E is the experience (completed or ongoing), EC is the estimated cost and ER is the experience ratio (Type Prequalification Specification for Construction Works in Restricted Tenders, 2019).

$$S_{EEE} = \begin{cases} 0 & EEE < 3 * EC * ER \\ \frac{0.25}{3 * EC * ER} * (EEE - 3 * EC * ER) + 0.25 & 3 * EC * ER \leq EEE \leq 6 * EC * ER \\ 0.50 & EEE > 6 * EC * ER \end{cases} \quad (8)$$

Where S_{EEE} is the score of the total of three experiences, EEE is the total of three experiences, EC is the estimated cost and ER is the experience ratio. Note that the document showing EEE of a potential tenderer to submit is optional. If not submitted, the potential tenderer is not excluded from tender but will be deprived of the additional score (Type Prequalification Specification for Construction Works in Restricted Tenders, 2019).

3.2.3 Calculating Overall Scores of Potential Tenderers (OS):

For one potential tenderer:

$$S_{EFC_1} = W_{EFC} (S_{BS} + S_{CR} + S_{ECR} + S_{DR} + S_{OT}) \quad (9)$$

$$S_{EFC_2} = W_{EFC} (S_{BS} + S_{CR} + S_{ECR} + S_{DR} + S_{TCW}) \quad (10)$$

$$S_{PTA} = W_{PTA} (S_E + S_{EEE}) \quad (11)$$

$$OS = (S_{EFC_1} \text{ or } S_{EFC_2}) + S_{PTA} \quad (12)$$

Where OS is the overall score for each potential tenderer, W_{EFC} is the weight of the economic and financial capability and W_{PTA} is the weight of the professional and technical ability. Note that candidates are allowed to submit either OT or TCW (Type Prequalification Specification for Construction Works in Restricted Tenders, 2019).

Finally, tenders are evaluated and the most economically advantageous tender is found. If the number of tenders is less than three, the tender is canceled (Type Administrative Specification for Construction Works in Restricted Tenders 2019).

4. MODELS IN CONSULTANCY SERVICES

Consultancy service procurements are frequently applied by contracting authorities during the preparation of contracts and the performing of contracts for construction works. At the stage of preparation of a contract such as surveying, engineering and architectural projects, technical specifications, estimating quantity of the work and the cost and at the stage of performing of a contract such as supervision and controlling might be procured from consultancy service providers. There are two models. In the first model, contracting authorities have two options to use; the open procedure and the negotiated procedure. In the second model, the restricted procedure must be used (Tender Implementation Regulation for Consultancy Service Procurements, 2019, Type Prequalification Specification for Consultancy Service Procurements, 2019, Type Administrative Specification for Consultancy Service Procurements, 2019)

4.1 First model

When the estimated cost is up to four times the upper value established for services, either the open procedure or the negotiated procedure in special cases can be used in this model. In the other case, the second model must be used. The economic and financial capability of tenderers (Table 5) is not evaluated in this model. However, tenderers who only meet the qualification criteria determined for measuring the professional and technical abilities (Table 6) will be evaluated. Then the price offers are evaluated (Tender Implementation Regulation for Service Procurements, 2019, Type Administrative Specification for Service Procurements in Open Tenders 2019),

Table 5. Documents for the evaluation of economic and financial capability

Criteria	$EC < UV * 4$
Bank statement.	NR
Current ratio.	NR
Equity capital ratio.	NR
The ratio of short-term bank debt to shareholder equity.	NR
Tenderer's overall turnover showing its business volume.	NR
Tenderer's turnover concerning services.	NR
EC: Estimated cost; UV: Upper value established for services; NR: Not required.	

Table 6. Documents for the evaluation of professional and technical ability

Criteria	Volume	Condition
	$EC < UV * 4$	
Legally authorised to submit tenders.	R	Mandatory
Operating as a registered member of the related chamber.	R	Mandatory
Experiences in consultancy service procurements within last five years or in consultancy service contracts linked to construction works (completed or ongoing) within the last fifteen years.	R	$\geq EC * (0.25-0.50)^1$
Organizational structure and adequate number of staff.	NR	Must not
Machinery, devices and other equipment required to perform the contract.	O	Available/Unavailable
Quality management system certificate.	O	Available/Unavailable
Environmental management system certificate.	O	Available/Unavailable
Service qualification certificate.	O	Available/Unavailable
Quality competence of test-analysis-calibration laboratories and inspection organizations.	O	Available/Unavailable
¹ The contracting authority decides on the ratio between the indicated ranges; EC: Estimated cost; UV: Upper value established for services; R: Required; NR: Not required; O: Optional.		

4.2 Second model

Regardless of the estimated cost, it is mandatory to use the restricted procedure in this model. This model consists of five stages (Tender Implementation Regulation for Consultancy Service Procurements 2019, Type Prequalification Specification for Consultancy Service Procurements 2019):

- Controlling documents submitted by candidates.
- General competency.
- Evaluation of the prequalification criteria.
- Scoring financial capacity and technical skills.
- Evaluating the tenders.

Controlling documents submitted by candidates: If the required documents submitted by the candidates are missing or do not comply with the required conditions, candidates are excluded from the evaluation. Documents to be used in the evaluation of the financial capacities and technical skills are shown in Table 7 and Table 8.

Table 7. Documents for evaluation of the financial capacity

Prequalification criteria		Volume		Condition
		$EC < ThV$	$EC \geq ThV$	
BS	Bank statements.	O	R	$EC^*(0.05-0.15)^1$
CR	Current ratio.	O	R	≥ 0.75
ECR	Equity capital ratio.	O	R	≥ 0.15
DR	The ratio of short-term bank debt to shareholder equity	O	R	< 0.50
OT	Overall turnover showing its business volume.	R		$\geq EC^*(0.25-0.35)^1$
TCS	Turnover concerning consultancy services.	R		$\geq EC^*(0.15-0.25)^1$
¹ The contracting authority decides on the ratio between the indicated ranges; EC : Estimated cost; ThV : Threshold value; O : Optional; R : Required.				

Table 8. Documents for evaluation of technical skills

Prequalification criteria		Volume		Condition	
		$EC < ThV$	$EC \geq ThV$	$EC < ThV$	$EC \geq ThV$
AL	Application letter	R		Mandatory	
MC	Operating as a registered member of the related chamber.	R		Mandatory	
LA	Legally authorised to submit tenders.	R		Mandatory	
E	Experiences in consultancy service procurements within last five years or in consultancy service contracts linked to construction works (completed or ongoing) within the last fifteen years.	R		$\geq EC^*(0.25-0.50)^1$	
				for the top score: $EC^*(0.50-1.00)^1$	
OS	Organizational structure and adequate number of staff.	R		$KTP \leq 2$	$KTP \leq 4$
				$PE \leq 10\text{ years}$	
				$SE \leq 5\text{ years}$	
MDE	Machinery, devices and other equipment required to perform the contract.	O		The contracting authority specifies the number, type and capacity	
QMC	Quality management system certification.	O		Available/Unavailable	

¹ The contracting authority decides on the ratio between the indicated ranges;
 EC : Estimated cost; ThV : Threshold value; O : Optional; R : Required.
 KTP : Key technical personnel; PE : Professional experience; SE : Similar experience.

General competency: Required documents to evaluate general eligibilities of the candidates are; an application letter, a document proving that the tenderer is operating as a registered member of the related chamber and is legally authorised to submit tenders, a statement of signature or signatory circular showing that the candidate is authorized, documents regarding general service experience, and prequalification documents. If the candidate is a joint venture, partnership statement is requested. If the number of candidates meeting the general eligibility requirements is less than three, the tender will be canceled (Tender Implementation Regulation for Consultancy Service Procurements 2019, Type Prequalification Specification for Consultancy Service Procurements 2019)

Evaluation of the prequalification criteria: The candidates who have meet the general eligibility must satisfy the conditions of prequalification criteria shown in Table 7 and Table 8. Disqualified candidates are excluded from the evaluation process. If the number of candidates who meet the prequalification criteria is equal to or less than the number of candidates to be shown in the procurement document, the candidates are invited to submit their tenders. If not so, the candidates are scored based on the financial capacity and technical skills (Tender Implementation Regulation for Consultancy Service Procurements 2019, Type Prequalification Specification for Consultancy Service Procurements 2019)

Scoring financial capacity and technical skills: The contacting authority determines the top scores of each criterion to be used to evaluate the financial capacity and technical skills of candidates with a total score of 100 as shown in Table 9 before the tender (Tender Implementation Regulation for Consultancy Service Procurements 2019, Type Prequalification Specification for Consultancy Service Procurements 2019)

Table 9. Scores of criteria for the financial capability and technical ability of candidates

Evaluation criteria and sub-criteria		Top Scores
Evaluation criteria of the financial capability ¹		10-30
<i>OT</i>	Overall turnover	[.....]
<i>TCS</i>	Turnover concerning consultancy services	[.....]
Evaluation criteria of the technical ability ²		70-90
<i>OE</i>	Overall experience	[.....]
<i>E</i>	Experience in similar fields to the contract	[.....]
<i>KTP</i>	Key technical personnel	[.....]
<i>MDE</i>	Machinery, devices and other equipment required to perform the contract	[.....]
<i>QMC</i>	Quality management system certification	[.....]
Total		100
¹ Candidates are allowed to submit either <i>OT</i> or <i>TCS</i> , so the top score of <i>OT</i> or <i>TCS</i> must be between 10 and 30.		
² Total of the top scores of <i>OE</i> , <i>E</i> , <i>OS</i> , <i>MDE</i> (if required) and <i>QMC</i> (if required) must be between 70 and 90.		

The procurement commission first scores the technical ability of each qualified candidate based on evaluation criteria of the technical ability (Eq. 2.1 through Eq. 2.8) and then the financial capability of each qualified candidate based on evaluation criteria of the financial capability (Eq. 2.9 and Eq. 2.10). The scores of the technical ability and financial capability of each candidate are aggregated into one score (Eq. 2.11 through Eq. 2.13). Then the candidates are ranked according to their scores and a short list including minimum three and maximum ten candidates selected among prequalified ones is made for submitting tenders in alphabetic order (Tender Implementation Regulation for Consultancy Service Procurements 2019, Type Prequalification Specification for Consultancy Service Procurements 2019)

4.2.1 Scoring The Technical Ability (S_{TA})

$$S_{OE} = \begin{cases} s_top & OE > 20 \\ s_2 & 10 < OE \leq 20 \\ s_1 & 5 < OE \leq 10 \\ s_min & 0 < OE \leq 5 \end{cases} \quad (13)$$

Where S_{OE} is the overall experience score and OE is the overall experience. Note that all scores of OE (s_top , s_2 , s_1 and s_min) are determined by the contracting authority and shown in the procurement document (Tender Implementation Regulation for Consultancy Service Procurements 2019, Type Prequalification Specification for Consultancy Service Procurements 2019)

$$\frac{s - s_min}{s - ER_1} * (E - ER_1) + s_min \quad EC * ER_1 \leq \quad (14)$$

Where S_E is the similar experience score, E is the similar experience, EC is the estimated cost, ER_1 is the similar experience ratio₁ is determined by the contracting authority between 0.25 and 0.50, and ER_2 is the similar experience ratio₂ is determined by the contracting authority between 0.50 and 1.00 (Tender Implementation Regulation for Consultancy Service Procurements 2019, Type Prequalification Specification for Consultancy Service Procurements 2019)

For each key person;

$$S_1^{PE} = \begin{cases} s_{top} & PE \geq PEY_2 \\ \frac{s_{top} - s_{min}}{PEY_2 - PEY_1} * (PE - PEY_1) + s_{min} & PEY_1 \leq PE < PEY_2 \\ 0 & PE < PEY_1 \end{cases} \quad (15)$$

Where PE is the professional experience, PEY_1 is the contracting authority determines the number of professional experience years for one key person providing at most 10 years and PEY_2 is the contracting authority determines the number of professional experience years for the top score for one key person (Tender Implementation Regulation for Consultancy Service Procurements 2019, Type Prequalification Specification for Consultancy Service Procurements 2019)

For each key person;

$$S_1^{SE} = \begin{cases} s_{top} & SE \geq SEY_2 \\ \frac{s_{top} - s_{min}}{SEY_2 - SEY_1} * (SE - SEY_1) + s_{min} & SEY_1 \leq SE < SEY_2 \\ 0 & SE < SEY_1 \end{cases} \quad (16)$$

Where SE is the similar experience, SEY_1 is the contracting authority determines the number of similar experience years for one key person providing at most five years and SEY_2 is the contracting authority determines the number of similar experience years for the top score for one key person (Tender Implementation Regulation for Consultancy Service Procurements 2019, Type Prequalification Specification for Consultancy Service Procurements 2019)

$$S_{OS} = \sum_{i=1}^k (S_i^{PE} + S_i^{SE}) \quad (17)$$

Where k is the total staff number

For each equipment;

$$S_1^{MDE} = \begin{cases} s_top & MDE \geq N_2 \\ \frac{s_top - s_min}{N_2 - N_1} * (MDE - N_1) + s_min & N_1 \leq MDE < N_2 \\ 0 & MDE < N_1 \end{cases} \quad (18)$$

Where MDE is the number of owned or rented machinery, devices and other equipment, N_1 is the contracting authority determines the number of equipment for minimum score and N_2 is the contracting authority determines the number of equipment for top score (Tender Implementation Regulation for Consultancy Service Procurements 2019, Type Prequalification Specification for Consultancy Service Procurements 2019)

$$S_{MDE} = \sum_{j=1}^q (S_j^{MDE}) \quad (19)$$

Where q is the total equipment number.

$$S_{QMC} = \begin{cases} s_top & yes \\ 0 & no \end{cases} \quad (20)$$

Where S_{QMC} is the score of the quality management system certification.

4.2.2 Scoring the financial capacity (S_{FC})

$$S_{OT} = \begin{cases} s_top & OT \geq OTR_2 \\ \frac{s_top - s_min}{OTR_2 - OTR_1} * (OT - OTR_1) + s_min & OTR_1 \leq OT < OTR_2 \\ 0 & OT < OTR_1 \end{cases} \quad (21)$$

Where OT is the overall turnover, OTR_1 is the overall turnover ratio₁ is determined by the contracting authority between 0.25 and 0.35, and OTR_2 is the overall turnover ratio₂ is determined by the contracting authority between 0.35 and 0.50 (Tender Implementation Regulation for Consultancy Service Procurements 2019, Type Prequalification Specification for Consultancy Service Procurements 2019)

$$W_{TE} = \begin{cases} 0.78 - 0.80 & TTS > 29 \\ 0.74 - 0.77 & 23 \leq TTS \leq 29 \\ 0.70 - 0.73 & 0 \leq TTS \leq 22 \end{cases} \quad (26)$$

Where W_{TE} is the technical evaluation weight and TTS is the total technical score.

$$W_{FE} = 1 - W_{TE} \quad (27)$$

Where W_{FE} is the financial evaluation weight.

In the first stage, each member of the procurement commission (decision makers) individually scores the technical evaluation scoring criteria, which is shown in Table 11, to determine the technical scores of the tenderers Type Administrative Specification for Consultancy Service Procurements ,2019)

Table 11. Technical evaluation scoring for a tenderer

Scoring criteria	Score range
A. The experience of similar characteristics and scale	10-20
B. The method proposed for the job and the organisational structure	30-50
a. How to do the job
b. Work schedule
c. Compliance of the organizational structure with the work schedule
d. Management and quality control techniques (optional)
e. Equipment
f. Other criteria according to the characteristics of the job
C. The managerial team and the technical staff	30-50
a. General characteristics
b. Eligibility for the job
c. Local experience and knowledge of Turkish language
Total	100

Then, the technical evaluation scores given by all tender commission members are brought together and the average technical evaluation score of the tenderer is calculated (Eq. 2.16). If the tenderer's score falls below the specified threshold score ($70 \leq \text{Threshold} \leq 80$), that tenderer is disqualified and excluded from the evaluation. After that the normalized technical evaluation scores of tenderers are calculated (Eq. 2.17) Type Administrative Specification for Consultancy Service Procurements, 2019)

$$S_i^{TE} = \left(\frac{1}{m} \sum_{c=1}^m S_c^{TE} \right) \geq \text{Threshold} \quad (28)$$

Where S_i^{TE} is the technical score of a tenderer, i is the i th tenderer ($3 \leq i \leq 10$), m is the number of a procurement commission (decision makers), which consists of at least five members and in odd numbers and threshold is the minimum technical score which the contracting authority decides on the threshold score between 70 and 80 ($70 \leq \text{Threshold} \leq 80$) Type Administrative Specification for Consultancy Service Procurements, 2019)

$$NS_i^{TE} = \frac{S_i^{TE}}{\max S_i^{TE}}, \max S_i^{TE} = \max \{S_1^{TE}, S_2^{TE}, \dots, S_i^{TE}\}, 3 \leq i \leq 10 \quad (29)$$

Where NS_i^{TE} is the normalized technical score of the i th tenderer, and $\max S_i^{TE}$ is the maximum of average technical evaluation scores.

In the second stage, financial scores of tenderers are evaluated using Eq. 2.18. If specified in the procurement documents, up to 15% price advantage to domestic tenderers can be applied Type Administrative Specification for Consultancy Service Procurements, 2019),

$$NS_i^{PO} = \frac{\min S_i^{PO}}{S_i^{PO}} * 100, \min S_i^{PO} = \min \{S_1^{PO}, S_2^{PO}, \dots, S_i^{PO}\}, 3 \leq i \leq 10 \quad (30)$$

Where NS_i^{PO} is the normalized financial score of i th tenderer, $\min S_i^{PO}$ is the minimum of the price offers and S_i^{PO} is the price offer of the i th tenderer.

Finally, in the last stage the normalized technical and financial scores of tenderers are multiplied by the their weighted coefficients and then they are added to calculate the tenderers' total scores (Eq. 2.19) [9].

$$TS_i = W_i^{TE} * NS_i^{TE} + W_i^{FE} * NS_i^{PO}, 3 \leq i \leq 10 \quad (31)$$

Where TS_i is the total score of i th tenderer, W_i^{TE} is the weighted coefficient for the technical evaluation, NS_i^{TE} is the normalized technical score of i th tenderer, W_i^{FE} is the weighted coefficient for the financial evaluation, and NS_i^{PO} is the normalized financial score of i th tenderer,

The tenderer with the highest total score is invited to negotiate the job description, contractual terms, personnel and financial tender. In case of equality of the total points, the tenderer with a higher financial tender score is invited to negotiate. If the financial tender scores are also equal, the tenderer who has more similar work experience for a single contract

is invited to negotiate. If the conditions are clarified and an agreement is reached at the end of the negotiation, the contract with the agreed conditions is awarded to the tenderer who has the highest total score. If an agreement cannot be reached, the contract is awarded to the tenderer who has the highest total score with the conditions specified in the tender document (Type Administrative Specification for Consultancy Service Procurements, 2019).

5. CONCLUSIONS

It is stated in the Public Procurement Law No. 4734 that the economically most advantageous tender in public procurements (goods, services or construction works) can be determined only on the basis of price offers or by considering the non-price factors together with the price offers in turnkey lump-sum contracts, lump-sum contracts and unit price contracts. It is also stated that such as operation and maintenance costs, cost effectiveness, productivity, quality and technical value can be used as non-price factors which may be quantitative or qualitative. However, determining the conditions regarding the scoring and criteria for these factors are left to the contracting authorities. When the tenders published in the Electronic Public Procurement Platform (EKAP) were examined, it was seen that non-price factors were used rarely in public procurements, and they were never used in construction works with turnkey lump-sum contracts. This may be because of the concern that awarding a contract at a higher price when considering non-price factors may result in the loss of public funds. In addition, in the 2018 Audit Report of Turkish Court of Accounts, it was seriously criticized that there were practices contrary to Turkish Public Procurement Law in the use of non-price factors in the tender evaluation and as a result of this there were public losses (Turkish Court of Accounts 2018 Audit Report, 2019). However, especially in construction works, it is thought that the economically most advantageous tender is determined only on the basis of price offer might disrupt the time-cost-quality balance, so taking into account the non-price factors in addition to the price might increase the quality of the work, prevent or reduce the cost of poor quality that contracting authorities can endure. Therefore, there is a need to develop models that define the scoring and conditions of non-price factors and to provide the relevant legislation and legal infrastructure.

Civil engineers in public or private sectors frequently work in construction works and consultancy services. Therefore, it will be beneficial for civil engineers to be knowledgeable in the process of tender evaluation models and to better manage the tender process. In addition, civil engineers work not only as civil engineers but also as construction or project managers in various public or private projects. It is believed that knowing all the public procurement processes of civil engineers will noticeably increase their own success and the success of their organizations.

REFERENCES

- Public Procurement Law No. 4734 (2002). Official Gazette of the Republic of Turkey (Issue: 24648), <https://www.ihale.gov.tr/Mevzuat.aspx>
- Public Procurement General Communiqué (2019), Official Gazette of the Republic of Turkey (Issue: 30887), <https://www.ihale.gov.tr/Mevzuat.aspx>
- Construction Works Tender Implementation Regulation (2019), Official Gazette of the Republic of Turkey (Issue: 30936), <https://www.ihale.gov.tr/Mevzuat.aspx>
- Type Administrative Specification for Construction Works in Open Tenders (2019), Official Gazette of the Republic of Turkey (Issue: 30936), <https://www.ihale.gov.tr/Mevzuat.aspx>
- Type Prequalification Specification for Construction Works in Restricted Tenders (2019), Official Gazette of the Republic of Turkey (Issue: 30936), <https://www.ihale.gov.tr/Mevzuat.aspx>
- Type Administrative Specification for Construction Works in Restricted Tenders (2019), Official Gazette of the Republic of Turkey (Issue: 30936), <https://www.ihale.gov.tr/Mevzuat.aspx>
- Tender Implementation Regulation for Consultancy Service Procurements (2019), Official Gazette of the Republic of Turkey (Issue: 30887), <https://www.ihale.gov.tr/Mevzuat.aspx>
- Type Prequalification Specification for Consultancy Service Procurements (2019), Official Gazette of the Republic of Turkey (Issue: 30887), <https://www.ihale.gov.tr/Mevzuat.aspx>
- Type Administrative Specification for Consultancy Service Procurements (2019), Official Gazette of the Republic of Turkey (Issue: 30887), <https://www.ihale.gov.tr/Mevzuat.aspx>
- Tender Implementation Regulation for Service Procurements (2019), Official Gazette of the Republic of Turkey (Issue: 30887), <https://www.ihale.gov.tr/Mevzuat.aspx>
- Type Administrative Specification for Service Procurements in Open Tenders (2019), Official Gazette of the Republic of Turkey (Issue: 30887), <https://www.ihale.gov.tr/Mevzuat.aspx>
- Turkish Court of Accounts 2018 Audit Report (2019): General Directorate of State Hydraulic Works, <https://www.sayistay.gov.tr/tr/?p=2&ContentID=12701>

Chapter 12

OVERVIEW OF LINEAR HALBACH ARRAYS AND EFFECT OF PARAMETRIC CHANGES

Serhat KÜÇÜKDERMENÇİ¹

¹ Balıkesir University Faculty of Engineering Department of Electrical and Electronics Engineering,
kucukdermenci@balikesir.edu.tr

1. INTRODUCTION

In 1980 K. Halbach showed that the series of magnets with a certain array created a large magnetic field (MF) on one side and almost no field at all on the other. One-sided magnetic fluxes were introduced by John C. Mallinson (Mallinson, 1973) and the Halbach (HB) array was developed by Kaus HB (Halbach, 1980).

HB arrays can be used in industrial and scientific applications such as magnetic systems of rotating machines, (Z. Q. Zhu & Howe, 2001), nuclear magnetic resonance (NMR) (Klein et al., 2021), electrodynamic suspensions (Kratz & Post, 2002), DC motors (Praveen et al., 2012), magnetic levitation (HTS Maglev) system for rail transport (Jing et al., 2007). Linear configurations of NdFeB magnets based on the HB structure developed for the generation of strong MFs were modeled on a theoretical basis and in some cases experimentally verified (Žežulka et al., 2013). Models were examined of adjustable linear HB structures (Hilton & McMurry, 2012) using the boundary element method through computer simulations. It was used optimization methods (Sarwar et al., 2012) for the design of HB structures to maximize the forces acting on magnetic nanoparticles. HB structures were analyzed (Jae-Seok Choi & Jeonghoon Yoo, 2008) using the finite element numerical optimization method and designed systems consisting of two and three layers of linear magnets suitable for increasing the MF between layers.

The HB array shown in Figure 1 consists of both axially and radially magnetized permanent magnets (PM). As a result of vectorial sums, the magnetic flux becomes concentrated in only one region (Winter et al., 2012), (Jae-Seok Choi & Jeonghoon Yoo, 2008), (Trumper et al., n.d.) and weakens in the other region.

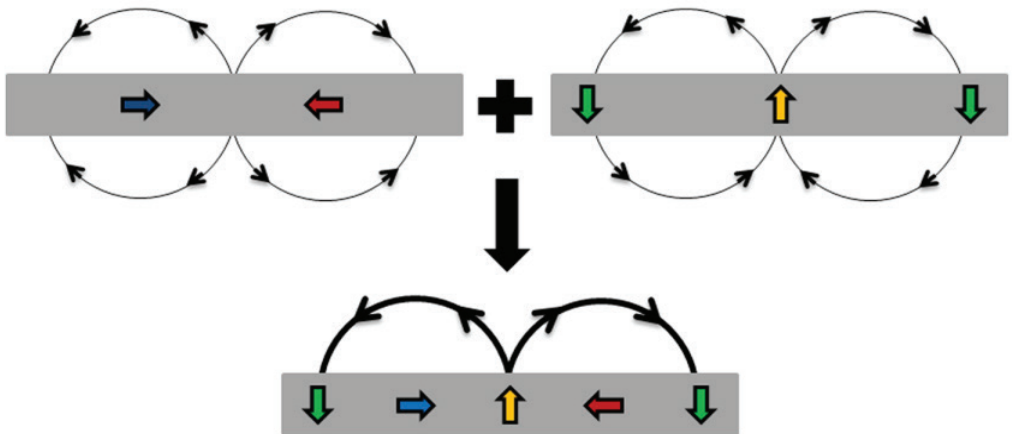


Figure 1. The superposition principle in the linear HB array.

The magnetization model of the HB array can generally be defined by Equations 1a and 1b (Mallinson, 1973) by the superposition of two trigonometric functions:

$$M_x = M \sin(2\pi x/\lambda) \quad (1a)$$

$$M_y = M \cos(2\pi x/\lambda) \quad (1b)$$

where λ denotes the wavelength and M denotes the magnetization amplitude. HB arrays can be linear, planar or cylindrical and have one dominant surface/side. Linear HB arrays are made up of discrete cylindrical or rectangular PMs with differing magnetic orientations resulting in a uniform and strong semi-sinusoidal MF.

Figure 2 shows the magnetization model and magnetic flux density properties for the HB array with 4 magnets.

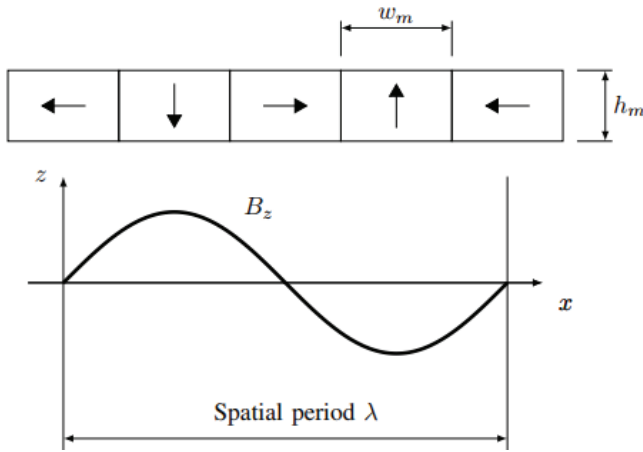


Figure 2. Magnetization model for 4-magnet HB array

The peak value of magnetic flux density at the active surface is given by Equation 2;

$$B = B_r \left(1 - e^{\frac{-2\pi h_m}{\lambda}}\right) \sin\left(\frac{\pi}{n_m}\right) \quad (2)$$

The example given in Figure 3 is defined by the magnet height h_m and the number of magnets per wavelength $n_m = 4$. The rectangular shape is obtained from the wavelength $\lambda = 8 h_m$. B_r now represents the magnetic flux density. As shown in Figure 3, for the distance between two facing HB arrays, the flux density in the normal direction (Gieras et al., 2008) is given by Equation 3;

$$B_z(x, z) = B \sin\left(\frac{2\pi x}{\lambda}\right) \frac{\cosh\left(\frac{2\pi z}{\lambda}\right)}{\cosh\left(\frac{\pi \delta}{\lambda}\right)} \quad (3)$$

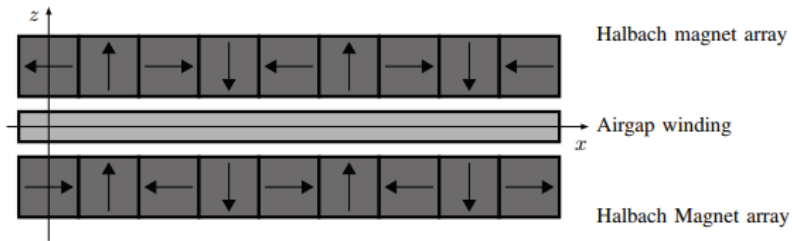


Figure 3. Double sided HB magnet array arrangement

Ideal linear HB array has sine and cosine magnetization in horizontal and vertical directions, respectively. This array results in the absence of a MF on one side and an advanced, purely sinusoidal MF on the other (Shute et al., 2000). Figure 4 (a) shows an ideal HB array. However, it is not practical to produce the ideal HB array. Instead, a series of rectangular or square PMs are used. The practical (non-ideal) four- and eight-part HB array is shown in Figure 4 (b). The non-ideal HB array cannot produce zero MF density on the canceled side and purely sinusoidal MF density on the enhanced side.

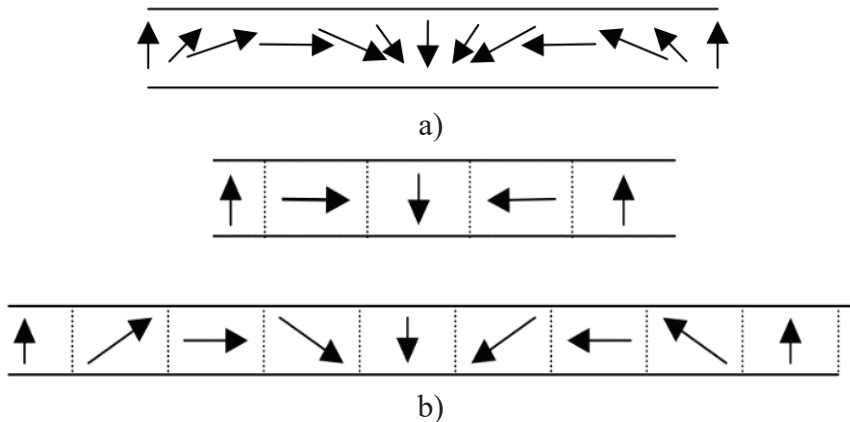
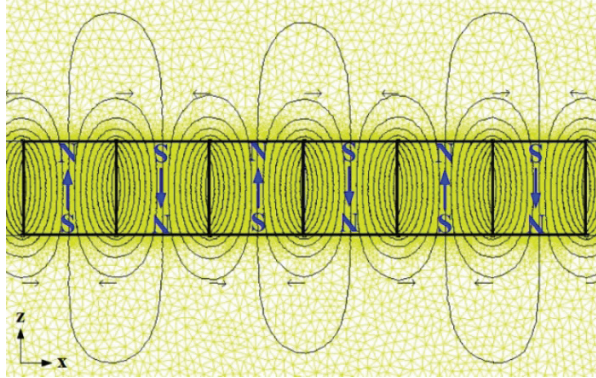


Figure 4. (a) Ideal HB array, (b) HB array of four and eight parts in practice.

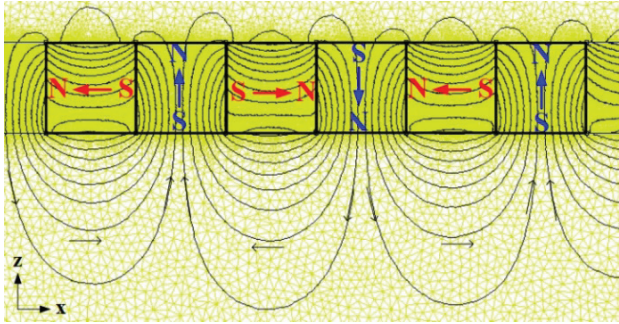
An N-S array with the north poles magnetized in the $+z$ and $-z$ directions respectively and arranged in a dual configuration is shown in Figure 5a. Figures 5b show a HB array of four magnet components instead of two. In addition to the $+z$ and $-z$ components, N poles in the $+x$ and $-x$ directions are included in the array. HB array with the aid of finite element simulation of the two main differences arise in the N-S array:

1) N-S array upper and lower parts have symmetrical MF pattern. The MF in the upper part of the HB array is very weak.

2) According to the N-S array, HB array has a much higher flux rate. HB array is stronger than at the bottom of about $\sqrt{2}$ times the N-S array (Kim & Trumper, 1998). This feature can be used in the design of planar motors that can increase the force density on the strong side to improve the levitation force.



(a) Flux pattern of N-S array



(b) Flux pattern of HB array

Figure 5. N-S array and HB array representation.

2. EFFECTS OF PARAMETRIC CHANGES

2.1 Parametric Changes in Rotation Angles

In an idealized case, the linear HB array will generate a one-sided MF. There are studies on the effect of rotation angles of rods and parametric changes of the distance between them on the MF pattern (Hilton & McMurry, 2012). A setup was set up with NdFeB magnets with a value of $B_r = 1.2$ T. Each bar is 1 cm in diameter, 10 cm in length and separated by a distance of 2.5 mm. A parametric study with rotation angles is shown in Figure 6. In $\Phi = 0$ case, rods are rotated to standard HB array angles and magnetic flux density measurements are taken. Then the same procedure is repeated for $\Phi = \pi / 4$ and $\Phi = \pi / 2$ angle rotations.

In order to observe parametric changes with rotation angles, the situation was examined by rotating the rods around their axes with angles $\Phi = 0$, $\Phi = \pi / 4$ and $\Phi = \pi / 2$ radians. Various types of patterns such as strong MF in the upper region and weak MF in the lower region, symmetrical MF in the upper and lower region, weak MF in the upper region and strong MF in the lower region can be provided by angle changes of the rods. The magnetic flux density plot for each rotation state is shown in Figure 6. For the asymmetric case, it is seen that the magnetic flux density amplitude is between 190-10 mT on the strong side and 30 mT on the weak side. In the symmetrical case, the amplitude is between 70-10 mT for both sides.

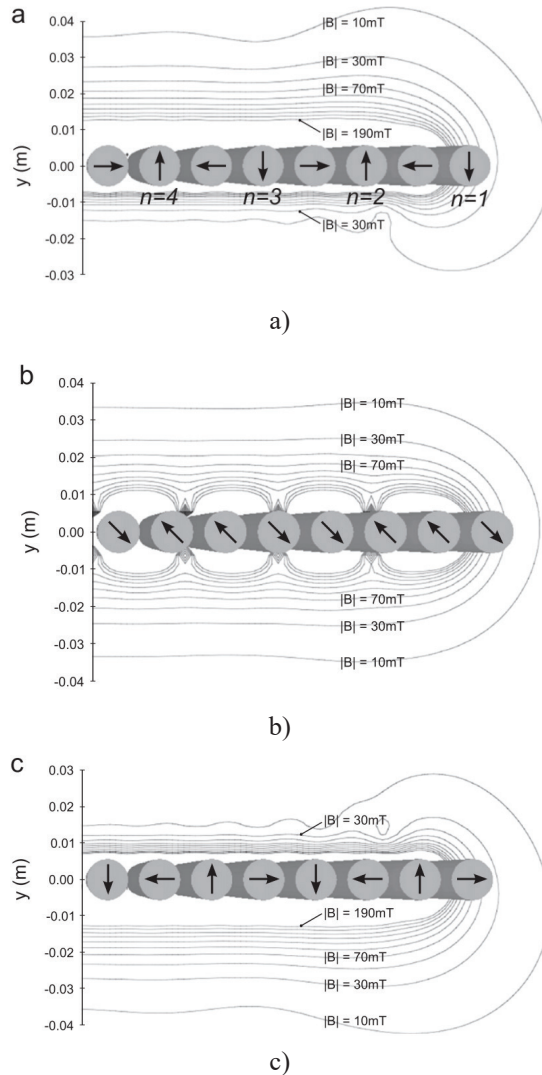


Figure 6. Flux density $[xx]$ for a magnetized rod array with
a) $\Phi = 0$, b) $\Phi = \pi / 4$ and c) $\Phi = \pi / 2$ radian turns (Hilton & McMurphy, 2012).

As seen in Figure 7, the magnetic flux density in the upper and lower parts of the array can be controlled with the help of a simple but effective gear system. Simulations prove that such a system is simple to implement and that the rods would not be subjected to undue torques during rotation. However, mechanical stabilization is needed since the device has no global energy minima. At stable mechanical equilibrium, rods at energy minima have neighbors at energy maxima at unstable equilibria. However, a very simple alternative exists that provides both mechanical stabilization and the potential to alternately rotate rods. This is as simple as using an identical gearing of each rod to its opposing rod.

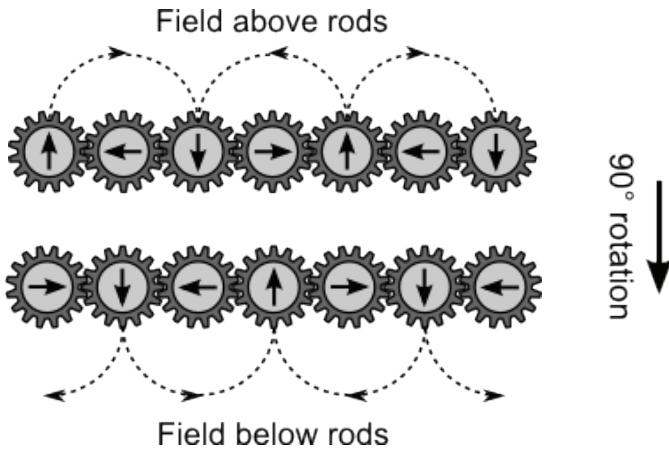


Figure 7. Linear HB array with adjustable angle with gear system

A field confined to one side of the plane of the rods is generated by a series of magnetized rods arranged in the form of Mallinson's flux layer. By rotating the rotation of each rod, the field can be transmitted through the plane. A basic gearing arrangement, as seen schematically in Fig. 7, can be used to transform such an arrangement into a functional unit. A system like this may be used for a variety of things, including mechanical magnetic latching and variable field sources. For free electron laser and synchrotron applications, two such parallel configurations could be used as a variable wiggler magnet.

2.2 Spatial Parametric Changes Between Rods

Figure 8 shows the flux density in the arrangement with bar separations of (a) 25mm, (b) 50mm and (c) 75mm for $\Phi = 0$. It has been observed that increasing the bar separation does not affect the field homogeneity in the central region. It has been observed that as the distance between the rods is increased, the magnetic flux lines just above the rods become fluctuating. For the asymmetric case, it is seen that the magnetic flux density amplitude is between 190-10 mT on the strong side and 30 mT on the weak side. Since

the field has a nonlinear dependence on rod separation, the architecture can be easily optimized. The optimum spacing for maximal field intensity at any chosen vertical position above the rods varies with the vertical position, as can be observed.

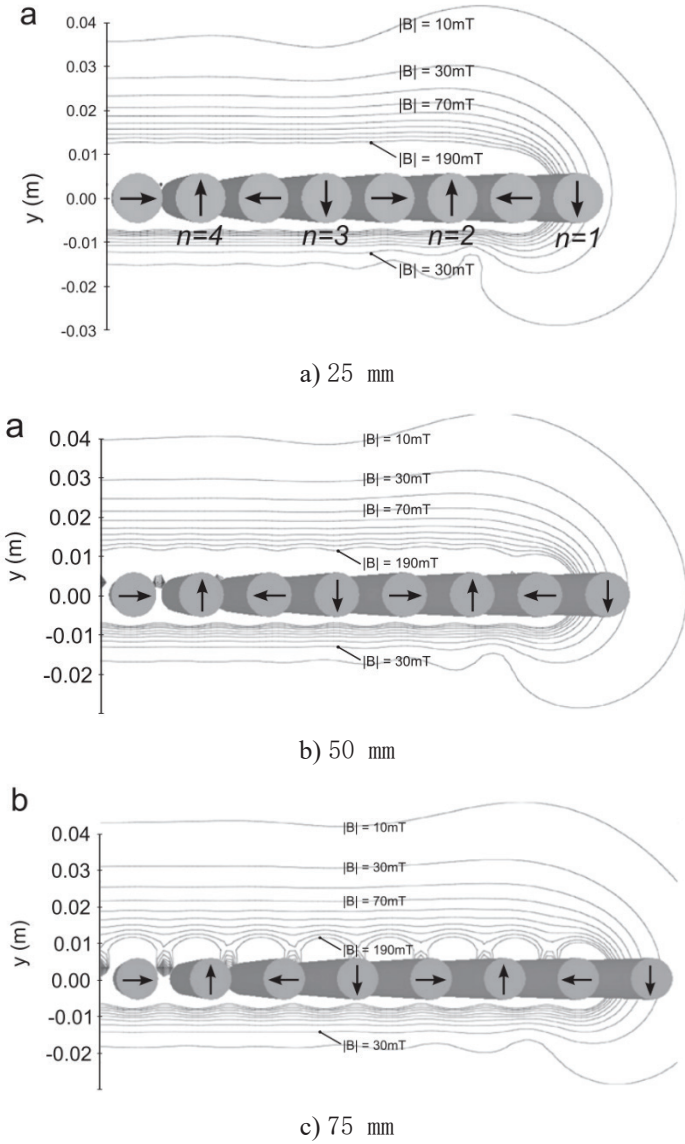


Figure 8. $\Phi = 0$ magnetic flux pattern generated by increasing the distance between the rods (Hilton & McMurry, 2012).

2.3 HB Array in Curved Form

Figure 9 depicts a schematic model of a linear positioned HB array of cylindrical PMs and configurations ranging from 0 to 90 degrees of rotation.

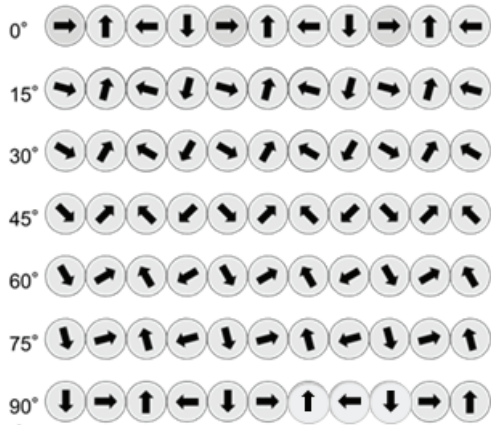


Figure 9. Diagram depicting the analysis model as a function of the PM’s synchronized rotation angle.

Figure 10 depicts two diagrams for each of the round designed HB sequence. A dominant MF distribution of the HB array is created on the outer surface of the arc shape in the A-type round layout model and at the inner surface of the U-type arrangement. The 3D-CAD model of A-type curved HB arrays using cylindrical PMs is shown in Figure 11 (Suzuki et al., 2017).

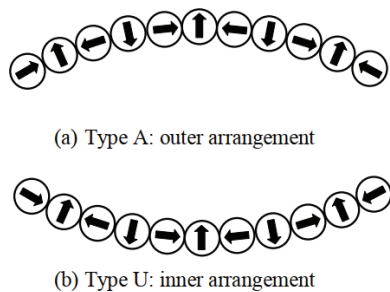


Figure 10. Diagram of curved array HB arrays using permanent cylindrical magnets (Suzuki et al., 2017).

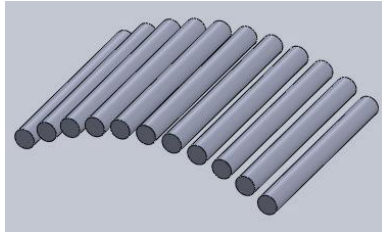


Figure 11. 3D-CAD model of A-type curved HB arrays using cylindrical PMs (Suzuki *et al.*, 2017).

Figure 12 shows the result of the line scan of the magnetic flux density in the array shown in Figure 10 (a) and Figure 11 with a quasi-static measurement. This result shows that the proposed round HB array has a magnetic flux density distribution similar to the HB array along the curved surface of the real prototype model. Figure 13 shows the magnetic flux density distribution depending on the synchronous rotation of all PMs with MF simulation. It clearly shows the shear performance of the MF on the proposed rounded HB array. With this design, the variation in the magnetic flux density distribution can be observed through the continuous rotation of the cylindrical PMs.

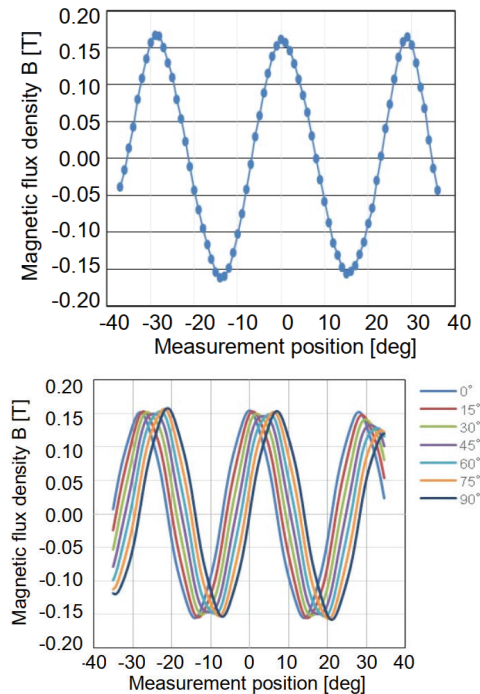


Figure 13. Simulation of the magnetic flux density distribution on a curved placed HB array. (Suzuki *et al.*, 2017).

3. CONCLUSION

There are applications of HB sequences in a wide variety of fields such as electromagnetic vibration energy harvesters using the HB array magnetic rotor (Zheng et al., 2021), the “maglev” system or magnetically levitating trains (Jiang et al., 2021), developed by Nasa, advanced HB arrays (D. Zhu et al., 2013), concentric HB cylinder magnetic refrigerator design (Tura & Rowe, 2014), linear HB array and moving magnet synchronous surface motor design (Hao et al., 2011), HB array linear alternator for thermo-acoustic motor (Saha et al., 2012). In addition, applications of HB arrays are seen in other fields of study such as physics, aerospace engineering (Shute et al., 2000), medicine (Whitney et al., 2005).

Compared to conventional PM arrays, HB arrays have the advantage of having a stronger MF locally. With a lower production and operating cost, HB arrays offer many advantages over electromagnets. Due to these advantages, static MF sources in many applications can be replaced with HB arrays.

With the geometric and parametric changes made in HB array designs different MF patterns can be created such as weak MF, strong MF, variable MF, MF free zone etc. in certain regions according to the application need.

REFERENCES

- Gieras, J. F., Wang, R.-J., & Kamper, M. J. (2008). *Axial Flux Permanent Magnet Brushless Machines*. Springer Netherlands. <https://doi.org/10.1007/978-1-4020-8227-6>
- Halbach, K. (1980). Design of permanent multipole magnets with oriented rare earth cobalt material. *Nuclear Instruments and Methods*, 169(1), 1–10. [https://doi.org/10.1016/0029-554X\(80\)90094-4](https://doi.org/10.1016/0029-554X(80)90094-4)
- Hao, X., Xing, P., & Bai, L. (2011). Design and analysis of moving magnet synchronous surface motor with linear halbach array. *Procedia Engineering*, 16, 108–118. <https://doi.org/10.1016/j.proeng.2011.08.1059>
- Hilton, J. E., & McMurry, S. M. (2012). An adjustable linear Halbach array. *Journal of Magnetism and Magnetic Materials*, 324(13), 2051–2056. <https://doi.org/10.1016/j.jmmm.2012.02.014>
- Jae-Seok Choi, & Jeonghoon Yoo. (2008). Design of a Halbach Magnet Array Based on Optimization Techniques. *IEEE Transactions on Magnetics*, 44(10), 2361–2366. <https://doi.org/10.1109/TMAG.2008.2001482>
- Jiang, Y., Deng, Y., Zhu, P., Yang, M., & Zhou, F. (2021). Optimization on Size of Halbach Array Permanent Magnets for Magnetic Levitation System for Permanent Magnet Maglev Train. *IEEE Access*, 9, 44989–45000. <https://doi.org/10.1109/ACCESS.2021.3058124>
- Jing, H., Wang, J., Wang, S., Wang, L., Liu, L., Zheng, J., Deng, Z., Ma, G., Zhang, Y., & Li, J. (2007). A two-pole Halbach permanent magnet guideway for high temperature superconducting Maglev vehicle. *Physica C: Superconductivity and Its Applications*, 463–465, 426–430. <https://doi.org/10.1016/j.physc.2007.05.030>
- Kim, W., & Trumper, D. L. (1998). High-precision magnetic levitation stage for photolithography. *Precision Engineering*, 22(2), 66–77. [https://doi.org/10.1016/S0141-6359\(98\)00009-9](https://doi.org/10.1016/S0141-6359(98)00009-9)
- Klein, Y. P., Abelman, L., & Gardeniers, J. G. E. (2021). Influence of the distribution of the properties of permanent magnets on the field homogeneity of magnet assemblies for mobile NMR. *IEEE Transactions on Magnetics*, 1–1. <https://doi.org/10.1109/TMAG.2021.3077301>
- Kratz, R., & Post, R. F. (2002). A null-current electro-dynamic levitation system. *IEEE Transactions on Applied Superconductivity*, 12(1), 930–932. <https://doi.org/10.1109/TASC.2002.1018551>
- Mallinson, J. (1973). One-sided fluxes -- A magnetic curiosity? *IEEE Transactions on Magnetics*, 9(4), 678–682. <https://doi.org/10.1109/TMAG.1973.1067714>
- Praveen, R. P., Ravichandran, M. H., Achari, V. T. S., Raj, V. P. J., Madhu, G., & Bindu, G. R. (2012). A Novel Slotless Halbach-Array Permanent-Magnet Brushless DC Motor for Spacecraft Applications. *IEEE Transactions*

- on *Industrial Electronics*, 59(9), 3553–3560. <https://doi.org/10.1109/TIE.2011.2161058>
- Saha, C. R., Riley, P. H., Paul, J., Yu, Z., Jaworski, A. J., & Johnson, C. M. (2012). Halbach array linear alternator for thermo-acoustic engine. *Sensors and Actuators A: Physical*, 178, 179–187. <https://doi.org/10.1016/j.sna.2012.01.042>
- Sarwar, A., Nemirovski, A., & Shapiro, B. (2012). Optimal Halbach permanent magnet designs for maximally pulling and pushing nanoparticles. *Journal of Magnetism and Magnetic Materials*, 324(5), 742–754. <https://doi.org/10.1016/j.jmmm.2011.09.008>
- Shute, H. A., Mallinson, J. C., Wilton, D. T., & Mapps, D. J. (2000). One-sided fluxes in planar, cylindrical, and spherical magnetized structures. *IEEE Transactions on Magnetics*, 36(2), 440–451. <https://doi.org/10.1109/20.825805>
- Suzuki, H., Sato, M., Hanafi, A. I. M., Itoi, Y., Suzuki, S., & Ito, A. (2017). Magnetic field performance of round layout linear Halbach array using cylinder-shaped permanent magnets. *2017 11th International Symposium on Linear Drives for Industry Applications (LDIA)*, 1–2. <https://doi.org/10.23919/LDIA.2017.8097248>
- Trumper, D. L., Williams, M. E., & Nguyen, T. H. (n.d.). Magnet arrays for synchronous machines. *Conference Record of the 1993 IEEE Industry Applications Conference Twenty-Eighth IAS Annual Meeting*, 9–18. <https://doi.org/10.1109/IAS.1993.298897>
- Tura, A., & Rowe, A. (2014). Concentric Halbach cylinder magnetic refrigerator cost optimization. *International Journal of Refrigeration*, 37, 106–116. <https://doi.org/10.1016/j.ijrefrig.2013.09.005>
- Whitney, R., Douglas, D., & Neil, G. (2005). *Airborne megawatt class free-electron laser for defense and security* (G. L. Wood (ed.); p. 109). <https://doi.org/10.1117/12.603906>
- Winter, O., Kral, C., & Schmidt, E. (2012). Augmented Temperature Degrading Effect of Rare Earth Magnets Arranged in Segmented Halbach Arrays. *IEEE Transactions on Magnetics*, 48(11), 3335–3338. <https://doi.org/10.1109/TMAG.2012.2199850>
- Žezulka, V., Pištora, J., Lesňák, M., Straka, P., Ciprian, D., & Foukal, J. (2013). Intensity distribution of strong magnetic fields created by opposing linear Halbach assemblies of permanent magnets. *Journal of Magnetism and Magnetic Materials*, 345, 7–12. <https://doi.org/10.1016/j.jmmm.2013.05.047>
- Zheng, Y., Wu, L., Zhu, J., Fang, Y., & Qiu, L. (2021). Analysis of Dual-Armature Flux Reversal Permanent Magnet Machines with Halbach Array Magnets. *IEEE Transactions on Energy Conversion*, 1–1. <https://doi.org/10.1109/TEC.2021.3070039>

- Zhu, D., Beeby, S., Tudor, J., & Harris, N. (2013). Increasing output power of electromagnetic vibration energy harvesters using improved Halbach arrays. *Sensors and Actuators A: Physical*, 203, 11–19. <https://doi.org/10.1016/j.sna.2013.08.008>
- Zhu, Z. Q., & Howe, D. (2001). Halbach permanent magnet machines and applications: a review. *IEEE Proceedings - Electric Power Applications*, 148(4), 299. <https://doi.org/10.1049/ip-epa:20010479>

Chapter 13

HEALTH RISKS ENCOUNTERED OF SPACECRAFTS AND SPACE PEOPLE AND PROTECTION METHODS

Mukadder İĞDİ ŞEN¹

¹ Mukadder İĞDİ ŞEN, Dr. Öğr. Üyesi, Trakya University, ORCID-ID: 0000-0002-0760-1752

1. INTRODUCTION

While the earth moves on its orbit around the Sun, the star of the Milky Way Galaxy, it is exposed to various effects in an environment called space air. People and materials in a manned or unmanned spacecraft moving in its orbit around the Earth adversely affect from this radiation. With the altitude of the spacecraft, gravity decreases and may cause problems in the normal functioning of the body. Since the spacemen are far from their daily lives on Earth, their biological order may change and their immune systems may weaken. In order to understand space radiation better, first of all, it is necessary to touch the radiation on its main source of space radiation.

1.1. Radiation

According to the Oxford Physics Dictionary, radiation is the propagation of energy in the form of electromagnetic waves, moving subatomic particles or high-energy particles that cause ionization (Oxford, 2021). Radiation is emitted by gamma rays, x-rays, ultraviolet, visible light, infrared, microwaves and radio waves at different wavelengths of the electromagnetic spectrum shown in Figure 1. Some types of radiation are alpha (α), beta (β), gamma, neutron radiation and gravitational radiation (Wikipedia1, 2021).

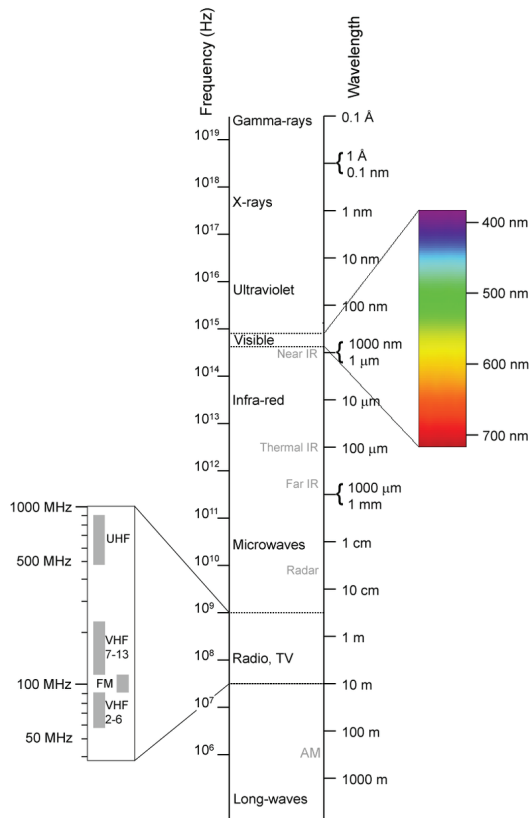


Figure 1. Electromagnetic-Spectrum (Wikipedia1, 2021).

According to the energy of the particles, there are two types of radiation, ionizing and non-ionizing (Wikipedia1, 2021). In ionizing radiation, high-energy particles such as gamma rays, x-rays and ultraviolet radiation separate electrons from the atom or molecule, thus the atom or molecule are ionized (Wikipedia2, 2021). In non-ionizing radiation, since the kinetic energy of particles (photons) which have visible light, infrared and microwave radiation in a longer wavelength than UV is very small, the particle can not break the bonds while passing through the matter and can not produce charged ions. With only its low energy, it changes the rotation and vibration of atoms and molecules.

Neutrons are classified according to their energy. High-speed neutrons can ionize atoms directly. Alpha radiation interacts strongly with matter and travels a few centimeters in the space at its normal velocities or penetrates low-density material a few millimeters (eg thin mica material). Beta radiation, which is more energetic than alpha radiation, is more penetrating than alpha, but less penetrating than gamma radiation (See Figure 2) (Wikipedia1, 2021).

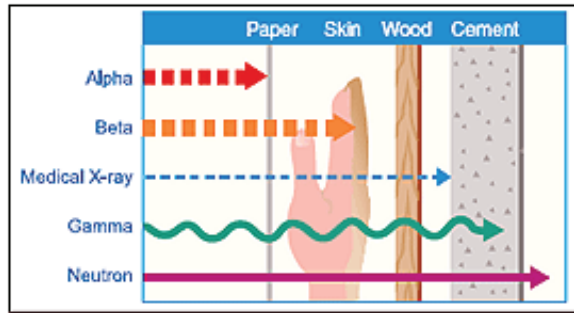


Figure 2. Particle radiation with respect to the material (Wikipedia1, 2021).

1.2. Space Radiation

Space radiation, which includes x-rays, gamma rays, proton and electron currents, is caused by cosmic and galactic rays from the sun and deep space. The main source of cosmic solar rays is the ejection of matter to the environment of the sun due to explosions on the surface of the sun (Reeves et al., 2019). Galactic cosmic rays are caused by supernova remnants and gamma ray bursts (Wikipedia1, 2021).

2. MATERIAL AND METHOD

For a manned or unmanned spacecraft, risks caused by space radiation or not caused by space radiation and the solution methods for these risks are examined under these two main headings.

2.1. The Negative Effects of Space Radiation

A spacecraft and space people can be negatively affected from space radiation as temporary or permanent damage.

2.1.1. Risks for Space People

NASA examined atomic bomb survivors in Japan, those who were exposed to radiation for their job, and people undergoing radiotherapy treatment and evaluated degenerative tissue damage such as cataracts, circulatory diseases and digestive diseases. The long-term occurrence of degenerative tissue effects for medium and high radiation doses in individuals exposed to ionizing radiation has been investigated (Mars, 2018). According to this study by NASA, important degenerative disorders that can potentially create in those exposed to space radiation: cataracts; cerebrovascular and peripheral artery diseases and cardiomyopathy and degenerative disorders in the circulatory system; cardiovascular disease may constitute a stroke (ischemic heart disease (IHD), atherosclerosis), premature aging and its associated diseases and fibrosis; immune and endocrine system dysfunction; and central nervous system (CNS) risks, digestive diseases and respiratory problems (Patel, 2016; Mars, 2018).

High doses of radiation are a major concern for manned spaceflight. Lower radiation doses are physiologically much milder but cause symptoms that can be equally serious (Mars, 2018). A representation of the acute and chronic effects of radiation on humans is available in Figure 3.

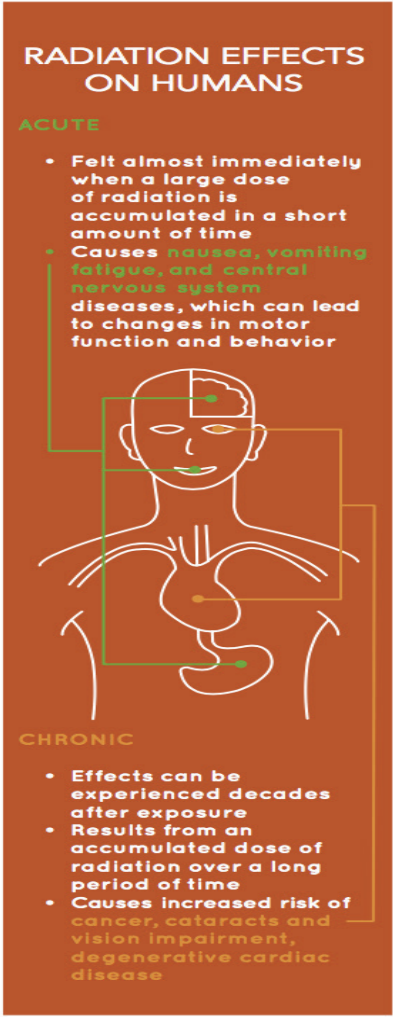


Figure 3. Radiation effects on humans (Mars, 2018).

It has been stated that degenerative diseases will develop when exposed to 0.5 Gy or more ionizing radiation. Some degenerative tissue effects have been seen in people who have performed long-term spaceflight due to their exposure ionizing radiation from galactic cosmic rays (GCR) or solar particle events (SPEs). Cardiovascular pathologies such as atherosclerosis are seen in those exposed to gamma rays. Evidence of cancer risks is available in humans exposed to radiation at doses above 100 millisievert (mSv) (Patel et al., 2016). According to the Radiation Carcinogenesis

Risk Evidence Report, a significant increase in chromosome damage in blood lymphocytes was detected after 3 to 6 months of space missions of the crew working in the ISS and MIR (Huff et al., 2016). The prolonged tenure in space also increases the likelihood of degenerative risks in tissues associated with digestive diseases and pulmonary changes (Mars, 2018).

2.1.2. Risks for Material

High kinetic energy particles come to the material and interact with their electrons so that some of their kinetic energy is transferred to them. They lose some or all of their energy by slowing down in this process called “slowing down process (displacement)”. Thus, new bonds are formed; and abrasion (damage) may occur by deteriorating the physical and chemical properties of the material (Shen et al., 2019).

2.2. SOLUTIONS

2.2.1. Natural Protection

The magnetosphere is controlled by the magnetic field (shield) of the Earth and is the space field around the planet. The shape of the Earth’s magnetosphere is caused by the “supersonic shock wave” propagating from the Sun in the center through out of the Solar System by the intensity of solar flares. The solar wind squeezes the material emitted by the supersonic shock wave on the side of the Earth facing the sun at a distance of 6 to 10 times the Earth’s radius. This shock wave creates a “Bow Shock” between the Sun and the Earth, as in Figure 4. Most solar wind particles heat up and slow down as they move out of the galaxy in a detour around the Earth. The solar wind drags the magnetosphere on Earth’s night side up to about 1000 times the Earth’s radius. This extension of the magnetosphere is known as “Magnetotail” (Kaase, 2017).

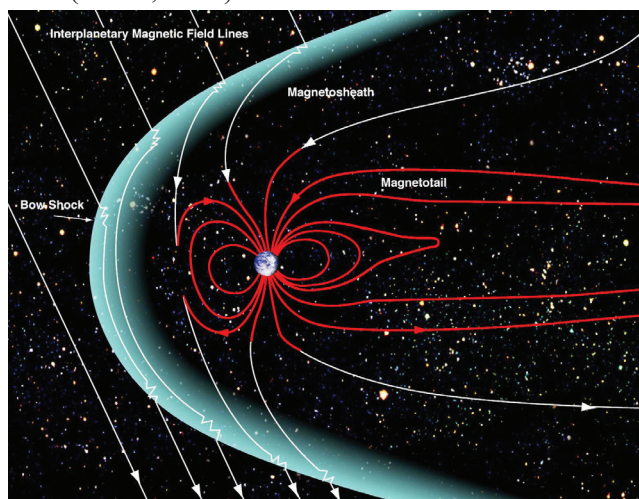


Figure 4. Earth's Magnetosphere (Kaase, 2017).

For a spacecraft and humans, Earth-centered Low Earth Orbit (LEO) (See Figure 5) with altitudes between 160-1,000 km (ESA, 2021) (or 99-651 miles) could be a natural solution to protection from space radiation. LEO has an orbital period of 128 minutes or less, usually making 11.25 orbits minimum per day, with less than 0.25 eccentricity. Most artificial satellites in space are moved in LEO. International Space Station (ISS) (look at Fig. 5) with an average altitude of 400 kilometers (250 miles) is in LEO orbit. Chinese Tiangong-1 and Tiangong-2 stations are in the orbit about 355 kilometers (221 miles) and 370 kilometers (230 miles), respectively (Wikipedia3, 2021).

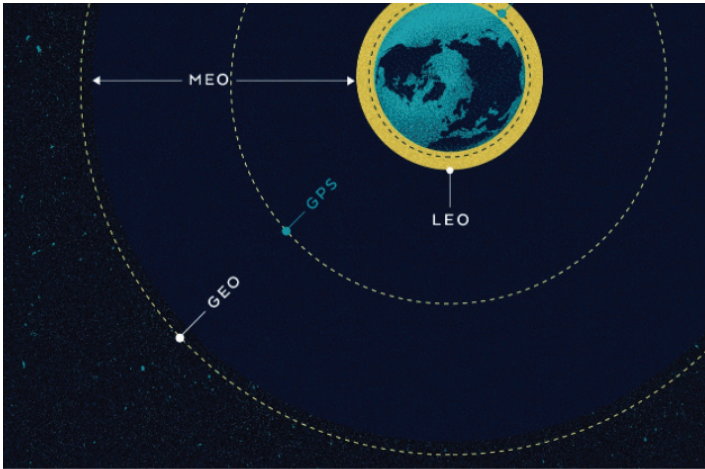


Figure 5. Orbits and ISS (Miller, 2019).

The ISS team is preserved from most of the space radiation due to its LEO orbit (Naitoa et al., 2020). However, due to the narrow field of view of the satellites on the LEO, it is a disadvantage that they can only observe a narrow part of the Earth at the same time (Wikipedia3, 2021). Since there is no natural protection of Earth's magnetosphere outside of LEO for mission success or crew health, more protection and protective mechanisms are required (Carnell et al., 2016).

2.2.2. Solutions for Space People

In order to keep the radiation exposed to the spaceflight at acceptable risk levels, the radiation generating equipment carried on the spacecraft is carefully evaluated together with the calculation and computer modeling of the radiation that the crew are exposed to while working outside and inside the spacecraft (Reeves et al., 2019). For this purpose, a radiation dosimeter, an example of which is shown in Figure 6, is used for each manned flight in accordance with NASA Radiation Health Program.

In addition, blood samples are taken to measure the damage caused by radiation to the chromosomes in the blood cells of space people returning to

Earth. NASA makes biological and behavioral researches as well as design of payloads, space habitats and life-support systems in a spacecraft. For this purpose, it applies a road map called NASA Bioastronautics (Stodieck et al., 1998). Degenerative and chronic tissue diseases and radiation damage to the central nervous system are examined for possible signs of cancer (Reeves et al., 2019).

Space humans use oral drug supplements that provide prevention and protection to reduce the damages of ionizing radiation. For prevention purposes, vitamins A and C, fish oil containing Omega-3, pectin fiber obtained from fruits and vegetables; in addition, strawberries, blueberries, cabbage and spinach are preferred for possible neurological damages. Medicines taken for protection provide faster recovery (Reeves et al., 2019). In addition, such drugs protect and repair root and progenitor cells that are capable of repairing the body and regenerating adult tissues (Be., 2006).



Figure 6. Radiation dosimetry model containing more than 300 radiation sensors used by NASA (Rask et al., 2010).

Vitamin D, which is necessary for the skeletal health of space people, is complemented as a vitamin D supplement as it can not be taken naturally due to the harmful ultraviolet radiation shield structure of the spacecraft (Reeves et al., 2019).

Works outside spacecraft should be performed in times of reduced solar activity and for shorter periods of time. It is important to continue research and development studies in order to minimize the radiation that may be exposed on flights to deep space (Reeves et al., 2019).

2.2.3. Solutions For Material

Improved materials with anti-static and anti-radiation function can protect from space radiation (Shen et al., 2019).

2.2.3.1. Radiation Shielding

Space people need to be protected from radiation depending on their location inside or outside the spacecraft, and the materials are selected accordingly.

Radiation shields are used for protection from radiation in the near and deep space and its development continues. Blocking and shielding abilities are looked at in the radiation shield (Wikipedia1, 2021; Wikipedia2, 2021). For this, stopping power and fragmentation cross section are taken into consideration (Wikipedia2, 2021). Stopping power is that the charged particle loses its energy. This depends on the type of charged particle, its energy and properties of the atoms in the material with which it comes into contact. Therefore, the stopping power for particles in the material is related to the velocity and energy of the incident particle according to the Bethe-Block formula which the heavy electron stopping formula in Quantum Classical Theory. Stopping power depends on the atomic number and density of the material being passed through (Shen, 2019).

$$(-dE/dX)_{ion} = \frac{4\pi z^2 e^4 N Z}{m_0 v^2} \left[\ln \left(\frac{2m_0 v^2}{I} \right) + \ln \left(\frac{1}{1 - \beta^2} \right) - \beta^2 - \frac{C}{Z} \right] \quad (\text{Shen et al., 2019})$$

Where, charged particle energy is E; charged particle incident depth is X; atomic density is N; electron rest mass is m_0 ; atomic number is Z; $\beta = v/c$, the electron velocity is v, the speed of light is c; the average ionization and excitation potential energy is I. Charged particles slowly lose their kinetic energy as they pass through the material and stop when they catch enough electrons. If the protective material is thick enough, the incoming particulate is blocked in the material or its energy decreases as the particle passes through the material. However, as the thickness of the radiation shield material increases, the weight of the spacecraft also increases. Secondary radiation (neutrons, protons, bremsstrahlung, etc.) produced by the collision of electrons passing through the material with the particles of the material also emits (Shen et al., 2019) (See Figure 7). Because high-energy gamma rays and galactic cosmic rays are ionized, they can pass through aluminum, which is the thin metal, but can not through cement (Reeves et al., 2019).

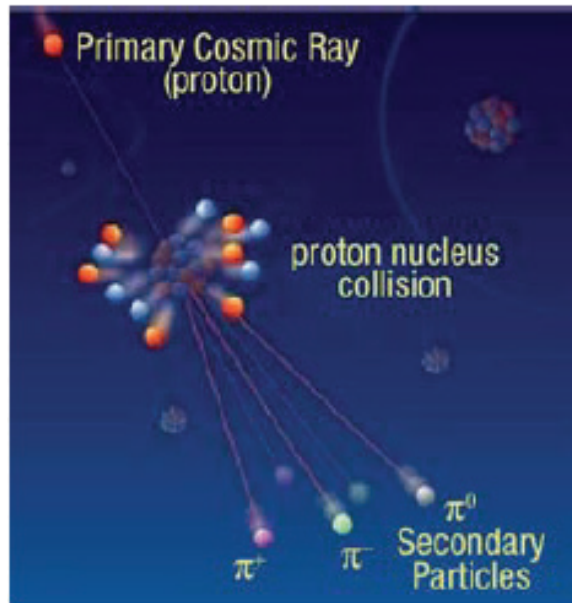


Figure 7. Damaging secondary particles can be caused by collisions between the high-energy particle and the material (Reeves et al., 2019).

Heavy elements generate more secondary radiation than lighter elements, and space puts people's health more at risk. For this reason, Spacecraft structure containing high and low atomic number materials together, especially the outer surface containing low atomic number material will increase the shielding as it will reduce the secondary radiation (Shen et al., 2019). Iron (Fe) ions easily stop in materials such as polyethylene and hydride, unlike materials such as aluminum and complex hydrides with high atomic number (Z) metals that contain little or no hydrogen (Wikipedia2, 2021).

Polyethylene plastic consisting of carbon and hydrogen atoms, called RFX1, is more efficient (50% and 15% respectively) at shielding from solar flares and galactic cosmic radiation compared to aluminum. Water, our main source of life, is a molecule that can absorb radiation. Since oxygen is the compound of water, it is heavier than polyethylene and is more expensive to launch into space. Lightweight radiation shields are easier to launch into space. A lightweight shield can significantly reduce the negative effects of space radiation particles, but cannot stop them all. If a radiation shield is 5-7 centimeters thick, it can block only 30-35 % of the radiation (Reeves et al., 2019).

2.2.3.2. Anti-static Protection Materials

During the spacecraft's operations in space, its surface may be exposed to charge and discharge effects.

Static electricity occurs when static charges accumulate beyond a threshold value and it causes to malfunction of the systems on the spacecraft (Yadav et al., 2020). Therefore, the outside of the spacecraft must be anti-static. The great space powers continue to work on the structural design of the spacecraft. NASA is investigating electrostatic and plastic protections against static electricity in this regard. Electrostatic radiation shields deflect incoming electrically charged particles with the positive and negative electric charges they produce (Reeves et al., 2019). The anti-static state on the outer surface of the spacecraft is achieved by improving the electrical conductivity of the thermal control coating, therefore the exterior of the spacecraft is usually covered with a thermo controlled coating such as PI (polyimide) (Shen et al., 2019).

2.2.3.3. Anti-Radiation Functional Materials

In the NASA study made for radiation protection material, polyethylene material used in ISS's sleeping bag was obtained. Also, an observation window as in Figure 8 is made of quartz glass with good radiation resistance (Shen et al., 2019). Polyethylene is a protector rich in hydrogen, and with its use, the exposure of space people to space radiation has been reduced in areas such as food and kitchen in the space station (Reeves et al., 2019).



Figure 8. ISS observation window (Wikipedia1, 2021).

2.2.4. Storm Shelters

Storm shelters are used for maximum protection from space radiation. Storm shelters added to a typical spacecraft can reduce the radiation effect below 0.1 Sv (Carnell et al., 2016).

2.2.5. Other Risks not Caused by Space Radiation

According to the Evidence Report on Cardiovascular Disease Risk and Other Degenerative Tissue Effects, it is necessary to mention synergistic effects for risks not caused by Space radiation together with other flight factors.

Causes of diseases not caused by space radiation can be microgravity, oxygen depletion, changes in the immune system, biological rhythms, changes in eating habits. These reasons also negatively affect the risks of cardiovascular and degenerative tissue disease indirectly caused by space radiation.

Patel et al. (2016) states that the increased duty time on the spacecraft can create major degenerative risks in digestive diseases and lung-related tissues. It has been stated that exposure to reduced gravity, even for a short time, causes disorder in the immune system. The interaction of the ionized particle with water and other cells creates reactive oxygen species (ROS), which causes indirect cell damage. The excess of free radicals produced causes oxidative damage to DNA, proteins and lipids, and also causes degenerative changes that cause cardiovascular disease, cell aging and cataracts. It can also trigger persistent metabolic changes. To protect the normal vascular system from ionizing radiation, countermeasures consisting of sulfhydryl or thiol compounds and antioxidants are used. Sulfhydryl or thiol compounds scavenge free radicals formed by ionizing radiation interacting with water. It has been reported that vitamins C and E also protect the lens and vascular system.

3. RESULTS AND CONCLUSIONS

Space radiation poses a threat for spacecraft and their crews in the orbit. In order to eliminate or reduce this threat, R & D studies of structural, operational and food measures are continuing.

The radiation shield should be studied carefully for possible primary and secondary radiation. Composite materials consisting of high and low atomic numbered elements should be preferred in order to choose the shield material and to adjust the thickness of the structure well (Shen et al., 2019). All possible risks should be taken into account in calculations for the most efficient space shield (Carnell et al., 2016). Since space radiation will be more effective in traveling to deep space (such as moon, mars), the selection of materials to be used for spacecraft and spaceflight is important (Reeves et al., 2019).

The surface of the spacecraft must be anti-static to prevent damage to both people and all devices. Space people should take drugs to reduce the effects of radiation. In addition, blood samples and radiation measurements of the crew should be made regularly. Since solar particle events (SPEs) include helium with a velocity of several hundred MeV and heavier elements, works outside spacecraft should be carried out outside these activity times. Space agencies should create sample models for all kinds of low, medium and high level radiation and continue their research studies and conservation strategies in order to prevent possible damage to materials and people on these models, because all these studies are required for near space and future deep space missions and travels.

REFERENCES

- Oxford Physics Dictionary, (2021, May 1). Radiation, Retrieved May 2 2021, from <https://languages.oup.com/google-dictionary-en/>
- Wikipedia1 (2021, April 1). Radiation, Retrieved April 20 2021, from <https://en.wikipedia.org/wiki/Radiation>
- Wikipedia2 (2021, May 1). Ionizing radiation, Retrieved May 5 2021, from https://en.wikipedia.org/wiki/Ionizing_radiation
- Reeves, K. K. et all., “Space Radiation”, 2019, NASA Human Research Program Engagement and Communications, Radiation iBook, USA.
- Mars, K. (2018, Jun 8). Space Radiation Risks, Retrieved April 20 2021, from <https://www.nasa.gov/hrp/elements/radiation/risks>
- Patel, Z. et all., “Evidence Report: Risk of Cardiovascular Disease and Other Degenerative Tissue Effects from Radiation Exposure”, 2016, National Aeronautics and Space Administration, Lyndon B. Johnson Space Center.
- Huff, J. et all., “Evidence Report: Risk of Radiation Carcinogenesis”, 2016, National Aeronautics and Space Administration, Lyndon B. Johnson Space Center.
- Shen, Z. et all., “Protection of Materials from Space Radiation Environments on Spacecraft”, 2019, IOP Conf. Series: Materials Science and Engineering, 585, doi:10.1088/1757-899X/585/1/012089.
- Kaase, A. (2017, Aug 7). Earth’s Magnetosphere, NASA, Goddard, Retrieved April 20 2021, from https://www.nasa.gov/mission_pages/sunearth/multimedia/magnetosphere.html
- ESA, (2021, March 30). Types of orbits, Retrieved April 20 2021, from https://www.esa.int/Enabling_Support/Space_Transportation/Types_of_orbits
- Wikipedia3 (2021, May 7). Low Earth orbit, Retrieved May 8 2021, from https://en.wikipedia.org/wiki/Low_Earth_orbit
- Miller, S. (2019, March 7). Low-Earth Expectations: What do LEO Satellites Mean for the IFC Landscape?, Illustration by Eduardo Leblanc, Retrieved April 20 2021, from <https://apex.aero/articles/low-earth-expectations-geostationary-satellites-finally-eclipsed/>
- Naitoa, M. et all., “Investigation of shielding material properties for effective spaceradiation Protection”, 2020, Life Sciences in Space Research 26, 69–76.
- Carnell, L. et all., “Evidence Report: Risk of Acute Radiation Syndromes due to Solar Particle Events”, 2016, National Aeronautics and Space Administration, Lyndon B. Johnson Space Center.

- Rask, J. et al., "Space Facing The Radiation Challenge", 2010, National Aeronautics and Space Administration, George C. Marshall Space Flight Center.
- Stodieck, L. S.; Hoehn, A.; Heyenga, A. G., "Space flight research leading to the development of enhanced plant products: Results from STS-94", 1998, AIP Conference Proceedings, 420: 578–585, doi:10.1063/1.54909, ISSN:0094-243X.
- Be, T., "Stem cells-a clinical update, Australian Family Physician", 2006, 35 (9), ss. 719-721. PMID 16969445.
- Yadav, R. et al., "Polymer Composite for Antistatic Application in Aerospace", 2020, Defence Technology, Volume 16, Issue 1, Pages 107-118.

Chapter 14

THERMODYNAMIC ANALYSIS OF THE REFRIGERATION TEST EVAPORATOR UNIT WITH ADVANCED EXERGY ANALYSIS

Betül SARAÇ¹

Teoman AYHAN²

1 Karadeniz Technical University, Department of Naval Architecture and Marine Engineering, Trabzon 61530, Turkey.

Orcid number: 0000-0003-3876-7314, bsarac@ktu.edu.tr

2 Avrasya University, Department of Mechanical Engineering, Trabzon 61080, Turkey

0000-0003-2917-5069. teoman.ayhan@avrasya.edu.tr

1. Introduction

Indoor air quality and thermal comfort can be realized with heating, ventilation and air conditioning (HVAC) technology. Currently, indoor air conditioning is common in several countries, especially in countries with hot and humid climates and where the summers are hot. To ensure energy efficiency, it is important to measure the performance of HVAC system components. Thus, the air conditioner manufacturers require more powerful design tools and a better understanding about the performances of the latest-technology components to remain competitive in the global market. Several air conditioner test facilities are available and operate based on the test standards published by American National Standards Institute / The American Society of Heating Refrigerating and Air Conditioning Engineers [1]. Thus, the present study aimed to validate the thermodynamic performance of for a corporate test unit for the manufactured evaporators that employ exergy and advanced exergy methods. The advantages of exergetic analyses were reported in several publications in different thermal science fields [2]. In these studies, advanced exergy methods were proposed and applied in vapor compression refrigerators and simple gas turbine power plants.

The present paper aimed to provide information on fundamental exergy terminology and explain the concept of advanced exergy analysis. In the advanced exergy method, exergy destruction is distributed to destructive parts that represent different losses. *The Unavoidable exergy destruction*, which represents the first group among these destruction parts, represents the exergy destruction of a component in the unit that could not be destroyed when the most advanced technologies are applied to the component during its employment in the unit. *The avoidable exergy destruction* represents the improvement potential of the component in the system. *The endogenous exergy destruction* component that constitutes the second group in the destruction parts represents only a part of the exergy destruction that exhibits the irreversibility of a unit component, while *the exogenous exergy destruction* is described as the difference between the actual exergy destruction and the endogenous exergy destruction [3]. The exergy destructions could be categorized in two main groups in advanced exergy methodology: endogenous–exogenous exergy destruction and avoidable–unavoidable exergy destruction [3]. These exergy destruction parts could determine the parts where inefficiencies were observed due to component interactions, and those that could be avoided with technological improvements in the thermal system. The advanced exergy analysis method was adopted in a combined cycle power plant to determine which inefficiencies were caused by component interactions, and which could be avoided with technological improvements in the plant [4].

Recently, further studies were conducted on the analysis of the performance of the vapor compression refrigeration systems with entropy generation and exergy analysis methods under various operational conditions such as different time intervals and different refrigerants/refrigerant blends [5]. They tested the combination of R134a + 15% R290 and R600a for the performance of refrigeration system. In their performance analysis of the refrigerant system based on refrigerant combinations, they reported that the entropy generation and exergy destruction were negligible. It was also reported that R134a refrigerant could have high effects on global warming (1430 GWP). The employment of an alternative eco-friendly refrigerant such as R600a with zero ozone depletion and the least global warming potential instead of R134a was recommended in refrigeration systems. Also, the performance analysis of a vapor compression refrigeration system with pure hydrocarbon (HC) refrigerants was theoretically investigated in four pure HCs; propane (R290), butane (R600), isobutane (R600a), isopentane (R1270) by [6]. Furthermore, R22 and R134a refrigerants were also investigated in the study. The findings demonstrated that the cooling performance coefficient variations in these refrigeration systems were quite small. It was reported that the energetic and exergetic efficiencies of the system were higher with R1270 and R600 when compared to R600a and R290. Detailed exergy analysis of a two-stage vapor compression cycle was conducted and exergy destruction and losses in its components were calculated [7]. A simple model was developed, and local state equations were used to calculate refrigerant thermodynamic properties. The exergy analysis findings were determined for the two-stage refrigeration system operating between a constant evaporation temperature of -30°C and various condensation temperatures of 30, 40, 50, and 60°C . The two natural substitutes of HCFC22, namely, propane (R290) and ammonia (R717) were used as operational fluids. The authors reported that the most significant exergy destruction was observed in the compressors, expansion valves and the condenser. An advanced exergy analysis of an ejector expansion trans-critical CO_2 refrigerating system was reported [8]. They reported exergy destruction for each component in the compressor ejector, evaporator and gas cooler line, respectively. Also, it was stated that the total exergy destruction type was internal. They reported that 43.44% of the total exergy destruction could be improved by improving the system components. It was demonstrated that when the component efficiency is increased, the avoidable endogenous exergy destruction rate could be reduced. In another study, the applications of the advanced exergy method were reported in the food industry [9]. The method was adopted in the analyses conducted in a milk processing facility, a significant energy consumer in the food industry. It was demonstrated that particularly the avoidable and unavoidable exergy destruction could contribute to a better understanding of the real processes and how to target

process optimization. A detailed explanation of the application of the advanced exergy analysis method in cooling systems was described in another study [10]. The highest potential cooling system performance was calculated with the advanced exergy analysis method. The performance improvement was achieved for the entire cooling system with the elimination of the irreversibility observed in the evaporator,. Another study to determine exergy destruction parts was conducted on a gas turbine with the advanced exergy method [11]. In the study, it was determined that the combustion chamber should be improved. It was calculated that 93.55% of the system exhibited unavoidable exergy destruction and the improvement potential was low for the system. Endogenous exergy destruction was determined as 81.33% and the interaction between the components was weak based on this value. To investigate the types of exergy destruction in the system and system components, the thermodynamic model of a military turbojet engine was selected to apply the advanced exergy method [12]. Performance improvements were implemented in the low-pressure compressor, combustion chamber, and reaction nozzle to improve the whole system performance [13] and exergy was analyzed in a natural gas liquefaction and production facility and the economic impacts of exergy destruction was determined in the system. In the study, it was reported that exergy destructions in the components were endogenous. Based on the economic analysis, it was estimated that the cost of the endogenous exergy was the highest. In another study, the advanced exergy method was used to analyze the performance of a supermarket refrigeration system with R744 [14]. Another study compared the exergetic efficiency of an ejector cooling system with vapor compression cooling with the advanced exergy method [15]. A combined power unit was modeled and discussed as a typical example for the advanced exergy analysis and exergy economy method practices [16]. Exergy economic efficiency method is the analysis of exergy destructions in the system based on costs. Studies reported that the system performance could be improved by 14% and the costs could be reduced by 15%. In a study, a regular air-conditioning system as the mainline and two other air-conditioning systems with liquid-vapor separation heat exchanger were compared with the advanced exergy method [17]. Another research investigated a trigeneration system with advanced exergy analysis [18]. They reported that exergy efficiency of the system was 0.354, while total exergy destruction rate in the system was 16.695 MW. The aim of their study was to determine the improvement potential of the system. In a study, a furnace in a petrochemical plant located in Turkey was analyzed with advanced exergy analysis [19]. Potential exergy improvements in system components were calculated. It was reported that there were major entropy sources in the system. The exergy destructions were determined in system components and exergy efficiencies were calculated. The advanced exergy analysis results

demonstrated that exergy efficiency could be improved up to 52.4% and 85.8%, respectively. In a study, advanced exergy method was employed in a compressed air energy storage system [20]. They investigated the exergy destruction in each system element and the thermodynamic efficiency of the system. They found that the unavoidable exergy destruction in the system components was higher than the avoidable destruction and the most important components were combustion chambers, intercoolers, and after coolers based on avoidable exergy destruction. Exergy destruction could be significantly reduced with the improvement of the main component efficiencies. More than half of the avoidable exergy destruction is exogenous, indicating that the interactions between the components have a significant impact on system performance. A mathematical model was developed to calculate endogenous and exogenous exergy destructions in thermal systems. The model was applied on a simple gas-turbine power system [21]. Another study on advanced exergy analysis was conducted with an air compression energy storage system [22]. The system included a compressed air tank, multi-stage compressors, intercoolers, and a gas-turbine power unit. The avoidable exergy damage induced by inter-component interaction was significantly exogenous. A study was conducted on the optimization of the performance of a parallel compression supermarket refrigerator with advanced exergy analysis method [23]. The study reported that the condenser, high-pressure compressor, and low-pressure compressors exhibited the highest improvement with the advanced exergy method. The above-mentioned novel method developed to determine the performance of a thermal system included advanced exergy analysis; however, it was only adapted to a few thermal energy systems. The performance analysis was conducted on a refrigeration system in a cargo vessel with both conventional and advanced exergy analyses methods [24, 25]. They found that, As the point temperature differences increase, the difference between the exergetic efficiency of real and unavoidable systems increases. A typical application of advanced exergy analysis could be observed in another paper [26]. The exergy destructions in the system were calculated and presented in graphs [26]. It was determined that the system performance could be enhanced with improvements in the ejector, the condenser, and the generator. A cascade absorption refrigeration system, which utilizes low-grade waste heat, was studied in another study [27]. They employed advanced exergy analysis and exergo-economic analysis in the study. The findings were compared with those obtained with the conventional method. Advanced exergy analysis was conducted on a ground-source heat pump drying system in dry foods industry [28]. The performance of whole system and each component was analyzed. It was reported that the most important system component was the condenser based on the findings.

The present paper aimed to contribute to the literature by conducting advanced exergy analysis on an evaporator test unit. The methodology was

adapted from previous studies [2, 21]. The main aim of the present paper could be summarized as follows:

- The analysis of the performance of the evaporator test unit.
- Exergetic analysis of the performance of each component in the test unit.
- The determination of exergy destruction in the evaporator test unit components of the as endogenous or exogenous and avoidable or unavoidable.
- The clarification of the mutual interdependence between each evaporator test unit component.
- The determination of the best thermodynamical component that was not affected by irreversibility generated by the other components.

2. System Description

The evaporator test unit was employed in an evaporator manufacturing company.

2.1 General description of the test unit

The evaporator test unit included a calibrated room calorimeter with good insulation, a test room, and a refrigeration system. A simplified diagram of the evaporator test unit and the refrigeration cycle is presented in Figure 1. Test facilities allowed for refrigerant-side pressure and temperature measurements at the inlet and outlet of each refrigeration loop component. Also, air-side temperature, humidity, and atmospheric pressure were measured. The test facility could provide a variety of indoor and outdoor rooms. The test chamber was cooled by a vapor refrigeration system. The compressor, the condenser and the throttling valve were located outside of the calorimeter calibrated room. The pipelines were well insulated throughout the cycle. The temperature measurements, control systems, test room and and calibrated room air pressure measurements were provided by Friterm Corporation. The temperature and the pressure sensors were excluded in the figure for simplicity purposes.

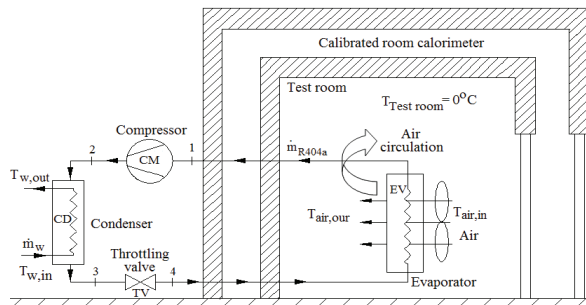


Figure 1. The evaporator test unit and calibrated room calorimeter diagram.

The measured value within the accepted error limits provide significant accuracy in the determination of refrigerant and air properties, and also valuable information about the effects of the inclusion of the test evaporator in the refrigerating loop on performance. All test unit data were collected with data acquisition and computer systems.

2.2 Assumptions

The energy, the exergy, and the advanced exergy analysis presented in this study were based on the following assumptions.

✓ The heat absorbed or released on the outer surface of the refrigeration piping system is neglected.

✓ The refrigerant evaporation and condensation temperatures were constant; however, the pressure drop in the evaporator was 1% of the evaporation and condensation pressures.

✓ The test system was operated under steady-state conditions.

✓ Changes in kinetic and potential energy were neglected.

✓ The air was accepted as a perfect gas.

✓ The compressor was accepted as non-adiabatic.

✓ The fan effect was neglected.

✓ The temperatures of real, unavoidable, theoretical and hybrid cycle states and also pinch point temperature differences in the condenser and the evaporator were accepted as constant, while the mass flow rate for the refrigerant R404a, the cooling water in the condenser and the processed air in the evaporator were accepted as variable.

2.3 Operation mode

The temperature and humidity could be independently controlled in the test room; however, they are somewhat correlated with the air in the calibrated room calorimeter. Due to the system control strategy, the thermal requirements of the test room and calibrated calorimeter room were met. The measurements were started after the control unit in the test room and calibrated calorimeter room were set to reach the desired conditions in both rooms. The data were collected when the setup stabilized, steady-state conditions and stable operation were maintained. The cold-water flow rate was based on full condenser capacity during the tests. Three tests were conducted at different test room air temperatures. The data measurements and exergy of the refrigeration loop states are presented in Table 1.

Table 1. Experimental data provided by the Friterm Company

	Test room air temperature [-18°C]					Test room air temperature [0°C]					Test room air temperature [10°C]				
Com	Fluid	\dot{m} [kg/s]	T [K]	P [kPa]	e [kJ/kg]	\dot{m} [kg/s]	T [°K]	P [kPa]	e [kJ/kg]	\dot{m} [kg/s]	T [K]	P [kPa]	e [kJ/kg]		
1	R404a	0.05	284	250	21.59	0.07	304	467	36.23	0.061	308	596	41.85		
2	R404a	0.05	347	1285	62.13	0.07	359	1786	70.42	0.061	352	1706	68.11		
3	R404a	0.05	283	1285	51.10	0.07	303	1786	52.07	0.061	303	1706	52		
4	R404a	0.05	24764	250	46.35	0.05	264	467	48.51	0.061	272	596	48.39		
$T_{w,in}$	Water	1	288	151	0.049	0.30	288	190	0.088	0.31	289	190	0.096		
$T_{w,out}$	Water	1	291	111	0.074	0.30	299	101	0.856	0.31	299	101	0.709		
$T_{air,in}$	Air	4.57	255	101	2.621	0.05	273	101	0.766	0.029	283	101	0.161		
$T_{air,out}$	Air	4.57	253	101	2.897	0.05	268	101	1.008	0.029	277	101	0.323		

3. Methodology

3.1 Exergy analysis

The sources of irreversibility and location in the thermal system and their magnitude occurred in each component can be calculated using the exergy analysis method, which is a general method for detecting the source of irreversibilities, and their magnitudes. The exergy balance equation is applied to each component separately in the system to determine the location and magnitude of exergy destruction in each unit. By applying the exergy equation to the system elements participating in the thermodynamic model considered, exergy input and exergy out for each element were calculated by the following relation.

$$e = h - h_0 - T_0(s - s_0) \quad (1)$$

The total fluid exergy in the fluid flows considered was calculated by equation 2, and the exergy destruction occurring in each element was calculated by equation 3 from the exergy equation.

$$\dot{E} = \dot{m}e \quad (2)$$

$$\dot{E}_D = \sum_k \left(1 - \frac{T_0}{T_k}\right) \dot{Q}_k - \dot{W} + \sum_k \dot{E}_{k,in} - \sum_k \dot{E}_{k,out} \quad (3)$$

Thermal and mechanical exergy definitions of fluid during the throttle of the expansion valve are determined with the Equations 4 and 5 [29].

Thermal exergy

$$e^{\Delta T} = [h_{(T,P)} - h_{(T_0,P)} - T_0(s_{(T,P)} - s_{(T_0,P)})]_{P=c} \quad (4)$$

Mechanical exergy

$$e^{\Delta P} = [h_{(T_0,P)} - h_{(T_0,P)} - T_0(s_{(T_0,P)} - s_{(T_0,P)})]_{T=c} \quad (5)$$

The pressure at the inlet and outlet of the thermal expansion valve was used to calculate the thermal exergy with Equation 4. In the constant temperature process, for the mechanical exergy value given in Equation 5, the dead temperature value was taken. The exergy efficiency equation for the thermal expansion valve was calculated with the Equation 6 based on the ratio of exergy product to exergy fuel [29].

$$\varepsilon_{TV} = \frac{(\dot{E}_4 - \dot{E}_3)_T}{(\dot{E}_3 - \dot{E}_4)_M} \quad (6)$$

The energy and exergy equations applied to the system components in the real and the theoretical models are summarized in Table 2. Since the compression in the compressor includes both internal and external irreversibility, the heat discharged from the compressor was included in the calculations.

The exergy destruction and exergy efficiency equations in the advanced exergy method based on the exergy fuel and exergy products are presented in Table 3.

Table 2. Energy, exergy, and exergetic efficiency equations

Comp onent	Energy equation	Exergy equation
CM	$\dot{W}_{CM} = \dot{m}_1(h_2 - h_1) + \dot{Q}_{CM}$	$\dot{E}_{D,CM} = \dot{W}_{CM} - (\dot{E}_2 - \dot{E}_1) + \dot{E}_{Q,CM}$
EV	$\dot{m}_{air}(h_{air,in} - h_{air,out}) = \dot{m}_R(h_1 - h_4)$	$\dot{E}_{D,EV} = (\dot{E}_4 - \dot{E}_1) - (\dot{E}_{air,out} - \dot{E}_{air,in})$
CD	$\dot{m}_w(h_{w,in} - h_{w,out}) + \dot{Q}_{CD} = \dot{m}_R(h_2 - h)$	$\dot{E}_{D,CD} = (\dot{E}_2 - \dot{E}_3) - (\dot{E}_{w,out} - \dot{E}_{w,in}) + \dot{E}_{Q,CD}$
TV	$\dot{m}_R h_3 = \dot{m}_R h_4$	$\dot{E}_{D,TV} = \dot{E}_3 - \dot{E}_4$
$\dot{E}_{Q,CD} = \dot{Q}_{CD}(1 - \frac{T_0}{T_{s,CD}}), \quad \dot{E}_{Q,CM} = \dot{Q}_{CM}(1 - \frac{T_0}{T_{s,CM}})$		

Table 3. Exergy fuel and exergy product definitions for exergy destruction and exergy efficiency calculations

Com.	\dot{E}_F	\dot{E}_P	\dot{E}_D	Exergy efficiency
CM	\dot{W}_{CM}	$\dot{E}_2 - \dot{E}_1$	$\dot{W}_{CM} - (\dot{E}_2 - \dot{E}_1) + \dot{E}_{Q,CM}$	$\varepsilon_{CM} = \frac{\dot{E}_2 - \dot{E}_1}{\dot{W}_{CM}}$
EV	$\dot{E}_4 - \dot{E}_1$	$\dot{E}_{air,out} - \dot{E}_{air,in}$	$(\dot{E}_4 - \dot{E}_1) - (\dot{E}_{air,out} - \dot{E}_{air,in})$	$\varepsilon_{EV} = \frac{\dot{E}_{air,in} - \dot{E}_{air,out}}{\dot{E}_4 - \dot{E}_1}$
CD	$\dot{E}_2 - \dot{E}_3$	$\dot{E}_{w,out} - \dot{E}_{w,in}$	$(\dot{E}_2 - \dot{E}_3) - (\dot{E}_{w,out} - \dot{E}_{w,in}) + \dot{E}_{Q,CD}$	$\varepsilon_{CD} = \frac{\dot{E}_{w,in} - \dot{E}_{w,out}}{\dot{E}_2 - \dot{E}_3}$
TV	$(\dot{E}_3 - \dot{E}_4)_M$	$(\dot{E}_4 - \dot{E}_3)_T$	$(\dot{E}_3 - \dot{E}_4)_M - (\dot{E}_4 - \dot{E}_3)_T$	$\varepsilon_{TV} = \frac{(\dot{E}_4 - \dot{E}_3)_T}{(\dot{E}_3 - \dot{E}_4)_M}$
Tot	\dot{W}_{CM}	$\dot{E}_{air,out} - \dot{E}_{air,in}$	$\dot{E}_{D,CM} + \dot{E}_{D,CD} + \dot{E}_{D,TV} + \dot{E}_{D,EV}$	$\varepsilon_{Tot} = \frac{\dot{E}_{air,out} - \dot{E}_{air,in}}{\dot{W}_{CM}}$

3.2 Advanced exergy analysis

In the definition of the thermodynamic open system, the energy input from the material and the types of energy that enter the system boundary as work and heat are generally defined as the exergy fuel. Based on the same idea, the energy released by the mass flow system in the open system and the types of the energy that are transferred from the system boundary as work and heat are generally defined as exergy products [3, 11, 23]. Exergy fuel-product analysis allows the determination of how the performance of process components usually affects the system performance, how to improve cycle performance, and which components or system components were improved [2, 8, 12, 13, 21]. In the k^{th} system component, the exergy of the input energy is defined as $\dot{E}_{F,k}$ exergy fuel. Similarly, in the "k" system component, the exergy of the output energy is defined as $\dot{E}_{P,k}$ exergy product. Generally, the exergy fuel-product analysis describes the employment of the exergy in the exergy source and the consequent exergy production. In this process, the exergy wasted in the environment and not reutilized is defined as exergy loss and it is indicated by \dot{E}_L symbol. The total exergy fuel-product, total exergy product, total exergy destruction $\sum_{n=1}^n \dot{E}_{D,k_n}$ and total exergy loss in the cycle could be written mathematically as follows based on the balance of exergy.

$$\dot{E}_{F,tot} = \dot{E}_{P,tot} + \sum_{n=1}^n \dot{E}_{D,k} + \dot{E}_{K,tot} \quad (7)$$

In exergy analysis, two indicators are employed to examine the cycle components and the cycle itself (the whole system). First, the exergy efficiency of the system components is indicated by “ ε ” ve and defined as the ratio of exergy product to exergy fuel. The second indicator is the ratio of the exergy destruction in the k^{th} unit in the cycle to the exergy fuel in the whole system and indicated by the “ y ”. In the above mentioned definitions, the two indicators:, the exergetic efficiency ε , and the exergy destruction ratio y , could be written for each system element in for the whole system.

$$\varepsilon_k = \frac{\dot{E}_{P,k}}{\dot{E}_{F,k}} \text{ for the } k^{\text{th}} \text{ component} \quad (8)$$

$$\varepsilon_{top} = \frac{\dot{E}_{P,tot}}{\dot{E}_{F,tot}} \text{ for the cycle} \quad (9)$$

$$y_k = \frac{\dot{E}_{D,k}}{\dot{E}_{F,k}} \text{ for the } k^{\text{th}} \text{ component} \quad (10)$$

$$y_{top} = \frac{\dot{E}_{D,tot}}{\dot{E}_{F,tot}} \text{ for the cycle} \quad (11)$$

3.3 Exergy destruction types

Advanced exergy analysis approaches exergy destruction in two sections to better investigate unit ineffectiveness. Real exergy destruction is scrutinized in two main classes. The first parts section includes endogenous exergy destruction ($\dot{E}_{D,k}^{EN}$) and exogenous exergy destruction ($\dot{E}_{D,k}^{EX}$), the section includes avoidable exergy destruction ($\dot{E}_{D,k}^{AV}$) and unavoidable exergy destruction ($\dot{E}_{D,k}^{UN}$).

$$\dot{E}_{D,k} = \dot{E}_{D,k}^{EN} + \dot{E}_{D,k}^{EX} \quad (12)$$

$$\dot{E}_{D,k} = \dot{E}_{D,k}^{AV} + \dot{E}_{D,k}^{UN} \quad (13)$$

Descriptions of these exergy destruction parts that are calculated for the k^{th} system component are explained below.

Endogenous exergy destruction; $\dot{E}_{D,k}^{EN}$

Endogenous exergy destruction $\dot{E}_{D,k}^{EN}$ indicates the irreversibility of the k^{th} system component. There is no interaction between $\dot{E}_{D,k}^{EN}$ and the irreversibility of other cycle components. The endogenous exergy destruction section for the k^{th} component, was calculated with the hybrid-cycle.

Exogenous exergy destruction; $\dot{E}_{D,k}^{EX}$

The exogenous exergy destruction $\dot{E}_{D,k}^{EX}$ is the difference between the real exergy destruction and the endogenous exergy destruction ($\dot{E}_{D,k}^{EX} = \dot{E}_{D,k} - \dot{E}_{D,k}^{EN}$). It is the exergy destruction that occurs in the k^{th} component due to the irreversibility induced by the other components except the k^{th} system component.

Unavoidable exergy destruction; $\dot{E}_{D,k}^{UN}$

The unavoidable exergy destruction $\dot{E}_{D,k}^{UN}$, is an indestructible exergy destruction in the k^{th} component produced by the latest technology. The irreversibility of the component is due to technical limitations. The unavoidable exergy destruction in the k^{th} component, is calculated based on the unavoidable-cycle.

Avoidable exergy destruction; $\dot{E}_{D,k}^{AV}$

The difference between true exergy destruction is defined as ($\dot{E}_{D,k}^{AV} = \dot{E}_{D,k} - \dot{E}_{D,k}^{UN}$) that the differences between real and unavoidable exergy destruction can be developed for the k^{th} component in the system. The development potential of the k^{th} component is judged by avoidable exergy destruction. Thus, the avoidable exergy destruction should be prioritized. To obtain more detailed information about the behavior of exergy destruction

types, they could be combined and reorganized to observe the interactions between them using logical combinations [15].

Unavoidable-Endogenous exergy destruction ($\dot{E}_{D,k}^{UN,EN}$):

$\dot{E}_{D,k}^{UN,EN}$ can-not be reduced due to technical limitations in component k^{th} .

Unavoidable-Exogenous exergy destruction ($\dot{E}_{D,k}^{UN,EX}$):

$\dot{E}_{D,k}^{UN,EX}$ parts of the exergy destruction shows that, the technical limitations of the remaining system components can-not be eliminated.

Avoidable-Endogenous exergy destruction ($\dot{E}_{D,k}^{AV,EN}$):

Avoidable-endogenous exergy destruction $\dot{E}_{D,k}^{AV,EN}$ can be eliminated by increasing the efficiency of the k^{th} component.

Avoidable-Exogenous exergy destruction ($\dot{E}_{D,k}^{AV,EX}$):

$\dot{E}_{D,k}^{AV,EX}$ can be reduced by a structural improvement of the overall system or the efficiency of the remaining system components.

Thus, the exergy destruction in the k^{th} component could alternatively be as follows:

$$\dot{E}_{D,k} = \dot{E}_{D,k}^{UN,EN} + \dot{E}_{D,k}^{UN,EX} + \dot{E}_{D,k}^{AV,EN} + \dot{E}_{D,k}^{AV,EX} \quad (14)$$

The expressions in this equation are calculated as follows [12, 15, 23].

$$\dot{E}_{D,k}^{UN,EN} = \frac{\dot{E}_D^{UN} \dot{E}_D^{EN}}{\dot{E}_{D,R}} \quad (15)$$

$$\dot{E}_{D,k}^{AV,EN} = \frac{\dot{E}_D^{AV} \dot{E}_D^{EN}}{\dot{E}_{D,R}} \quad (16)$$

$$\dot{E}_{D,k}^{UN,EX} = \frac{\dot{E}_D^{UN} \dot{E}_D^{EX}}{\dot{E}_{D,R}} \quad (17)$$

$$\dot{E}_{D,k}^{AV,EX} = \frac{\dot{E}_D^{AV} \dot{E}_D^{EX}}{\dot{E}_{D,R}} \quad (18)$$

In advanced exergy analysis, it is emphasized that $\dot{E}_{D,k}^{AV,EN}$ and $\dot{E}_{D,k}^{AV,EX}$ exergy destructions should be prioritized to improve the performance of each component. In advanced exergy analysis, the combined mexogenous exergy destruction type is defined as shown below [3, 12, 15, 22, 23]:

Mexogenous exergy destruction $\dot{E}_{D,k}^{Mex}$

Mexogenous exergy destruction $\dot{E}_{D,k}^{Mex}$ is defined as the difference between the $\dot{E}_{D,k}^{EX}$ and the combined effect of the exergy destruction in all the other system components for the k^{th} component [11, 15].

$$\dot{E}_{D,k}^{Mekso} = \dot{E}_{D,k}^{EX} - \sum_{n \neq k}^n \dot{E}_{D,k}^{EX,n} \quad (19)$$

3.4 Exergetic performance parameters

Based on the first and second laws of thermodynamics and the advanced exergy analysis method, the energy and exergy destruction was calculated qualitatively and quantitatively for each component to estimate the whole system performance. The refrigeration system thermodynamic cycles in the evaporator test unit are presented in Figure 2 with a T-s diagram under the actual operation parameters and thermodynamic data. The real cycle, unavoidable cycle, and the theoretical cycle are represented by the 1R, 2R, 3R and 4R points, 1UN, 2UN, 3UN, and 4UN points and 1T, 2T, 3T, and 4T point, respectively.

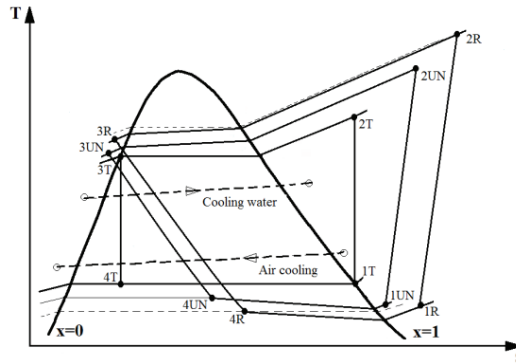


Figure 2. T-s diagram for real cycle (1R-2R-3R-4R), unavoidable cycle (UN-2UN-3UN-4UN) and Theoretic cycle (1T- 2T-3T-4T).

In the study, system performance calculation with the advanced exergy analysis method, the minimum temperature difference of the fluid flow in the condenser and the evaporator was accepted as typical operating parameters for the thermodynamic model. Data obtained with actual measurements and the thermodynamic simulation model are presented in Table 4.

Table 4. Operating parameters for the real cycle and theoretical cycles assumptions.

Parameters	Test room air temperature [10°C]			Test room air temperature [0°C]			Test room air temperature [-18°C]		
	Conditions			Conditions			Conditions		
	Real Cycle	Un. Cycle	Theo Cycle	Real Cycle	Un. Cycle	Theo Cycle	Real Cycle	Un. Cycle	Theo Cycle
	Real Cycle	Un. Cycle	Theo Cycle	Real Cycle	Un. Cycle	Theo Cycle	Real Cycle	Un. Cycle	Theo Cycle
Pressure drop percentage $\Delta P[\%]$	1	0.5	0	1	0.5	0	1	0.5	0
Pinch temperature difference in the condenser, [°]	12.12	0.5	0	13	0.5	0	7.93	0.5	0
Pinch temperature difference in the evaporator. [°]	5.37	0.5	0	4	0.5	0	5.88	0.5	0
Compressor efficiency, $\eta_{CM} \%$	85	95	100	85	95	100	85	95	100
Condensation temperature for R404a [°C]	37.13	25.5	25	39	26.5	26	25.9	18.5	18
Evaporation temperature for R404a [°C]	-0.71	4.16	4.66	-8.18	-4.68	-4.18	-25.8	-20.5	-20
Throttling processes 3-4	IR	IR	R	IR	IR	R	IR	IR	R

To calculate endogenous exergy destruction in the k^{th} component, a hybrid-cycle was constructed. This is a thermodynamically hypothetical cycle, where one component’s operation is irreversible and all other components operations are reversible. The number of hybrid cycles should be equal to the number of the components in the investigated system. Thus, four hybrid cycles presented in Figure 3 were developed in the present study.

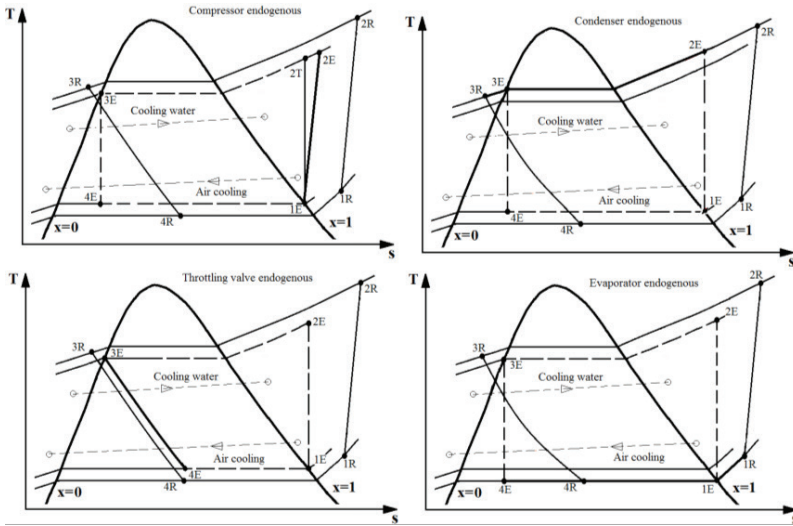


Figure 3. Thermodynamic cycles employed to estimate the endogenous exergy destruction for each refrigeration unit component [11].

4. Results and discussions

Experimental refrigeration system data employed in the exergy and advanced exergy analysis are presented in Table 5. As seen in Table 5, the total exergy efficiency of the system increased with the decrease in test room air temperature. It was found that the system performance was low. The variation in the exergy destruction for each component was associated with the exergy fuel. When the evaporator temperature increased exergetic efficiency decreased. Also, overall system exergetic efficiency increased with a decreased in the condense pinch point temperature difference such as, exergy efficiency; ε , 5.06 %, 11.41 %, and 42.09 %, see in Table 5.

The thermodynamics model cycles and the real cycle findings are presented in Table 6. The table includes exergy destruction, exergy destruction sections in each component at different test unit evaporation and condensation pressures. As seen in Table 6, $\dot{E}_{D,Th}$ each component and the total system were low in all experimental conditions. (\dot{E}_{CM}^{UN} , \dot{E}_{CD}^{UN} , \dot{E}_{TV}^{UN} , \dot{E}_{EV}^{UN} , 0.207, 0.131, 0.031, 0.021 respectively were smaller than \dot{E}_{TOT}^{UN} 0.392). Thus, it was evidenced that the test unit met the standard test requirements, since the unavoidable exergy destruction in each component were low. The $\dot{E}_{D,k}^{EX}$ in the evaporator was very small when compared to each component's, $\dot{E}_{D,k}^{EX}$ value. This same trend was observed in all the test results. Thus, exergy destruction in the evaporator was entirely induced by the evaporator. This indicated that the test unit met the conventional refrigeration test standards.

$\dot{E}_{D,k}^{UN,EN}$, $\dot{E}_{D,k}^{UN,EX}$, $\dot{E}_{D,k}^{AV,EN}$, $\dot{E}_{D,k}^{AV,EX}$ exergy destruction values for each component and the overall system were calculated, as presented in Table 7.

The highest $\dot{E}_{D,k}^{AV,EN}$ was observed in the condenser. Thus the improvement of the condenser efficiency could reduce the exergy destruction in the overall system. The $\dot{E}_{D,k}^{AV,EX}$ was calculated positive for all components in all the tests except the evaporator for operation temperature of -4.18 °C. This finding demonsrated that the improvement of the system iwas unnecessary and the system worked well.

$\dot{E}_{D,k}^{Mex}$ mexogenous exergy destruction was defined to understand the intractions between the system components. As seen in Table 8. $\dot{E}_{D,k}^{Mex}$ mexogenous exergy destruction was caused by the impact of the other components when a component was removed from the unit. It was determined that the exergy destruction the condenser was significantly affected by the other components in all test room temperatures ($\dot{E}_{CD,k}^{MEX,r}$ =1.280, 1.550, 0.559).

Table 5. Exergy destruction and exergy efficiency for the real cycle.

Comp.	Test room air temperature 10°C $\Delta T_{CD} = 13^{\circ} C$ $\Delta T_{EV} = 4^{\circ} C$					Test room air temperature 0°C $\Delta T_{CD} = 12.12^{\circ} C$ $\Delta T_{EV} = 5.37^{\circ} C$					Test room air temperature -18°C $\Delta T_{CD} = 7.93^{\circ} C$ $\Delta T_{EV} = 5.88^{\circ} C$				
	$\dot{E}_{Ex,F}$ [kW]	$\dot{E}_{Ex,P}$ [kW]	$\dot{E}_{D,k}$ [kW]	ϵ [%]		$\dot{E}_{Ex,F}$ [kW]	$\dot{E}_{Ex,P}$ [kW]	$\dot{E}_{D,k}$ [kW]	ϵ [%]		$\dot{E}_{Ex,F}$ [kW]	$\dot{E}_{Ex,P}$ [kW]	$\dot{E}_{D,k}$ [kW]	ϵ [%]	
CM	2.1	1.621	0.478	77.21		3.000	2.436	0.563	81.21		3	2.317	0.682	77.26	
CD	0.983	0.190	0.793	19.38		1.299	0.233	1.065	17.99		0.622	0.126	0.496	20.33	
TV	0.627	0.406	0.220	64.85		1.112	0.736	0.375	66.21		1.668	1.400	0.268	83.93	
EV	0.199	0.106	0.093	53.12		0.745	0.342	0.403	45.92		1.402	1.262	0.139	90.03	
Tot	2.1	0.106	1.585	5.06		3.000	0.342	2.408	11.41		3	1.262	1.586	42.09	

Table 6. Advanced exergy analysis and two-part splitting approach.

	Test room air temperature 10°C $\Delta T_{CD} = 13^o\ C$ $\Delta T_{EV} = 4^o\ C$					Test room air temperature 0°C $\Delta T_{CD} = 12.12^o\ C$ $\Delta T_{EV} = 5.37^o\ C$					Test room air temperature -18°C $\Delta T_{CD} = 7.93^o\ C$ $\Delta T_{EV} = 5.88^o\ C$				
	$\dot{E}_{D,Th}$ [kW]	$\dot{E}_{D,k}^{UN}$ [kW]	$\dot{E}_{D,k}^{AV}$ [kW]	$\dot{E}_{D,k}^{EN}$ [kW]	$\dot{E}_{D,k}^{EX}$ [kW]	$\dot{E}_{D,Th}$ [kW]	$\dot{E}_{D,k}^{UN}$ [kW]	$\dot{E}_{D,k}^{AV}$ [kW]	$\dot{E}_{D,k}^{EN}$ [kW]	$\dot{E}_{D,k}^{EX}$ [kW]	$\dot{E}_{D,Th}$ [kW]	$\dot{E}_{D,k}^{UN}$ [kW]	$\dot{E}_{D,k}^{AV}$ [kW]	$\dot{E}_{D,k}^{EN}$ [kW]	$\dot{E}_{D,k}^{EX}$ [kW]
Component															
CM	0	0.207	0.270	0.224	0.253	0	0.048	0.515	0.213	0.350	0	0.146	0.535	0.289	0.392
CD	0.149	0.131	0.661	0.342	0.451	0.208	0.504	0.561	0.520	0.544	0.013	0.020	0.475	0.236	0.259
TV	0.098	0.031	0.188	0.150	0.069	0.226	0.230	0.145	0.279	0.096	0.082	0.118	0.150	0.214	0.054
EV	0.002	0.021	0.071	0.081	0.011	0.085	0.137	0.265	0.394	0.008	0.014	0.018	0.121	0.132	0.007
TOT	0.2507	0.392	1.193	0.799	0.786	0.519	0.920	1.487	1.408	0.999	0.109	0.303	1.282	0.872	0.713
%	15.80	24.75	75.24	50.40	49.60	21.56	38.22	61.73	58.47	41.53	6.91	19.14	80.85	55.00	44.99

Table 7. The combined approach in advanced exergy analysis.

Component	Test room air temperature 10°C $\Delta T_{CD} = 13^{\circ} C$ $\Delta T_{EV} = 4^{\circ} C$				Test room air temperature 0°C $\Delta T_{CD} = 12.12^{\circ} C$ $\Delta T_{EV} = 5.37^{\circ} C$				Test room air temperature -18°C $\Delta T_{CD} = 7.93^{\circ} C$ $\Delta T_{EV} = 5.88^{\circ} C$			
	$\dot{E}_{D,k}^{UN,EN}$ [kW]	$\dot{E}_{D,k}^{UN,EX}$ [kW]	$\dot{E}_{D,k}^{AV,EN}$ [kW]	$\dot{E}_{D,k}^{AV,EX}$ [kW]	$\dot{E}_{D,k}^{UN,EN}$ [kW]	$\dot{E}_{D,k}^{UN,EX}$ [kW]	$\dot{E}_{D,k}^{AV,EN}$ [kW]	$\dot{E}_{D,k}^{AV,EX}$ [kW]	$\dot{E}_{D,k}^{UN,EN}$ [kW]	$\dot{E}_{D,k}^{UN,EX}$ [kW]	$\dot{E}_{D,k}^{AV,EN}$ [kW]	$\dot{E}_{D,k}^{AV,EX}$ [kW]
CM	0.505	-0.297	-0.280	0.551	0.005	0.042	0.207	0.307	0.187	-0.041	0.101	0.433
CD	0.004	0.126	0.337	0.324	0.134	0.369	0.385	0.175	0.002	0.020	0.236	0.238
TV	0.073	-0.041	0.077	0.111	0.211	0.018	0.068	0.077	0.268	-0.055	0.040	0.109
EV	0.059	-0.037	0.022	0.049	0.002	0.137	0.394	-0.129	0.139	-0.036	0.078	0.043

Table 8. $\dot{E}_{D,k}^{Mex}$ for each component.

		Test room air temperature		
		10°C $\Delta T_{CD} = 13^{\circ} C$ $\Delta T_{EV} = 4^{\circ} C$	0°C $\Delta T_{CD} = 12.12^{\circ} C$ $\Delta T_{EV} = 5.37^{\circ} C$	-18°C $\Delta T_{CD} = 7.93^{\circ} C$ $\Delta T_{EV} = 5.88^{\circ} C$
Component	Affected component	$\dot{E}_{D,k}^{EX,r} [kW]$	$\dot{E}_{D,k}^{EX,r} [kW]$	$\dot{E}_{D,k}^{EX,r} [kW]$
CM	CD	0.777	1.069	0.645
	EV	0.484	0.656	0.392
	TV	0.446	0.602	0.371
	Mex	-1.229	-1.764	-0.726
CD	CM	0.013	0.140	0.252
	EV	-0.231	-0.286	-0.147
	TV	-0.269	-0.339	-0.168
	Mex	1.280	1.550	0.559
TV	CM	0.254	0.364	0.206
	EV	0.010	-0.062	-0.193
	CD	0.303	0.350	0.059
	Mex	-0.347	-0.276	0.195
EV	CM	0.419	0.390	0.355
	TV	0.136	-0.090	-0.064
	CD	0.468	0.376	0.209
	Mex	-0.930	-0.273	-0.360

To explain the distribution of exergy destruction between the components Figure 4, Figure 5 and Figure 6 are presented as below.

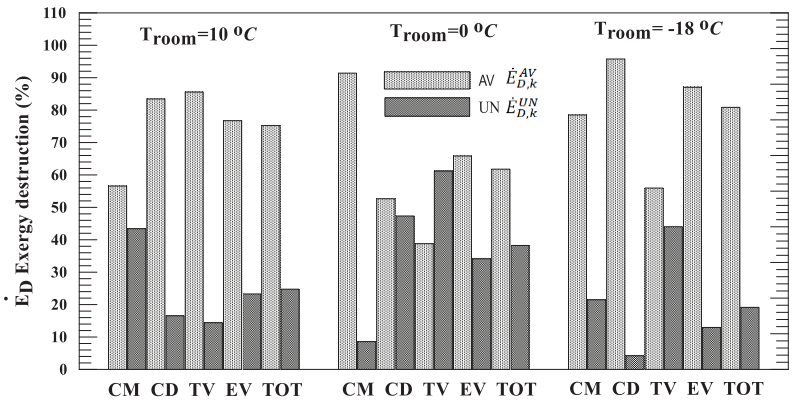


Figure 4. Ratio of $\dot{E}_{D,k}^{AV}$ and $\dot{E}_{D,k}^{UN}$ for each unit to total exergy destruction.

The magnitude of $\dot{E}_{D,k}^{AV}$ and $\dot{E}_{D,k}^{UN}$ in each component and the overall system exergy destructions are presented in Figure 4. Comparison of the $\dot{E}_{d,k}^{UN}$ in Figure 4 revealed that \dot{E}_{CM}^{UN} was very low in each operating condition. It was determined that the \dot{E}_{EV}^{UN} part change in the evaporator depended on the mass air flow rate and inlet processed air temperature in the evaporator.

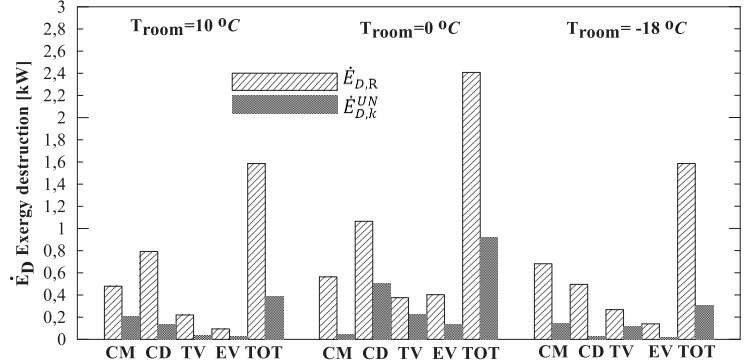


Figure 5. Comparison of $\dot{E}_{D,R}$ and $\dot{E}_{D,k}^{UN}$ parts for each component.

A comparison of $\dot{E}_{D,R}$ and $\dot{E}_{D,k}^{UN}$ based on the real cycle and unavoidable cycle parameters is presented in Figure 5. It was observed that the actual and $\dot{E}_{D,k}^{UN}$ values determined for each

component remained approximately the same with the change in the test room temperature.

The ratio of $\dot{E}_{D,k}^{EN}$ and $\dot{E}_{D,k}^{EX}$ to total exergy destruction is presented in Figure 6 for each unit and all test data. The ratio of $\dot{E}_{D,k}^{EN}$ and $\dot{E}_{D,k}^{EX}$ to total exergy and destruction in each component in different test conditions, exhibited approximately similar trends. The discrepancies were due to the difference between the refrigerant (R404a) pressure and the mass flow rates of and condenser operating conditions.

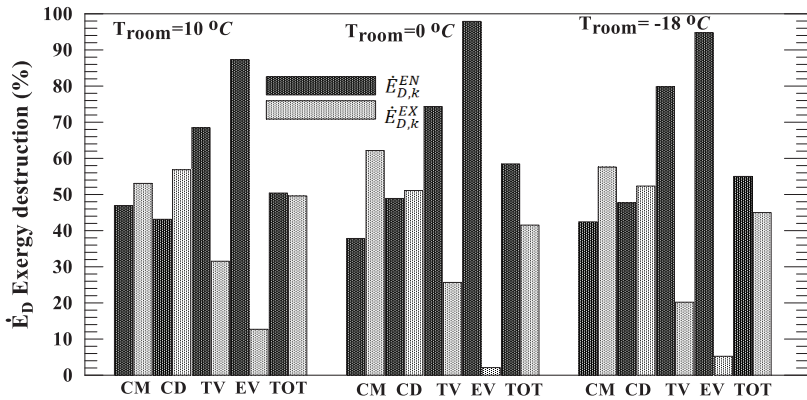


Figure 6. Ratio of $\dot{E}_{D,k}^{EN}$ and $\dot{E}_{D,k}^{EX}$ parts generated in each unit to total exergy destruction

5. Conclusion

The total avoidable exergy destruction caused by the condenser was higher than those induced by the remaining components. The operation condition of condenser should be revised or improved.

- It was demonstrated that the test unit it met standard test requirements.
- Exergy destruction in the evaporator was generated by itself.
- The main finding of this study is that the irreversibility generated in each evaporator component was negligible.

Acknowledgment

The authors would like to thank Friterm Company for sharing the experimental data. The authors also thank Dr. Hüseyin ONBAŞIOĞLU for his suggestions and contributions. Also, the authors would like to

thank Prof. Dr. Seyhan UYGUR ONBAŞIOĞLU for her valuable comments and contributions.

Nomenclature

E	: Exergy	[W]
e	: Specific exergy	[J/kg]
h	: Enthalpy,	[J/kg]
s	: Entropy	[J/kgK]
\dot{m}	: Mass flow rate	[kg/s]
T	: Temperature	[K]
P	: Pressure	[kPa]
ε	: Exergetic efficiency	[%]
y	: Ratio of exergy destruction for “k”th component to the total exergy destruction [%]	

Abbreviations

AV	Avoidable
CD	Condenser
CM	Compressor
D	Destruction
EN	Endogenous
EV	Evaporator
EX	Exogenous
UN	Unavoidable
Tot	Total
TV	Throttling valve
P	Exergy product, Pressure
M	Mechanical exergy
T	Thermal exergy, Temperature

Subscript

air Air

o Dead state

c Constant

F Exergy fuel

P Exergy product

in Inlet

k Component

L Loss

mex Mexogenous

out Outlet

R Real

Theo Theoretical

Tot Total

w Water

C Cycle

IR Irreversible

R Reversible

References

1. Ashare, 1984. Method of Testing for Rating Room Air conditioners and Packaged Terminal air Conditioners. ANSI/ASHRAE Standard 16-1983, ASHRAE Publications, Atlanta, GA.
2. Tsatsaronis, T. and Morosuk, T. Advanced thermodynamic (exergetic) analysis. *Journal of Physics: Conference Series*. 2012. p 395.
3. Wang L., Yang Z., Sharama S., Mian, A., Lin T E., Tsatsaronis, T., Marechal F. And Yang, Y. A Review of Evaluation, Optimization and Synthesis of Energy Systems: Methodology and Application to Thermal Power Plants. *Energies*. 2019. 12, 73; doi:10.3390/en12010073.
4. Petrakopoulou, F., Tsatsaronis, G., Morosuk, T., Carassai, A. Conventional and advanced exergetic analyses applied to a combined cycle power plant. *Energy*. 2012. 41(1): p .146–52.
5. Geete, A, Sharma, M, Shrimali, P. Entropy generation and exergy destruction analyses for vapor compression refrigeration system with various refrigerants. *SN Applied Sciences*. Springer Nature Switzerland AG 2019. 10.1007/s42452-019-0798-4.
6. Bayrakçı H.C., Özgür, A.E. Energy and exergy analysis of vapor compression refrigeration system using pure hydrocarbon refrigerants. *International Journal of Energy Research*. 2009. Vol 33:p.1070-1075.
7. Ouadha, A., En-caer M., Adjlout, L. and Lmine, O. Exergy analysis of a two-stage refrigeration cycle using two natural substitutes of HCFC22. *International Journal of Exergy*. 2005. Vol 2, N0 1, 10.1504/IJEX.2005.006430
8. Bai T., Yu J., Yan, G. Advanced exergy analysis of an ejector expansion transcritical CO₂ refrigeration system. *Energy Conversion and Management*. 2016. 126: p.850-861.
9. Buhler, F., Toung-Wang N., Kjeear, J J., and Brian, E. Energy, exergy and advanced exergy analysis of a milk processing factory. *Proceedings of ECOS, The 29th International conference on efficiency, cost, optimization, simulation and environmental impact of energy system*. 2016. pp 1-13.
10. Kelly, S., Tsatsaronis G., Morosuk, T. Advanced exergetic analysis: Approaches for splitting the exergy destruction into endogenous and exogenous parts. *Energy*. 2009. 34: p.384–391.

11. Şöhret, Y., Açikkalp, E., Hepbaşlı, A., Karakoç T H. Advanced exergy analysis of an aircraft gas turbine engine: Splitting exergy destructions into parts. *Energy*. 2015. 90: p.1219-1228.
12. Balli, O. Advanced exergy analysis to evaluate the performance of a military aircraft turbojet engine (TJE) with after burner system: Splitting exergy destruction into unavoidable/avoidable and endogeneous/exogenous. *Applied Thermal Engineering*. 2017. 111:152-169.
13. Ghorbani, B., Roshani, H. Advanced exergy and exergoeconomic analysis of the integrated structure of simultaneous production of NGL recovery and liquefaction. *Trans Phenom Nano Micro Scales*. 2018. 6 (Specials):8-14. Doi: 0 22111/tpnms.23743.1140.
14. Gullo P., Hafner A., and Banasiak, K. Thermodynamic Performance Investigation of Commercial R744 Booster Refrigeration Plants Based on Advanced Analysis. *Energies*. 2019. 354, doi:10.3390/en12030354.
15. Chen, J. Investigation of vapour ejectors in heat driven ejectors refrigeration system. Doctor thesis. Division of applied thermodynamics and refrigeration department of energy technology, Royal Institute of Technology, KTH , SE-100 44 Stockholm, Sweden. 2014.
16. Azizi, T., Boyarhchihi, F A. 2014. Assessment of a Real Combined Cycle Power Plant with Supplementary Firing Based on Advanced Exergy/Exergoeconomic Methods. *Iranian Journal of Mechanical Engineering*. (15), No. 2.
17. Yunhai Li, Jianyong Chen, Xu Lin, Zhi Yang, Ying Chen & Xianglong Luo . Quantification on the Effects of Liquid-Vapor Separation in Air-Conditioning System by using Advanced Exergy Analysis. *Journal of Thermal Science* volume 29, pages597–608. 2020).
18. Emin Açikkalp, Haydar Aras, Arif Hepbaşlı. Advanced exergy analysis of a trigeneration system with a diesel–gas engine operating in a refrigerator plant building. *Energy and Buildings*. Volume 80, September 2014, Pages 268-275.
19. Selay Sert and Firuz Balkan Determination of avoidable and unavoidable exergy destructions of furnace-air preheater coup system in a petrochemical plant. *Journal of Thermal Engineering, Technical Note – JTEN* – 2015 – 76.
20. Hui Liu, Qing He and Sarmad Bin Saeed. Thermodynamic analysis of a compressed air energy storage system through advanced exergetic

- analysis. *Journal of Renewable and sustainable energy*. 2016. 8, 034101. pp 1-17.
21. Tsatsaronis, G. and Morosuk, T., Kelly S. 2006. Endogeneous and Exogeneous Exergy Destruction in Thermal System”, Conference paper. DOI: 10.1115/IMECE, 13675.
22. Liu, H., He Q., Saeed, S.B. Thermodynamic analysis of a compressed air energy storage system through advanced exergetic analysis. *Journal of Renewable and Sustainable Energy*. 2016. 8, 034101.
23. Gullo P, Elmegaard B, Cortell G. Advanced exergy analysis of a R744 booster refrigeration system with parallel compression. *Energy*. Doi:10.1016/j.energy.04.043.
24. Cihan Nacak. Depending on the ship route, determination of the performance of the ship cooling system by using energy, exergy, advanced exergy and exergy economy methods. 2020. Karadeniz Technical University Sürmene Faculty of Marine Sciences - Naval Architecture and Marine Machines Engineering, Trabzon, Turkey. Master Thesis.
25. Cihan Nacak and Betül Saraç. The performance assessment of a refrigeration system which exists on a cargo vessel influenced by seawater-intake temperature. *Journal of Thermal Analysis and Calorimetry*. 2020. <https://doi.org/10.1007/s10973-020-10060-y>. In press.
26. Jianyong Chen, Hans Havtun, Björn Palm. Conventional and advanced exergy analysis of an ejector refrigeration system. 2015. *International Journal of Applied Energy*. 144:139-151. DOI: 10.1016/j.apenergy.2015.01.139
27. Mengxiao Yu, Peizhe Cui, Yinglong Wang, Zhiqiang Liu, Zhaoyou Zhu and Sheng Yang. Advanced Exergy and Exergoeconomic Analysis of Cascade Absorption Refrigeration System Driven by Low-Grade Waste Heat. *ACS Sustainable Chem. Eng.* 2019. 7, 19, 16843–16857.
28. Zafer Erbay, Arif Hepbasli. Application of conventional and advanced exergy analyses to evaluate the performance of a ground-source heat pump (GSHP) dryer used in food drying. *Energy Conversion and Management*. 2014. Volume 78, Pages 499-507.
29. Kotas, T.J. The exergy method of thermal plant analysis. 1985, Anchor Brendon Ltd.

Chapter 15

THE HYBRID-NANOFLUIDS REINFORCED WITH IRON(III) OXIDE AND COPPER(II) OXIDE

Ahmet B. DEMIRPOLAT¹

Ercan AYDOĞMUŞ²

1 Turgut Özal University, Arapgir Vocational School, Electronics and Automation, Malatya, Turkey. E-mail: ahmetb.demirpolat@ozal.edu.tr.

(Orcid: <https://orcid.org/0000-0003-2533-3381>)

2 Firat University, Faculty of Engineering, Chemical Engineering, Elazığ, Turkey. Corresponding Author: ercanaydogmus@firat.edu.tr.

(Orcid: <https://orcid.org/0000-0002-1643-2487>)

1. INTRODUCTION

In this study, the change of thermal conductivity coefficient with temperature and concentration of the hybrid nanofluids obtained by using iron (III) oxide and copper (II) oxide as nanoparticles was investigated. The nano- $\text{Fe}_2\text{O}_3/\text{CuO}$ powders were used to increase the thermal conductivity coefficient of the water used in the residential heating system. Thermal conductivity coefficients were measured by increasing the temperature of the water at room temperature up to 70 °C. It has been observed that the thermal conductivity coefficient tends to go up with the increase in temperature. In the experiments, it was seen that when pure water is used instead of heating water, the thermal conductivity efficiency goes down. Besides, the change in the thermal conductivity coefficient was investigated by studying the nano- $\text{Fe}_2\text{O}_3/\text{CuO}$ powders concentrations at 0.1wt%, 0.2wt%, 0.3wt%, 0.4wt%, and 0.5wt%. It was observed that as the concentration ratio increased, the thermal conductivity coefficient increased, but after the water reached a certain saturation (0.3wt%), this coefficient reached equilibrium.

Hybrid mixtures were prepared with 0.3wt% nanopowder ratio water at the concentration where the nanopowder reached maximum saturation. $\text{Fe}_2\text{O}_3/\text{CuO}$ mixing ratios have been studied at 4/1, 3/1, 2/1, 1/1, 1/2, 1/3, and 1/4 by mass ratios. Also, it has been determined that the viscosity of the heating water decreases with the increase in temperature, while the viscosity increases with the nanopowder concentration. According to the results, it has been evaluated that the thermal conductivity coefficient of the water used in residential heating increased approximately 1.22 times to hybrid nanopowders. The results obtained from the experimental data were determined with the help of statistical analysis, giving results compatible with the developed theoretical models. To meet the increasing energy need, such studies with efficient and economical methods will gain importance in the future.

It is known that the use of nanofluids is widespread in different applications today. Generally, nanopowder can be used to change the properties of liquids such as thermal conductivity coefficient, viscosity, surface tension, and electromagnetic structure. In this study, the hybrid uses of two nanoparticles (Fe_2O_3 and CuO) with different properties will be investigated. When the sources in the literature are searched, it is seen that nanofluids have been developed for many purposes.

In an article using Fe_3O_4 nanopowder, while the thermal conductivity coefficient of aqueous nanofluids increased with the increase of temperature, its viscosity decreased [1]. In research using iron oxide (Fe_2O_3) and zinc oxide (ZnO) nanofluids, electromagnetic waves were provided for oil

recovery in open seas. Electromagnetic waves are produced with the help of an antenna developed and nanofluids can be directed to the desired areas. In the results obtained, recovery of petroleum and its derivatives was achieved by injecting 0.1wt.% iron oxide nanofluid. [2]. In a study where iron oxide nanoparticles were obtained by laser pyrolysis technique, nanoparticle mixtures with an average particle diameter of 4-5 nm were prepared using an ultrasonic homogenizer. The heat transfer properties of Fe_2O_3 -nanofluids have been investigated depending on the temperature and concentration using a two-phase closed thermosiphon. It has been determined that nanoparticle concentration and temperature are effective in increasing the heat transfer coefficient [3].

In another study comparing the effect of particle size on Fe_2O_3 /kerosene nanofluid in a closed-loop vibrating heat pipe system under a magnetic field, it was studied between 10 nm and 30 nm. The heat transfer rate and temperature distribution were investigated by exposure to the magnetic field. Both the heat transfer coefficient and thermal performance of the vibrating heat pipe increased with the addition of Fe_2O_3 nanoparticles in the magnetic field. According to the obtained evaluations, optimum nanoparticle size was found in 20 nm particle size of iron oxide for the best heat transfer performance [4]. An experimental study, obtained iron oxide nanoparticles by laser pyrolysis technique, has been investigated in different thermal performance (0%, 2%, and 5.3%) of thermosiphon heat pipe. The results show that adding 5.3% by volume iron oxide nanoparticles has a much better thermal performance than deionized water [5].

By using iron oxide nanofluid, the stability and thermal efficiency of the flat plate solar collector have been analyzed over time. In the research, the stability of the nanofluid with iron oxide/ethylene glycol and distilled water has been evaluated depending on the time. Thermal efficiency experiments in solar collectors have been investigated for Fe_3O_4 at 30-150 L/h flow rates and 0.2-1% by volume. Optimum results were found with 1% Fe_3O_4 by volume and high efficiency at 30 L/h flow rate. Also, when its thermal efficiency was compared with time (15 days), it was seen that the performance of nanofluids did not decrease much [6]. Another article compares the thermal efficiency of nanofluids in a single-basin solar system. Thermal performances of aluminum oxide (Al_2O_3), zinc oxide (ZnO), iron oxide (Fe_2O_3), and tin oxide (SnO_2) nanofluids have been evaluated. The thermal efficiency of aluminum oxide (Al_2O_3) is 29.95%, zinc oxide (ZnO) is 12.67%, and tin oxide (SnO_2) is 18.63 more than the water [7].

In the study investigating the effect of aggregation of nanofluids in stable and unstable conditions, thermal conductivity, viscosity, and size distribution of Fe_3O_4 and CuO nanoparticles have been evaluated. Agglomeration has been verified to have an important role and functionality

in the thermal properties of nanofluids. It has increased the thermal performance by increasing the thermal conductivity and viscosity of the agglomeration of microscopic nanofluids [8].

Parameters such as thermal conductivity, type of nanoparticle, fluid, particle size, volume fraction, and suspension temperature in oxide and metallic nanofluids were investigated. Experimental dataset and temperature fluctuation tracking were performed for thermal conductivity measurement of liquids. It has been found that metallic nanofluids show higher thermal performance than oxide nanofluids. Thermal conductivity increased inversely as nanopowder particle size decreased. It has been observed that the increase in temperature significantly increases the thermal conductivity of the nanofluids. When nanoparticle suspensions were compared, it was determined that the volume fraction was in a nonlinear relationship with thermal conductivity [9]. In an article where Al_2O_3 , CuO , TiO_2 , and Fe_3O_4 nanofluids were compared in the same volume fraction, the highest thermal conductivity was found in Fe_3O_4 -powders. The high thermal conductivity values of Fe_3O_4 nanofluid in experimental observations can be attributed to nanoparticle aggregation and alignment. It has been determined that the nonlinear thermal conductivity of nanofluids is mainly due to nanoparticle alignment and aggregation [10].

In this research, the thermal efficiency of hybrid-nanofluids formed by iron (III) oxide with strong magnetic properties and copper (II) oxide nanoparticles with high thermal conductivity have been investigated. The thermal conductivity efficiency of the hybrid mixture has reached higher values than the nanoparticles used alone. These nanoparticles, which are compatible with each other, have provided advantages in terms of both viscosity and thermal conductivity even at high temperatures.

2. MATERIALS AND METHODS

2.1. Materials

Iron (III) oxide, copper (II) oxide, triglyceride, and acetic acid have been supported by Nanografi and Sigma Aldrich. Using distilled water, nanofluids of various concentrations were formed. The total mass of the mixture was 1 kg, with concentrations of 0.1 percent, 0.2 percent, 0.3 percent, 0.4 percent, and 0.5 percent. Fe_2O_3 (0.3wt%) and CuO (0.3wt%) components were combined in proportions of 4/1, 3/1, 2/1, 1/1, 1/2, 1/3, and 1/4 by mass for the hybrid mixtures. Thermal conductivity and viscosity were used to determine the proper mixing ratios.

2.2. Methods

The maximum amount of nanoparticles that water can hold was calculated as 0.3 percent by mixing iron (III) oxide and copper (II) oxide

in different amounts by mass. Even at 1000 rpm fluid rotation speed, precipitation increased in the bottom of the water when higher ratios of nanoparticles were used in experiments. Acetic acid (5 mL), triglyceride (95 mL), distilled water, and nanoparticles were added to a total of 1L of the mixture. These additives provide a homogeneous suspension of the hybrid and nanofluids as colloidal. According to the experimental study plan in Table 1, the maximum efficiency was obtained in the 6th experiment.

Table 1. *The mixing ratio of nanoparticles by mass*

Experiments	Fe ₂ O ₃ (wt.%)	CuO (wt.%)
1	4: (80%)	1: (20%)
2	3: (75%)	1: (25%)
3	2: (67%)	1: (33%)
4	1: (50%)	1: (50%)
5	1: (33%)	2: (67%)
6	1: (25%)	3: (75%)
7	1: (20%)	4: (80%)
8	0: (0%)	1: (100%)
9	1: (100%)	0: (0%)

3. RESULTS AND DISCUSSIONS

In this study, the variation of both viscosity and thermal conductivity with the temperature of the hybrid-nanofluid formed by the determined iron (III) oxide and copper (II) oxide was investigated.

In Fig. 1, the relative thermal conductivity coefficients of the experimental measurements concerning water are compared. In the 6th and 7th experiments, the thermal conductivity efficiency of hybrid mixtures was found to be maximum, and in the 1st and 9th experiments, it was found to be minimum. Also, for the hybrid with the highest efficiency (6th experiment), it was determined in Fig. 2 that the relative thermal conductivity coefficient increased in direct proportion to the temperature.

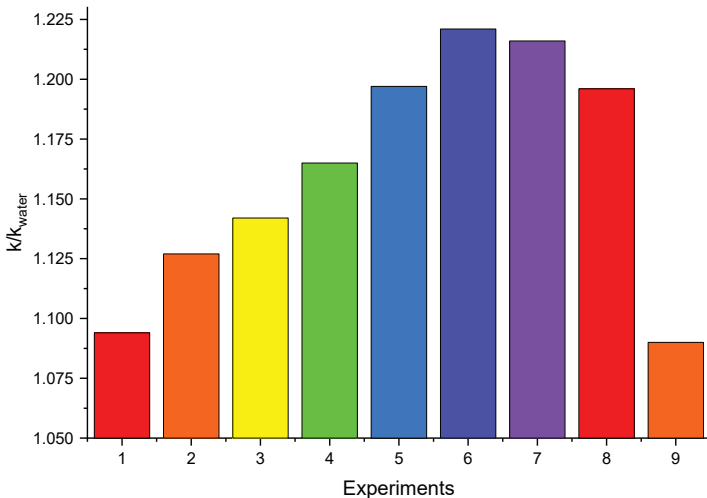


Fig. 1. Comparison of relative thermal conductivity coefficient concerning water in experimental studies at 60 °C

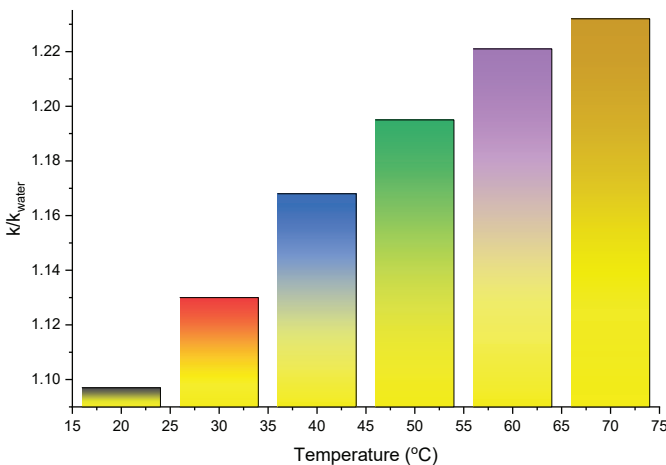


Fig. 2. The change of relative thermal conductivity coefficient of hybrid-nanofluid (6th experiment) with temperature

Fig. 3 shows the variation of the viscosity of the hybrid-nanofluid with temperature. It has been determined that viscosity is more stable than water.

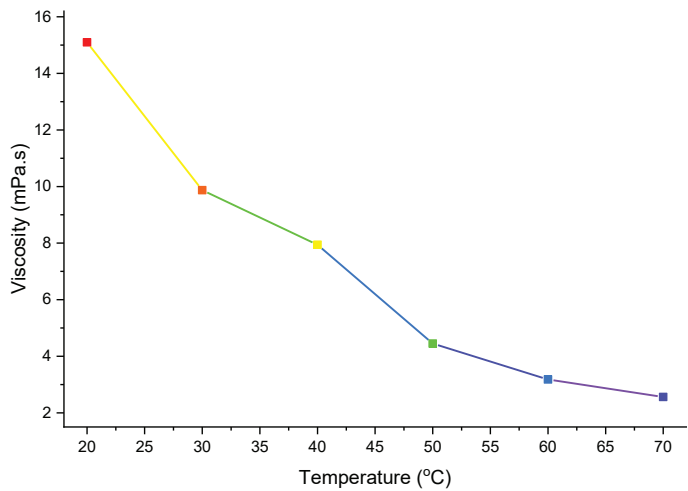


Fig. 3. *The change of viscosity of hybrid-nanofluid (6th experiment) with temperature*

Theoretical modeling has been developed by evaluating the experimental data according to the Response Surface Methodology (RSM). The thermal conductivity coefficient of hybrid-nanofluids has been modeled depending on the concentration and density. As can be seen in Fig. 4, as the density and nanoparticle concentration of hybrid-nanofluids increased, the thermal conductivity coefficient went up.

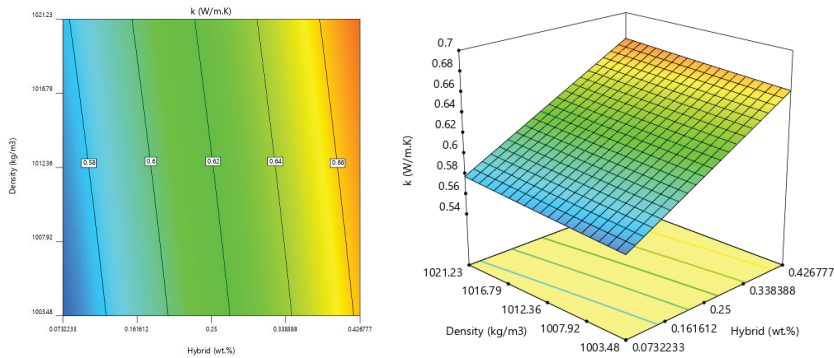


Fig. 4. *The change of concentration of hybrid-nanofluid with density according to RSM*

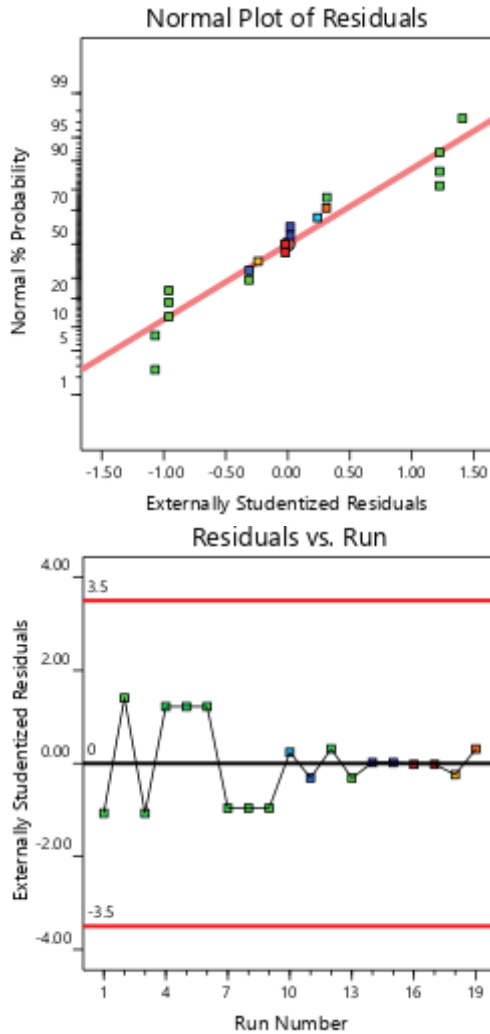


Fig. 5. *The compatibility of experimental data with the theoretical model according to RSM*

Fig. 5 shows the distribution of model data evaluated by statistical analysis. High R^2 (0.9985) and low error values (SST=0.0054) indicate that the model and experimental data are compatible. The high significance of RSM results (p -value=0.0001) strengthens the compatibility of the model equation in Eq. (1) with experimental data. Eq. 1 shows the equation of thermal conductivity coefficient (k) depending on density (ρ) and hybrid concentration (C) by mass.

$$k = +3.47339 + 0.430861 \times C - 0.006454 \times \rho - 0.000159 \times C \times \rho + 0.000889 \times C^2 + \rho^2 \times 3.5 \times 10^{-6} \quad (1)$$

Fig. 6 shows the SEM image of CuO nanoparticles (50 nm and below) distribution and geometric structure of copper (II) oxide.

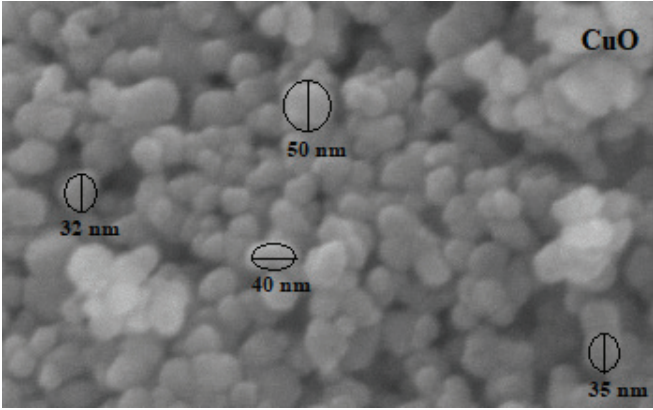


Fig. 6. SEM image of CuO oxide nanoparticles (experiment 8)

In the FTIR spectrum in Fig. 7, Cu-O bonds in the 400-600 cm wavelength range and O-H bonds at a wavelength of 3150-3450 cm are seen [11].

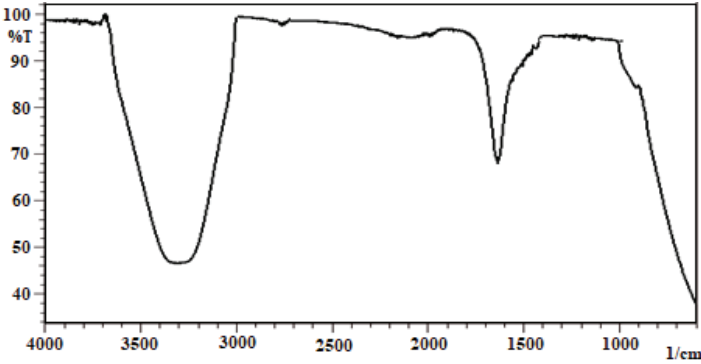


Fig. 7. FTIR spectrum of CuO oxide nanofluids (experiment 8)

CONCLUSIONS

The use of nanoparticles in a hybrid form has been shown to improve thermal conductivity efficiency over the use of nanoparticles alone. Temperature reduced the viscosity of both nanofluids and hybrid-nanofluids. The thermal conductivity coefficient of nanoparticle reinforced nanofluids increased as the temperature increased. CuO had a better thermal conductivity effect on the nanofluid than Fe_2O_3 . Nanofluids' viscosity and thermal conductivity have often outperformed water. The density of the nanofluid increased as the concentration of nanoparticles in the water increased.

The model equality obtained in the RSM results and the experimental results were found to be compatible with statistical analysis.

REFERENCES

- [1] Shima, P. D., Philip, J., & Raj, B. (2010). Dependence on Thermal Conductivity and Viscosity. *J. Phys. Chem. C*, 114, 18825–18833.
- [2] Yahya, N., Kashif, M., Shafie, A., Solemani, H., Zaid, H. M., & Latiff, N. R. A. (2014). Improved oil recovery by high magnetic flux density subjected to iron oxide nanofluids. *Journal of Nano Research*, 26, 89–99.
- [3] Huminic, G., & Huminic, A. (2011). Heat transfer characteristics of a two-phase closed thermosyphons using nanofluids. *Experimental Thermal and Fluid Science*, 35(3), 550–557.
- [4] Goshayeshi, H. R., Safaei, M. R., Goodarzi, M., & Dahari, M. (2016). Particle size and type effects on heat transfer enhancement of Ferro-nanofluids in a pulsating heat pipe. *Powder Technology*, 301, 1218–1226.
- [5] Huminic, G., Huminic, A., Morjan, I., & Dumitrache, F. (2011). Experimental study of the thermal performance of thermosyphon heat pipe using iron oxide nanoparticles. *International Journal of Heat and Mass Transfer*, 54(1–3), 656–661.
- [6] Choudhary, S., Sachdeva, A., & Kumar, P. (2021). Time-based analysis of stability and thermal efficiency of flat plate solar collector using iron oxide nanofluid. *Applied Thermal Engineering*, 183(April 2020), 115931.
- [7] Elango, T., Kannan, A., & Kalidasa Murugavel, K. (2015). Performance study on single basin single slope solar still with different water nanofluids. *Desalination*, 360, 45–51.
- [8] Shima, P. D., Philip, J., & Raj, B. (2010). Influence of aggregation on thermal conductivity in stable and unstable nanofluids. *Applied Physics Letters*, 97(15), 1–4.
- [9] Patel, H. E., Sundararajan, T., & Das, S. K. (2010). An experimental investigation into the thermal conductivity enhancement in oxide and metallic nanofluids. *Journal of Nanoparticle Research*, 12(3), 1015–1031.
- [10] Zhu, H., Zhang, C., Liu, S., Tang, Y., & Yin, Y. (2006). Effects of nanoparticle clustering and alignment on thermal conductivities of Fe₃O₄ aqueous nanofluids. *Applied Physics Letters*, 89(2), 023123.
- [11] Karthick Kumar, S., Murugesan, S., & Suresh, S. (2014). Preparation and characterization of CuO nanostructures on copper substrate as selective solar absorbers. *Materials Chemistry and Physics*, 143(3), 1209–1214.

Chapter 16

**INNOVATIVE EXPLORATION ON MODULAR
BELT CONVEYOR TRANSPORTATION
MECHANISIM BY DEFORMATION,
VON-MISES STRESS MECHANICAL
AND CFD ANALYSIS IN
MATERIAL HANDLING**

Özdoğan KARAÇALI¹

¹ Özdoğan Karaçalı, Associate Prof. Dr.

Department of Mechanical Engineering, Faculty of Engineering, Istanbul University-
Cerrahpaşa, Avcılar, Istanbul, (34320) Turkey

Conveyor systems, which are generally used in material handling in many sectors of the global industry, especially in the food, mining, and agricultural industries provide high performance and ease of work in machines. The objective of this research is to analyze analytically a belt conveyor to maintain material transfer by mechanic modeling. The conveyor forced by the pulling power while the material being transported. Result of the stresses during the operation caused by the pulling force, wear on the drive drum or chain gears and fractures, deformation, fails in the shaft are observed. Modeling method of the conveyor according to design criteria of material strength that will reduce the stresses of the drive drum and shaft was also considered. In order to achieve the purpose of the study, Finite element method (FEA) was used for structural analysis by ANSYS v20. In this research, the conveyor belt under study is divided into a finite number of elements by calculating the mass of each element. Computational Fluid Dynamics (CFD) was accomplished for realization of realist airflow velocity and pressure analysis to model belt conveyor. The effect of FEA and CFD in ANSYS software, analysis of optimum design results, to achieve the purpose of optimum design has a certain proving importance to optimize the actual conveyor structure. The results of mechanical information analysis obtained in the computational environment were examined and an evaluation was presented for the improvement of conveyor system for designers and manufacture engineers.

Keywords: Belt conveyor, finite element analysis, ANSYS

Introduction

Conveyor system is a mechanical framework that enables easier, safer, faster and more efficient to transport materials with high degree of automation (Bajda M., 2019). In the simplest sense, belt conveyors are machines that function to carry the material laid on a power transmission belt between the loading point and the unloading point (Carretero L., 2019). Its main components consist of a tensioned belt between two drums, much larger than its width and height. Elements that change the direction of the belt, clean the belt and support the belt between the two drums can also be included in the conveyor, depending on the complexity of the needs and the transport problem (DIN 22101, 2016). Depending on the power requirement of the conveyor, power is transferred to the belt over the drum by driving one or two drums by the motor-reducer group. In most bulk material conveyors, the belt has a corrugated profile rather than a flat profile to increase carrying capacity (Dunlop F., 2009).

Belt conveyors operate in a horizontal or vertical plane depending on the friction characteristic of the transported load (Dunlop F., 2009). The classification of belt conveyor was given in (Figure 1). There are many types of conveyors known and known as the belt system used by people to transport raw materials waiting to be processed in places such as factories, slaughterhouses and assembly shops. The classification of belt conveyor was shown in (Figure 2).

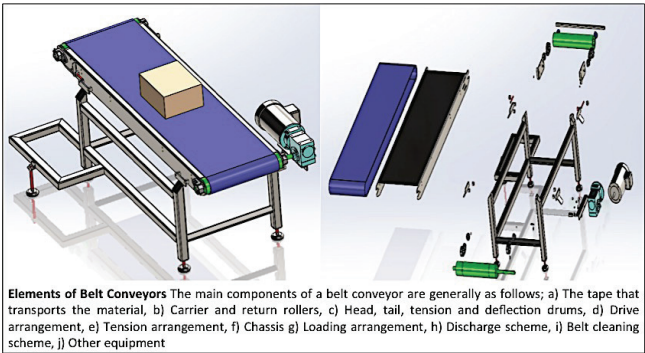


Figure 1. Belt conveyor system and elements

Since the conveyor belt systems operating with a motor power inside are not possible to be used in narrow areas, preferred to be used in larger and spacious areas. Before carrying out the conveying process related to conveyor belts, it is extremely important to consider the material to be transported in the selection of these belts and to choose according to the engine power and the structure of the material to be transported.

The areas of use of conveyor belts are also extremely wide. Since it does not require manpower, it has much more affordable costs compared to many transportation systems. The system, which works with the help of a motor, can easily carry many materials on high and low floors. In this sense, the shape of the floor is important here and when the assembly and material selection is done correctly, it provides the transportation process without causing any problems.

The belt types selected vary according to the shape of the material conveyed and the sectorial structure. The most commonly used belts are general use belts as shown in (Figure 2).

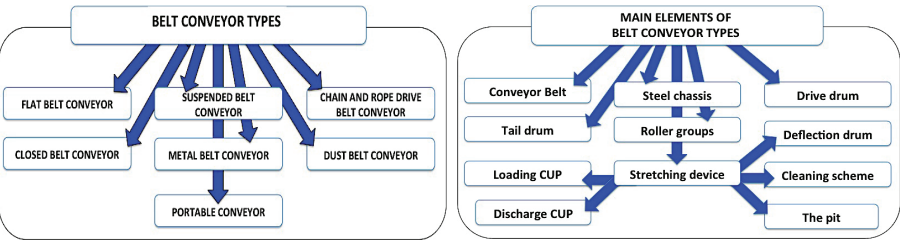


Figure 2. The classification of belt conveyor

The Worldwide Literature Survey

In the current state of the art, different studies can be found for solutions to specific belt conveyor problems at the industrial level (Gerdemeli I., 2014). Conveyor systems are durable and dependable in materials transportation and warehousing. In view of various standards of operation, there are diverse transport frameworks to be specific: gravity, belt, screw, pail, vibrating, chain, spiral, grain conveyor systems etc. The decision however relies on upon the volume to be transported, stature or separation of transportation, nature of material, strategy for generation utilized (Wu Z., 2013), (ISO, 2015). Material taking care of hardware reaches from those that are worked physically to self-loader frameworks and to the ones with high level of robotization. The level of computerization however depends on handling requirements (Lu Y., 2019). A belt comprises of an interminable and adaptable belt of high quality with two end pulleys (driver and driven) at settled positions upheld by rollers. Pulleys are used for providing the drive to the rubber belt through a drive unit gearbox fueled by an electric engine. It likewise helps in keeping up the correct pressure to the belt.

Conveyor equipment selection is a complex, and sometimes, tedious task since there are literally hundreds of equipment types and manufacturers to choose from (Mathaba T., 2017). The expert system approach to conveyor selection provides advantages of unbiased decision-making, greater availability, faster response, and reduced cost as compared to human experts. Expert system and artificial intelligence has become important for industrial conveyor selection.

A simplified approach to modeling rolling contact events on the surface top of a wheel driven elastic belt rubber was reported in (Munzenberger P.J, 2019). In this engineering approach, the basic aim is to control the rolling rubbing friction due to the relationship and hysteresis between grip and slip of a wheel driven belt conveyor. The model is an extension of an existing linear viscoel model from a Maxwell model with three parameters combined with a Winkler basis used to determine the rolling drag due to hysteresis in a conventional flat belt conveyor (Nuttall A., 2017).

The design of a multi-conveyor system in supporting machine loading and unloading has become crucial to management. However, through the mathematical model proposed in this paper, this issue becomes realistically and concretely solvable. Over the years a lot of work has done and is still continuing with great effort to save weight and cost of applications (Rao A. M., 2012). The current trend is to provide weight/cost effective products which meet the stringent requirements. New design of rollers focused on the measurement of static and dynamic resistance of rotating rollers and the impact of new construction on the power consumption of the belt conveyor (Rick G., 2019).

Conveyor equipment selection is a complex, and sometimes, tedious task since there are literally hundreds of equipment types and manufacturers to choose from. The expert system approach to conveyor selection provides advantages of unbiased decision-making, greater availability, faster response, and reduced cost as compared to human experts. Conveyor types are selected on the basis of a suitability score, which is a measure of the fulfillment of the material handling requirements by the characteristics of the conveyor (Shen, J, 2018).

The design of an efficient material handling system which will increase productivity and minimize cost entails the followings; designing the system for continuous flow of material (idle time should be zero); going in for standard equipment which ensures low investment and flexibility; incorporating gravity stream in material stream framework; and ensuring that the proportion of the dead weight to the payload of material taking care of gear is least (Suhas M., 2012). The transportation course influences the general expense of material taking care of. An effective material taking care of gear will decrease cost per volume of material transported and guarantee that materials are conveyed to the creation line securely (Yuan X., 2014). The outline of belt transport framework includes determination of the right measurement of the belt transport parts and other basic parameter values in order to guarantee ideal effectiveness amid stacking and emptying conditions (Wang F.S., 2018).

Materials and Methods for Belt Conveyor Analysis

Methods used in different applications to reduce product costs sometimes cause fails during operation and fatal accidents with equipment. Before application, simulation modeling and mathematical analysis has become important for designers and manufacturers (Yuan X., 2014). These are methodologies such as design change, drum failure, belt design and failure, deformation, energy and efficiency, friction, thinning, operation and maintenance.

The method developed in this study to discover the possible problems and causes of a mechanical strength breakdown and the system of the failure. For this reason, potential risks and corrective actions are modeled by computational simulations and identified the most serious concerns. Conveyor belt evaluation considered as an engineering analysis conducted comprehensively analyzes designs or production processes for development. The simulations provide experiments to find and correct the product weaknesses before they fall into manufacturing environment and the customer's hands.

The von Mises stress is accepted as equivalent stress in this research. Here σ_x , σ_y , σ_z are the corresponding stresses in the X, Y and Z directions as given in equation (1) and (2). τ_x , τ_y , τ_z are corresponding shear stresses in equation (2). The maximum distortion, the von Mises theory known as the octahedral shear stress theory or the von Mises theory, is used to predict the yield of ductile materials. Von Mises states that the fault is transmitted when the distortion energy in the uniaxial voltage reaches the same energy for stress yield. Von Mises stress is also called equivalent tensile stress. It's a special measure of stress that serves as an approach to combine all stress components into one value. Thanks to that it can be compared with material's strength when multi-axial loading occurs. The formula used to calculate von Mises stress equation (1) and (2) is as follows:

$$\sigma = \sqrt{0.5[(\sigma_x - \sigma_y)^2 + (\sigma_y - \sigma_z)^2 + (\sigma_z - \sigma_x)^2]} \quad (1)$$

$$\frac{1}{\sqrt{2}} \sqrt{(\sigma_x - \sigma_y)^2 + (\sigma_y - \sigma_z)^2 + (\sigma_z - \sigma_x)^2 + 6(\tau_{xy}^2 + \tau_{yz}^2 + \tau_{zx}^2)} < \sigma_y^2 \quad (2)$$

Stress theory is more moderate than von Mises criterion for placing within the von Mises ellipse. As much as limiting the fundamental stresses to prevent ductile fracture, von Mises gives a fatigue value within acceptable limits, especially in cases of repeated stress and strain loads.

Another issue is to compare modern numerical methods within themselves. In this study, the belt conveyor is examined separately by the finite element method-FEM. FEM can calculate the stress concentrations and deformations that may occur due to the geometry of the problem precisely and in less time, since it discriminates and examines only the boundaries of the area of interest. Then, a sample belt conveyor to be analyzed was dimensioned. After the sizing phase, stress analysis was done analytically and then modern numerical methods were used.

The stress criteria considered in this study consist of static and fatigue strength analysis for the conveyor. The stress criteria that occur in the conveyor consist of simulations for setting the limits in both the maximum stresses and the stress range that can occur in drum and shaft and boundary conditions are taken into account. Displacement, deformation and von Mises analysis for three dimensional stress zones uncover radial, tangential and axial stresses analyzed in the pulley. When evaluating ductile material, usually the yield strength of the material is used as fracture. Distortion energy theory is used for static strength evaluation for this research. This theory predicts that yield begins for ductile materials as expected.

Belt Conveyor Static Analysis by FEM

The FEM is one of the important methods of continuum mechanics and widely used in engineering applications. Theoretical studies of this computational approach according to experimental results and literature review in the field of conveyor, which has many applications in industry, have been examined. Stress analysis of a belt conveyor is implemented using FEM.

FEA based on the application domain and methods are systematically established on the decomposition of sub-domains where the approximate solution is created (Wu, 2013). In fact, FEA divides the field into elements and reduces the number of unknown domains to parts that have the problem with the expression in the functions that precede it. This type of interpolation defines the boundaries of field variables at certain points as nodes. The FEM, which is a mathematical method, is used in ANSYS to obtain results for presentation and stress analysis and fluid flow to a wide range of engineering problems.

ANSYS is a design engineering general-purpose Finite Element Analysis (FEA) software package. ANSYS computer program used for analysis in engineering is a multi-purpose finite element program. Static and dynamic network analysis, which are seen in ANSYS's analysis capabilities as application areas, attract a lot of attention with its ability to solve mode frequency and buckling eigenvalue problems, static or time-varying analyzes. FEA is a numerical method used to break down a multifaceted system into very small parts called elements. The Workbench focuses on attaching existing geometry, setting up the finite element model, solving, and reviewing results. After geometric modeling of the conveyor belt system with given specifications it is subjected to analysis. The Analysis involves the following discretization called meshing, boundary conditions and loading.

A mesh dependency study for model was prepared in order to determine the optimum mesh size and material properties as shown in (Figure 3). The study shows that using 0.5 mm mesh size at the contact area satisfies the design criteria, where the results converge at that size as shown in (Figure 3). The mesh was built in a way that can reduce computation time while getting accurate results by refining the mesh at the contact zone and having a moderate size out of that specific zone as. Statics tetrahedrons type of mesh models developed with nodes 215156 and number of elements 58948. Belt conveyor essential components' material properties are presented in (Figure 3).

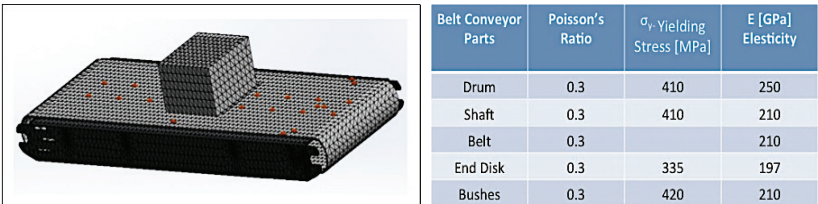


Figure 3. Meshed belt conveyor system and material properties

Force 2098 N was applied on the top of the belt surface with a box shape. The load applied to belt is uniformly distributed load in conveyor. The maximum deformation induced in belt conveyor system is 0.26 mm at near the tail pulley side belt surface. The maximum equivalent stress induced is 13.817 MPa and minimum equivalent stress induced is 1.733×10^{-7} MPa. The maximum shear stress induced is 6.875 MPa and minimum shear stress induced is 2.151×10^{-7} MPa. FE results show that the belt was indented due to its contact with both idler rolls as reported in the literature (Yuan X., 2019), where belt conveyor due to center roll has higher values than that for wing roll. It is also noted that idler rolls rotate due to the applied belt motion, which simulate the actual operation case. The exemplary

outcomes of the FEA results for static analysis are presented in (Figure 4). FEA results show that displacement analysis.

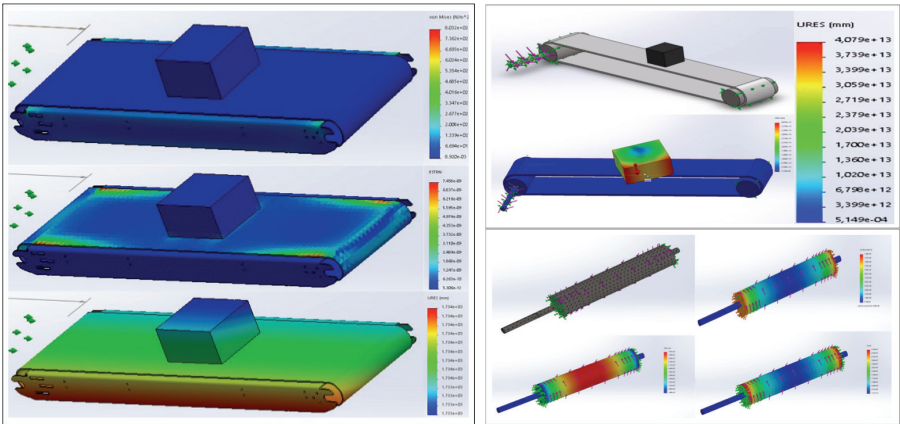


Figure 4. Static analyses of belt conveyor system

The number of nodes created was 206832 and elements were 60778. (Figure 5) shows the von mises analysis for the drum highlighted in red green blue. (Figure 5) shows the axial force relation to the weight of the conveyor and the belt. It was performed for finite element-FE analysis and shear stresses with the failure criteria. FE analysis was applied in ANSYS and analysis results were obtained.

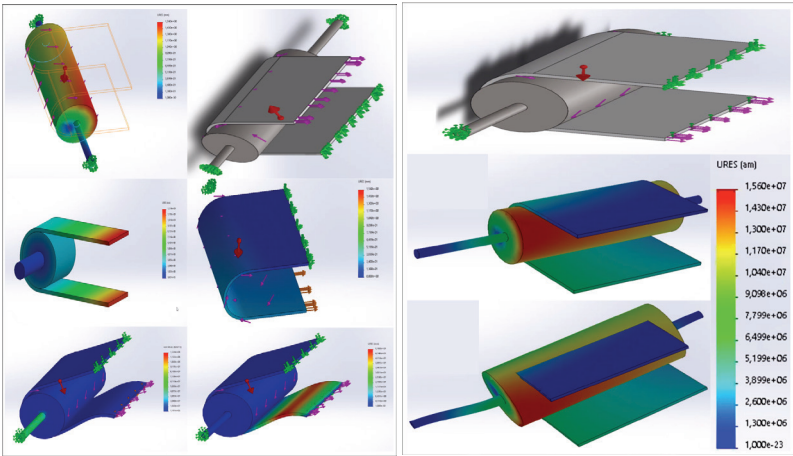


Figure 5. Conveyor drum static and displacement analysis

The conveyor repeat communication continued during the simulations and maintained the shear

stresses. The stress obtained in the analyzes was found to be 5.85 MPa and the shear stress at 2.73 MPa. These stresses are within the allowable limit of the rubber material and are found to be safe. The activity that maintains the conveyor movement and shear stresses during the simulations were given in (Figure 5).

Several types of problems resolved by FEM in engineering area covering elastic, elastoplastic and viscoelastic analysis of Lattice beams, frames, plates, shells and solids. The displacements, stresses, stresses, velocities, pressure and load analyses all depend on time in dynamic problems as shown in (Figure 6). The belt conveyor under research is distributed into finite number of mesh elements. The movements of the belt were obtained by modeling mass, rigidity. Initial conditions are determined and the forces affecting are computed. The conveyor belt is split into an assembling of elements. Beam properties are defined for every element. In this research, considering the behavior of longer beam elements representing the long conveyors and belts are determined compared to transverse dynamic study. In order to achieve the equations of motion, mass, hardness and damping matrices are arranged. The power vector is generated when a single exterior force is affected to the drive the belt conveyor.

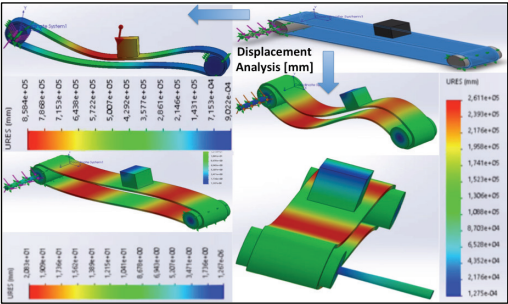


Figure 6. Conveyor displacement analysis

Analytical design is verified with the help of ANSYS software. Exactly similar forces and constraints simulated in ANSYS to get accurate results. Finite element analysis is carried out to find von Mises stresses, safety factor, total deflection on pulley and its components because of belt tensions as presented in (Figure 7) and (Figure 8).

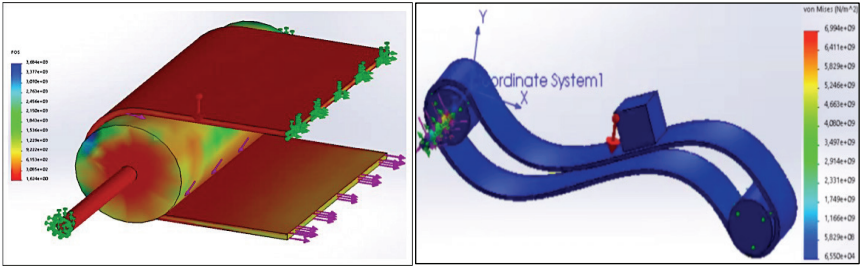


Figure 7. Safety factor and the von Mises analysis

For finite element analysis all standard material properties are assigned. Dead weight of the pulley is considered. Resultant tension is calculated and applied as a uniform radial pressure over the pulley surface in the region of angle of wrap, and throughout the belt width. Torques given for driven pulleys is applied at the drive end of the shaft. Initially 3D model SLIDWORKS of pulley assembly created using ANSYS software.

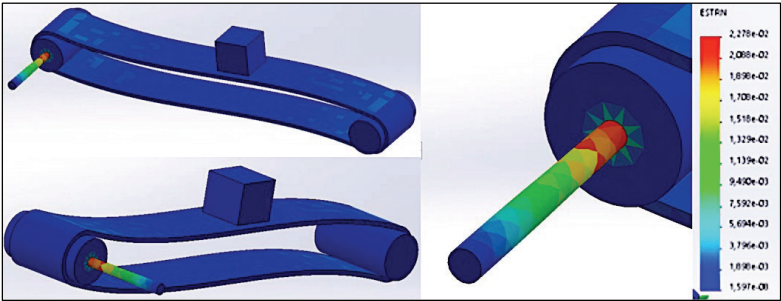


Figure 8. Strain analysis on drum shaft and belt system

Load and constraints applied to all two types of pulley. Maximum tight side tension is 232271N and maximum slack side tension is 64396N calculated by above analytical method. Horizontal and vertical forces are 345478N and 9090N respectively. Therefore resultant force calculated is 345598N. By considering equivalent weight of belt and rubber, contact length it gives total contact area affecting von Mises criteria and strain value under stress as shown in (Figure 9). Using this area find out pressure acting on pulley is 0.1MPa. Boundary conditions applied on pulley are torque 90952 Nm, pressure on belt 0.10Mpa, gravity force acting 9.806 m/s^2 .

Meshing of pulley is carried out with quad and tetra element type. Total slippage is considered between the shaft and the disc hub close to the drive side to simulate the worst possible loading condition. Limit stress in design was considered as the endurance stress for each material.

As the maximum stresses developed in worst possible conditions are clearly less than the allowable limits in all the cases, hence design is safe in all case of pulley mark. Forces applied to edge of the drum were computed as given in (Figure 10).

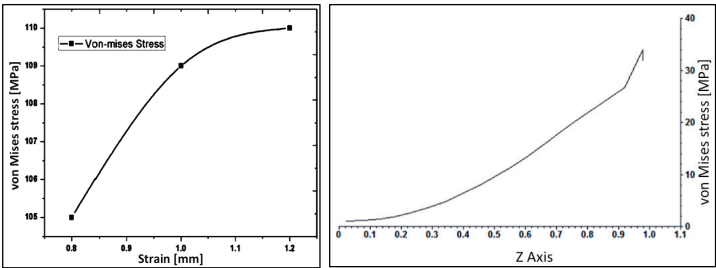


Figure 9. The von Mises stress and strain analysis

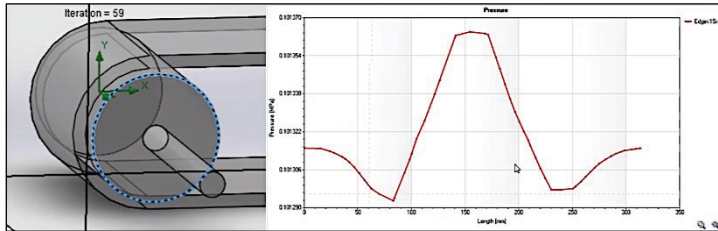


Figure 10. Forces applied to edge of the drum

Experimental Results

After completing design and analysis of conveyor system it's also important to allow adequate time for testing prior to getting the new system up and running. There could be hidden mechanical issues of belt conveyor that would delay production, or any number of other problems that may need to be adjusted so the conveyor system can perform at peak efficiency.

Basic initial testing step is visual safety inspection. Check all the guards in place, emergency pull-stops accessible at any point along the line. It's also important to ensure the mechanical and junction boxes are closed. Function testing is effective at identifying any major system flaws, but it's also important to completely load the system to realize how it achieves at full capacity. These load tests are also called simulated load tests. Conveyor load test carried out on basis of three load conditions. First is no load, second is actual load and full load condition. Testing speed is variable of conveyor on the basis of load variation. The linear speed of conveyor belt was measured by using contact tachometer with wheel attachment. The wheel against the conveyor calculated linear speed on the display based on the rotational rate and fixed diameter of the wheel. CFD analysis was made by ANSYS-CFX in v20. For CFD analysis of belt conveyor, a mesh model was build as presented in (Figure 11). Airflow velocity of belt conveyor was modeled in (Figure 12). CFD Pressure analysis on the z- axis along was shown in (Figure 13). Acoustic Analysis of conveyor was also modeled to find the working noise conditions. As shown in (Figure 13), The noise level dB was obtained as safe or more below than maximum limits.

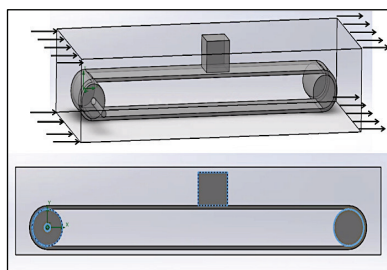


Figure 11. CFD analysis of belt conveyor

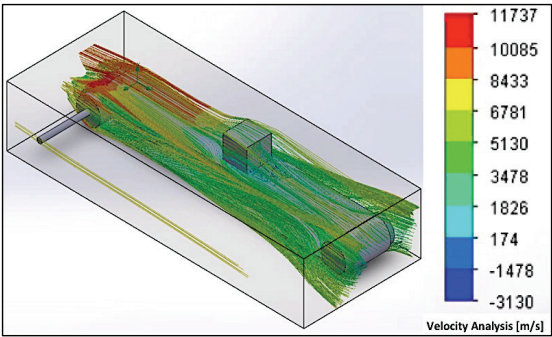


Figure 12. Airflow velocity of belt conveyor

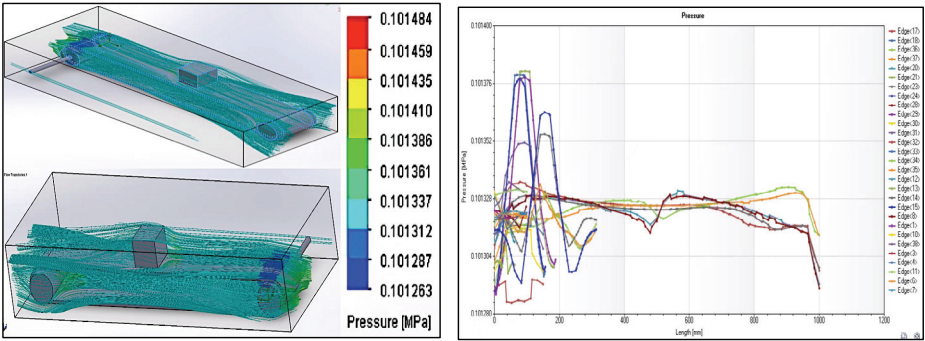


Figure 13. CFD Pressure analysis on the z- axis along

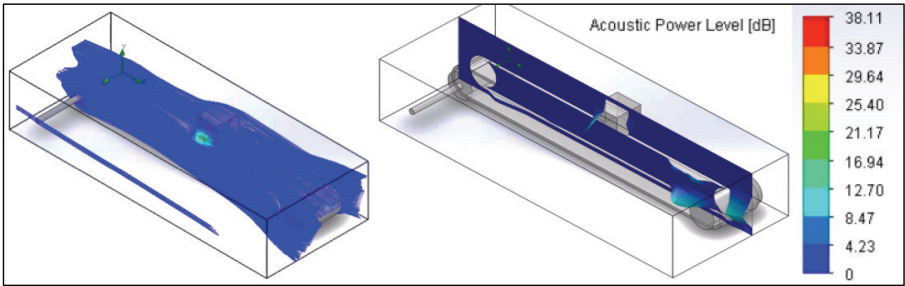


Figure 14. Acoustic Analysis of conveyor

Conclusions

A belt conveyor system with two rollers can be developed for handling the weight. The belt conveyor system was designed with high degree of automation, loading, movement and unloading efficiency. These are very flexible, safe, with low initial, and maintenance cost. From the results of the FE analysis, stresses for both the mechanical and CFD were understood within the allowable limit of the rubber material in conveyor. With an optimized belt, it can be reflected in the power requirement. 3D model of the belt conveyor system is generated in SOLIDWORKS parametric model and this model is imported to ANSYS for processing work. An amount of force 10.791 KN is applied along the upper belt surface and base structure is fixed. Above finite element analysis results gave Maximum stresses developed at extreme high load conditions on conveyor pulleys are less than the allowable limits, hence design of conveyor system is safe.

Design of belt conveyor for given design capacity is found safe as stress and deflection calculations from finite element analysis on critical parts of conveyor pulley are less than allowable limits. Approximately constant conveyor speed achieved at various materials loading conditions therefore conveyor are safe and efficient to use for heavy-duty applications with time circumstances. The maximum deformation induced in belt conveyor system was 0.6403mm near the tail pulley side belt surface. From the FEA output the maximum design strength found as 12.817 MPa from the material property. The ultimate tensile strength of the material obtained 300 MPa, then the factor of safety becomes within that safety limit. The value of equivalent von-Misses stress that comes out from the analysis was far less than material yield stress so the design constructed was safe. Maximum power required at full load condition whereas in case of actual load condition power was comparatively lower. This ensures design and motor safety under extreme heavy load conditions.

References

- Bajda, M.; Blazej, R.; Jurdziak, L. Analysis of changes in the length of belt sections and the number of splices in the belt loops on conveyors in an underground mine. *Eng. Fail. Anal.* 2019, 101, 436–446.
- Carretero, L.; Valero, J. Existence of periodic solutions for a scalar differential equation modeling optical conveyor belts. *J. Math. Anal. Appl.* 2019, 480, 123385.
- DIN 22101, 2016. Belt Conveyors for Bulk Materials - Bases for calculation and design. DIN.
- Daniyan, I. A., Adeodu, A. O. and Dada, O. M. (2014). Design of a Material Handling Equipment: Belt Conveyor System for Crushed Limestone Using 3 Roll Idler. *Journal of Advancement in Engineering and Technology*. pp. 1-7.
- Fenner Dunlop “Conveyor Handbook” (2009). Conveyor Belting Australia. pp 1-70.
- Gerdemeli, S. Kurt, E. T. Dayan “Belt Conveyor Design and Analysis”, scientific proceedings xi international congress "machines, technologies, materials" 2014 ISSN 1310- 3946.
- ISO 15236-1: International Organization for Standardization. Steel cord conveyor belts Part 1: Design, dimensions and mechanical requirements for conveyor belts for general use, 2015
- Lu, Y.; Li, Q. A regression model for prediction of idler rotational resistance on belt conveyor. *Meas. Control* 2019, 52, 441–448.
- Mathaba T, Xia X. Optimal and energy efficient operation of conveyor belt systems with downhill conveyors. *Energy Efficiency* 2017; 10(2): 405-417
- Munzenberger, P.J.; OShea, J.I.; Wheeler, C.A. A comparison of rubber stress relaxation models for conveyor belt indentation rolling resistance calculations. *Int. J. Mech. Mater. Des.* 2019, 15, 213–224.
- Nuttall AJG, Lodewijks G. Dynamics of multiple drive belt conveyor systems. *Part Part Syst Charact*

- 2017;24:365–9.
- Rao, A. M. , Suresh, G., S., V., Priyadarshini, D., (2012), Alternate Design and Optimization of Conveyor Pulley Using Finite Element Analysis. *International Journal of Engineering Research and Technology* Vol 1 Issue 7.
- Rick Garrity, “The Basics Of Conveyor Engineering Belt, Roller And Gravity” Manager, system engineering Interlake conveyors, INC 300HWY 44 East Shepherdsville, Kentucky 40165, 2019.
- Shen, J.; Wheeler, C.; O’Shea, J.; Ilic, D. Investigation of the dynamic deflection of conveyor belts via experimental and modelling methods. *Measurement* 2018, 127, 210–220.
- Suhas M. Shinde and R.B. Patil, “Design and Analysis of a Roller Conveyor System for Weight Optimization and Material Saving”, *International Journal on Emerging Technologies*, 2012, 3(1): 168-173.
- Yuan X., Yang S., Niu Q., Analysis and Design of the Roller for Belt Conveyor Based on ANSYS, *Advanced Materials Research*, 1027, 315-319, 2014.
- Wang, F.S. Research on flexible multibody dynamics modeling of conveyor belt. *Mech. Transm.* 2018, 042, 43–46.
- Wu Z., Guan W. J., Three-dimensional parametric modelling and finite element analysis of drum on belt conveyer, *Applied Mechanics and Materials*, 319, 474-476, 2013.